6th BSME International Conference on Thermal Engineering (ICTE 2014)

Free convection fluid flow in the presence of a magnetic field with thermally stratified high porosity medium

Abdullah Ahmed Foisal and Mahmud Alam*

Mathematics Discipline ,Khulna University, Khulna-9208, Bangladesh

Abstract

MHD free convection over an inclined plate in a thermally stratified high porous medium in the presence of a magnetic field has been studied. The dimensionless momentum and temperature equations have been solved numerically by explicit finite difference technique with the help of a computer programming language Compaq Visual Fortran 6.6a. The obtained results of these studies have been discussed for the different values of well known parameters with different time steps. Also, the stability conditions and convergence criteria of the explicit finite difference scheme has been analyzed for finding the restriction of the values of various parameters to get more accuracy. The effects of various governing parameters on the fluid velocity, temperature, local and average shear stress and Nusselt number has been investigated and presented graphically.

Keywords: MHD flow; free convection; thermal stratification; porous medium

1. Introduction

Free convection fluid flow with thermally stratified high porosity medium occurs in environment has an important applications to the engineers dealing with many industrial process and technological fields such as in geophysics, astrophysics, geothermal energy convection, petroleum reservoirs, magnetohydrodynamics (MHD) accelerators and generators. Gebhart et al. [1] have investigated an overview of the natural convection flows. The

---

* Corresponding author. Tel.: +88-041-725741; cell: +8801912982811 fax: +88-041-731244.
  *E-mail address:*alam_mahmud2000@yahoo.com

natural convection flow over a vertical heated surface in a porous medium has been studied by Bejan and Khair [2]. The non-Darcy effects on the natural convection boundary layer flow on an isothermal vertical flat plate embedded in a high-porosity medium was considered by Chen et al. [3]. The effect of the ambient thermal stratification on the problem studied by Chen et al. [3]. Chamkha [4] has extended the analysis of Chenet al. [3] to include the effects of the magnetic field. The non-linear coupled parabolic partial differential equations governing the flow have been solved numerically by using an implicit finite-difference scheme similar to that of Blottner [5].

Hence, the purpose of the present study is to extend the work of Takhar et al. [6] investigates effects of non-uniform wall temperature or mass transfer in finite sections of an inclined plate on the MHD natural convection flow in a temperature stratified high-porosity medium. The proposed model has been transformed into non-similar coupled partial differential equations by usual transformation. Finally, the governing momentum and energy equations are solved numerically by using the explicit finite difference method.

Nomenclature

A	Dimensionless constant	u, v	velocity components
B	Magnetic field	U	hypothetical velocity
D_c	Darcy Number		
E_c	Eckert uumber	*Greek letters*	
G_r	Grashof number	v	kinematic viscosity
k	Thermal conductivity	ρ	density
L	Characteristic length	Ω	angle of inclination
M	Magnetic parameter	Γ	dimensionless inertia coefficient
N_u	Nusselt number		
P	Pressure	*Subscripts*	
P_r	Prandlt number	i	initial conditions
S_T	Thermal stratification	W	condition at the wall
T	Temperature	∞	conditions at infinity

2. Mathematical analysis

Consider an unsteady MHD free convection flow past infinite vertical porous plate which is thermally stratified. Let us consider an unsteady free convective flow of an electrically conducting viscous fluid through a porous medium along a semi-infinite vertical porous plate $y = 0$ in a rotating system under the influence of transversely applied magnetic field. The flow is assumed to be in the x-direction which is taken along the plate in the upward direction and y-axis is normal to it. Initially the fluid is at rest, after the whole system is allowed to rotate with a constant angular velocity Ω about the y-axis. Since the system rotates about the y-axis, so it can be taken $\Omega = (0, -\Omega, 0)$. The temperature of the plate raised from T_w to T_∞, where T_∞ be the temperature of the uniform flow. A uniform magnetic field B is taken to be acting along the y-axis which is assumed to be electrically non-conducting. The assumption is justified when the
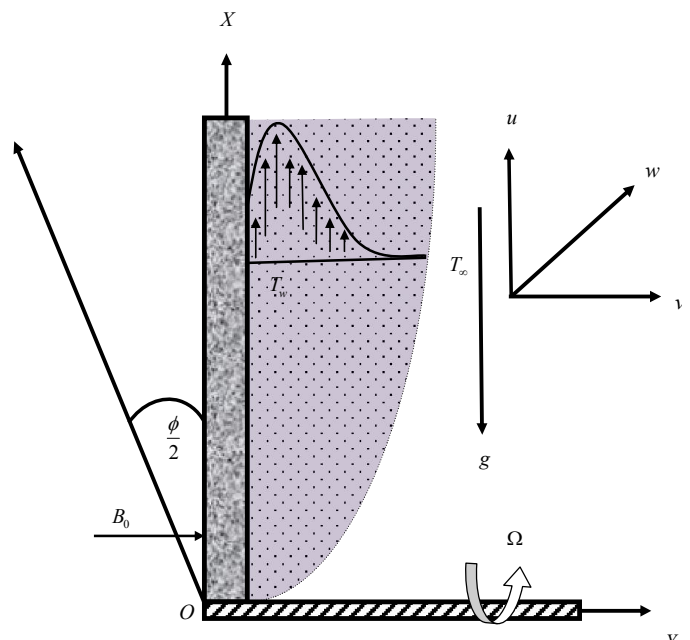

Fig1. Physical configuration and coordinate system

magnetic Reynolds number of the flow is taken to be small enough so that the induced magnetic field is negligible and is of the form $B = (0, B_0, 0)$ and the magnetic lines of force are fixed relative to the fluid. The physical configuration of this study is furnished in the Fig.1.

Thus accordance with the above assumptions relevant to the problem and under the electromagnetic Boussinesq approximation, in a rotating frame the basic boundary layer equations are;
The continuity equation:

$$\frac{\partial u}{\partial x} + \frac{\partial v}{\partial y} = 0 \tag{1}$$

Momentum equations:

$$\frac{1}{\varepsilon^2}(\frac{\partial u}{\partial t} + u\frac{\partial u}{\partial x} + v\frac{\partial u}{\partial y}) = g\beta(T - T_\infty)Cos\left(\frac{\phi}{2}\right) + \frac{v}{\varepsilon}\frac{\partial^2 u}{\partial y^2} - \frac{v}{k}u + 2\Omega w - c(u^2 + w^2) - \frac{\sigma B_0^2 u}{\rho} \tag{2}$$

$$\frac{1}{\varepsilon^2}(\frac{\partial w}{\partial t} + u\frac{\partial w}{\partial x} + v\frac{\partial w}{\partial y}) = \frac{v}{\varepsilon}\frac{\partial^2 w}{\partial y^2} - \frac{v}{k}w - 2\Omega u - c(u^2 + w^2) - \frac{\sigma B_0^2 w}{\rho} \tag{3}$$

Energy equation

$$\frac{\partial T}{\partial t} + u\frac{\partial T}{\partial x} + v\frac{\partial T}{\partial y} = \frac{k}{\rho c_p}\frac{\partial^2 T}{\partial y^2} + \frac{v}{c_p}[\left(\frac{\partial u}{\partial y}\right)^2 + \left(\frac{\partial w}{\partial y}\right)^2] + \frac{\sigma B_0^2}{\rho c_p}(u^2 + w^2) \tag{4}$$

To obtain the dimensionless governing equations and the boundary condition the following non-dimensional quantities are introduced as;

$$U = \frac{G_r^{-1/2}uL}{v}, V = \frac{G_r^{-1/2}vL}{v}, w = \frac{G_r^{-1/2}wL}{v}, X = \frac{x}{L}, Y = \frac{G_r^{1/4}y}{L}, \tau = \frac{\tau v G_r^{1/2} y}{L^2}, \theta = \frac{T - T_\infty}{T_w - T_\infty}$$

Then the non-dimensional equations are as follows;

$$\frac{\partial U}{\partial X} + \frac{\partial V}{\partial Y} = 0 \tag{5}$$

$$\frac{\partial U}{\partial \tau} + U\frac{\partial U}{\partial X} + V\frac{\partial U}{\partial Y} = \varepsilon\frac{\partial^2 U}{\partial Y^2} + \varepsilon^2\theta Cos\left(\frac{\phi}{2}\right) + \varepsilon^2 RW - \epsilon^2\Gamma\left(U^2 + W^2\right) - \varepsilon^2\left(D_c^{-1} + M^2\right)U \tag{6}$$

$$\frac{\partial W}{\partial \tau} + U\frac{\partial W}{\partial X} + V\frac{\partial W}{\partial Y} = \varepsilon\frac{\partial^2 W}{\partial Y^2} - \varepsilon^2 RU - \varepsilon^2\Gamma\left(U^2 + W^2\right) - \varepsilon^2\left(D_c^{-1} + M^2\right)W \tag{7}$$

$$\frac{\partial \theta}{\partial \tau} + U\frac{\partial \theta}{\partial X} + V\frac{\partial \theta}{\partial Y} = \frac{1}{P_r}\frac{\partial^2 \theta}{\partial Y^2} + Ec\left[\left(\frac{\partial U}{\partial Y}\right)^2 + \left(\frac{\partial W}{\partial Y}\right)^2\right] + M^2 E_c\left(U^2 + W^2\right) - S_T U \tag{8}$$

within the boundary conditions;

$$U = 0, V = 0, W = 0, \ \theta = 1 - S_T X \qquad \text{at } y = 0 \tag{9}$$
$$U \to 0, V \to 0, W \to 0, \ \theta \to 0 \qquad \text{as } y \to \infty \tag{10}$$

Here, the boundary conditions for temperature along the wall in non-dimensionless form are obtained as follows;
$$\therefore \theta = 1 - S_T X$$

3. Shear Stress and Nusselt Number

From the velocity field, the effect of various parameters on the local and average shear stress has been investigated. The following quantities represent the local and average shear stress at the plate.

Local shear stress, $\tau_L = \mu(\frac{\partial u}{\partial y})_{Y=0}$ and average shear stress,

$\tau_A = \mu\int(\frac{\partial u}{\partial y})_{Y=0}dx$ which are proportional to $(\frac{\partial U}{\partial Y})_{Y=0}$ and

$\int_0^{100}(\frac{\partial U}{\partial Y})_{Y=0}\ dX$ respectively.

From the temperature field, the effects of various parameters on the local and average heat transfer coefficients have been investigated. The following equations represent the local and average heat transfer rate that is well known as Local Nusselt

number, $N_{uL} = \mu\left(-\frac{\partial T}{\partial y}\right)_{Y=0}$ and average Nusselt number stress,

Fig 2. Finite difference grid system

$N_{uA} = \mu\int(-\frac{\partial T}{\partial y})_{Y=0}dx$, which are proportional to $(-\frac{\partial\overline{T}}{\partial Y})_{Y=0}$ and $\int_0^{100}(-\frac{\partial\overline{T}}{\partial Y})_{Y=0}dX$ respectively.

4. Numerical Technique

To obtain the difference equations, the region of the flow is divided into a grid of lines parallel to X and Y axes where X-axes is taken along the plates and Y- axes is normal to the plates. It is considered that the plate of the height $X_{max} = 100$ i.e X varies from 0 to 100 and regard $Y_{max} = 25$ as corresponding to $Y \to \infty$ i.e, Y varies from 0 to 25. There are $m = 200$ and $n = 200$ grid spacing in the X and Y directions respectively has been shown in the Fig.2.

It has been assumed that $\Delta X, \Delta Y$ are constant mesh sizes along X and Y directions respectively taken as follows $\Delta X = 0.5(0 \le x \le 100)$, $\Delta Y = 0.125(0 \le y \le 25)$ with the smaller time step, $\Delta\tau = 0.001$.

Now U', W' and θ' denote the values of U, W and θ at the end of a time-step respectively. The explicit finite difference approximation gives;

$$\frac{U_{i,j} - U_{i-1,j}}{\Delta X} + \frac{V_{i,j} - U_{i,j-1}}{\Delta Y} = 0 \tag{11}$$

$$\frac{U'_{i,j} - U_{i,j}}{\Delta\tau} + U_{i,j}\frac{U_{i,j} - U_{i-1,j}}{\Delta X} + V_{i,j}\frac{U_{i,j+1} - U_{i,j}}{\Delta Y} = \varepsilon\frac{U_{i,j+1} - 2U_{i,j} + U_{i,j-1}}{(\Delta Y)^2} + \varepsilon^2\theta_{i,j}Cos\left(\frac{\phi}{2}\right) + \varepsilon^2 RW_{i,j}$$
$$-\varepsilon^2\Gamma\left(U_{i,j}^2 + W_{i,j}^2\right) - \varepsilon^2\left(D_c^{-1} + M^2\right)U_{i,j} \tag{12}$$

$$\frac{W'_{i,j} - W_{i,j}}{\Delta\tau} + U_{i,j}\frac{W_{i,j} - W_{i-1,j}}{\Delta X} + V_{i,j}\frac{W_{i,j+1} - W_{i,j}}{\Delta Y} = \varepsilon\frac{W_{i,j+1} - 2W_{i,j} + W_{i,j-1}}{(\Delta Y)^2} - \varepsilon^2 RU_{i,j} - \varepsilon^2\Gamma\left(U_{i,j}^2 + W_{i,j}^2\right)$$
$$-\varepsilon^2\left(D_c^{-1} + M^2\right)W_{i,j} \tag{13}$$

$$\frac{\theta'_{i,j} - \theta_{i,j}}{\Delta\tau} + U_{i,j}\frac{\theta_{i,j} - \theta_{i-1,j}}{\Delta X} + V_{i,j}\frac{\theta_{i,j+1} - \theta_{i,j}}{\Delta Y} = \frac{1}{P_r}\frac{\theta_{i,j+1} - 2\theta_{i,j} + \theta_{i,j-1}}{(\Delta Y)^2} + E_c[(\frac{U_{i,j+1} - U_{i,j}}{\Delta Y})^2 + (\frac{W_{i,j+1} - W_{i,j}}{\Delta Y})^2]$$
$$-S_T U_{i,j} - M^2 Ec\left(U_{i,j}^2 + W_{i,j}^2\right) \tag{14}$$

With the finite difference boundary conditions;

$U_{i,0}^n = 0, \quad V_{i,0}^n = 0, \quad W_{i,0}^n = 0, \quad \theta_{i,0}^n = 1 - S_T X$

$U_{i,L}^n = 0, \quad V_{i,L}^n = 0, \quad W_{i,L}^n = 0, \quad \theta_{i,L}^n = 0 \qquad$ where, $L \to \infty$

Here the subscript i and j designates the grid points with x and y coordinate and n represents a value of time $\tau = n\Delta\tau$ where $n = 1, 2, 3, \ldots$. At the end of the time step $\Delta\tau$, the new primary velocity $U_{i,j}^{n+1}$, the new secondary velocity and the new temperature distributions at all interior nodal points, may be calculated by successive applications of equations (11)-(14) respectively. Also the numerical values of the local shear stress and Nusselt number are evaluated by five-point approximation formula for their derivatives and the average shear stress and Nusselt number are calculated by the use of Simpson's $\frac{1}{3}$ integration formula.

5. Results and discussion

The results have been presented for various values of thermal stratification parameter (S_T), Darcy number D_c magnetic parameter M and porosity parameter ε. Figures 3(a)-3(b) and 4(a)-4(b) represented the local and average primary and secondary shear stress for the different values of thermal stratification parameter (S_T). From these figures it has been shown that the local primary and average shear stress decreases with the increasing values of the thermal stratification parameter while the local secondary and average shear stress increases with the increasing values of thermal stratification parameter. Figures 5(a)-5(b) and 6(a)-6(b) represented the local and average primary and secondary shear stress for the different values of Darcy number D_c. From these figures it has been shown that the local primary and average shear stress increases with the increasing values of the Darcy number while the local secondary and average shear stress decreases with the increasing values of Darcy number D_c. Figures 7(a)-7(b) and 8(a)-8(b) represented the local and average primary and secondary shear stress for the different values of Magnetic parameter M. From these figures it has been shown that local and average primary shear stress decreases while the local and average secondary shear stress increases with the increase of magnetic parameter. Figure 9(a)-9(b) represented the local primary and secondary shear stress for the different values of porosity parameter (ε). Figure 10(a)-10(b) represented the local Nusselt number for different values of thermal stratification (S_T) and Darcy number D_c. from these figures it has been shown that the local Nusselt number increases with the increase of thermal stratification and Darcy number.
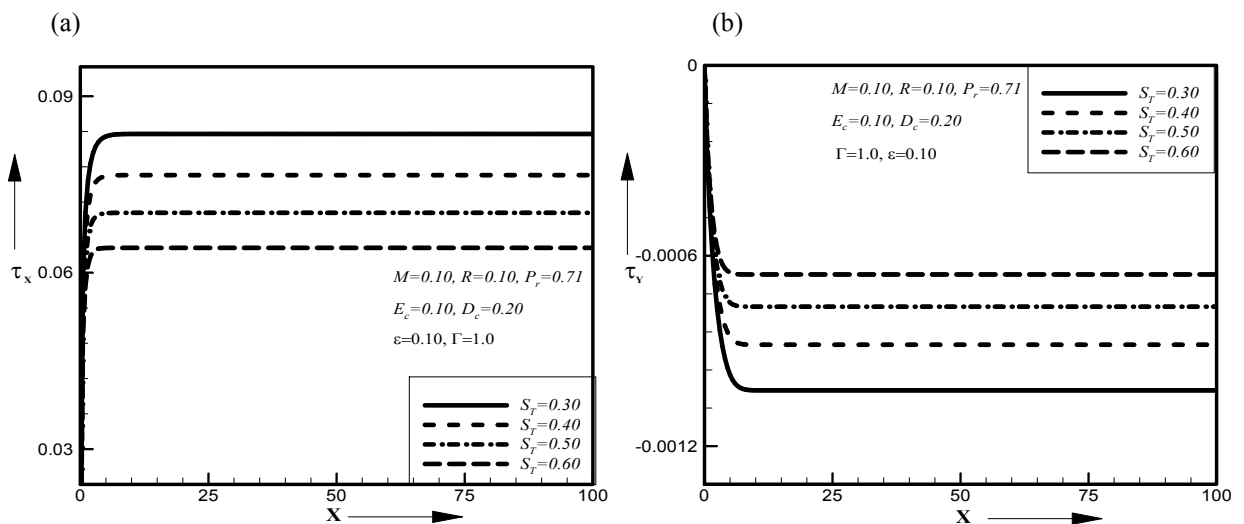

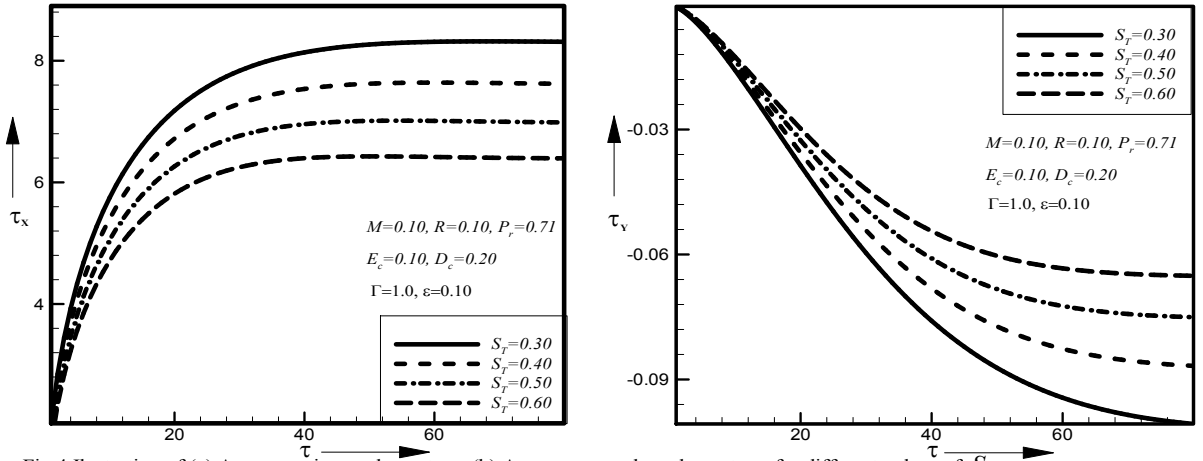Fig 3.Ilustration of (a) Local primary shear stress (b) Local secondary shear stress for different values of S_T

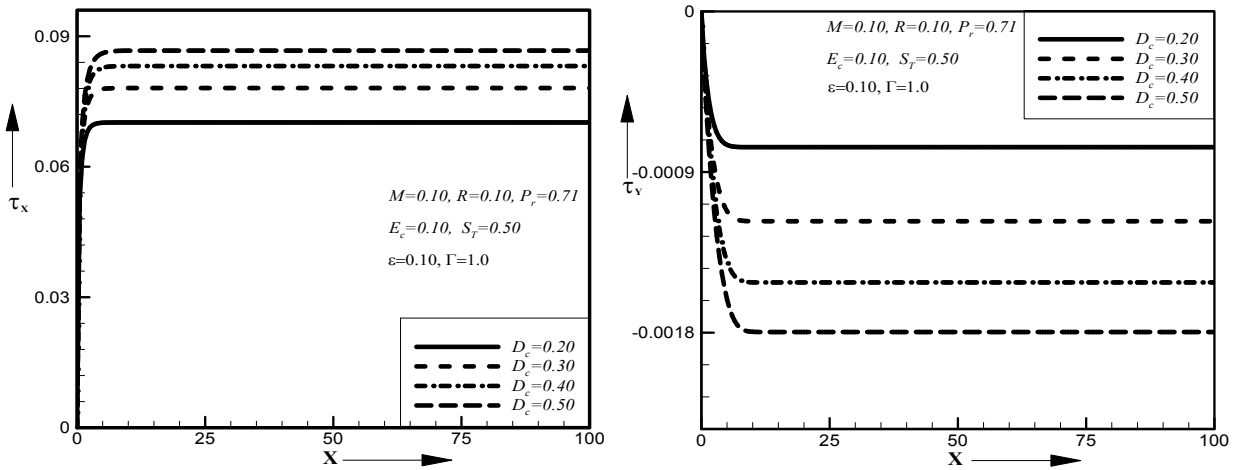Fig 4.Ilustration of (a) Average primary shear stress (b) Average secondary shear stress for different values of S_T

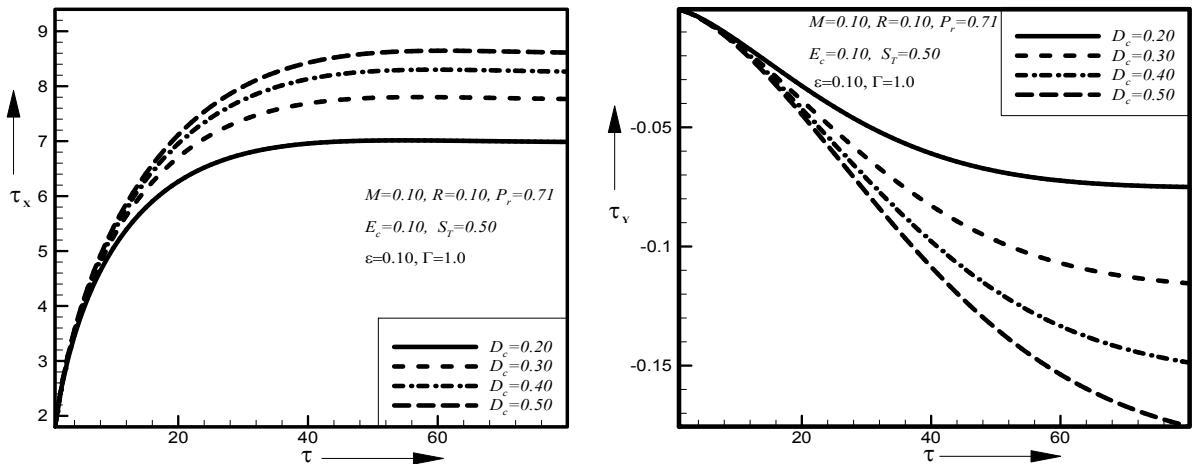Fig 5.Ilustration of (a) Local primary shear stress (b) Local secondary shear stress for different values of D_c

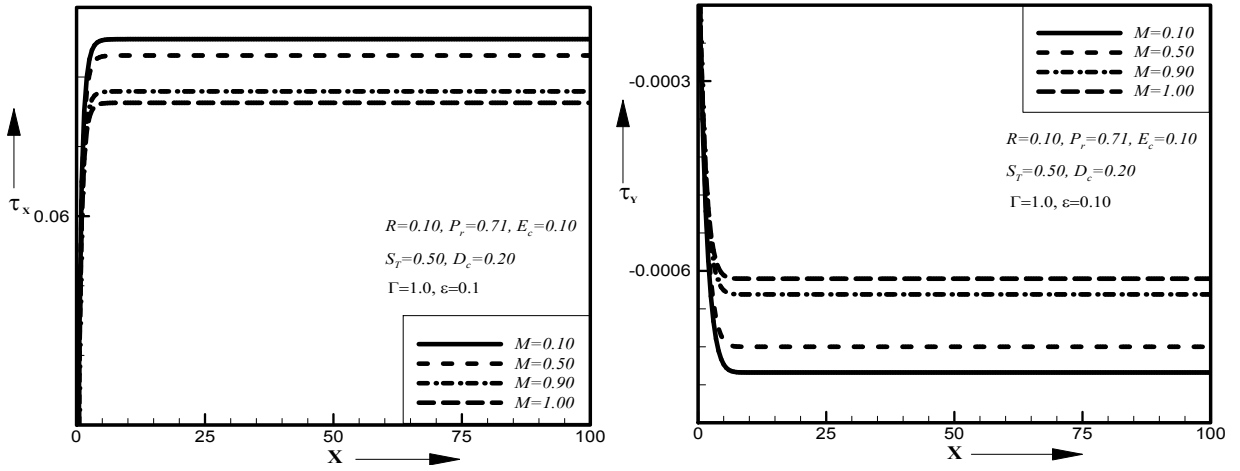Fig 6.Ilustration of (a) Average primary shear stress (b) Average secondary shear stress for different values of D_c

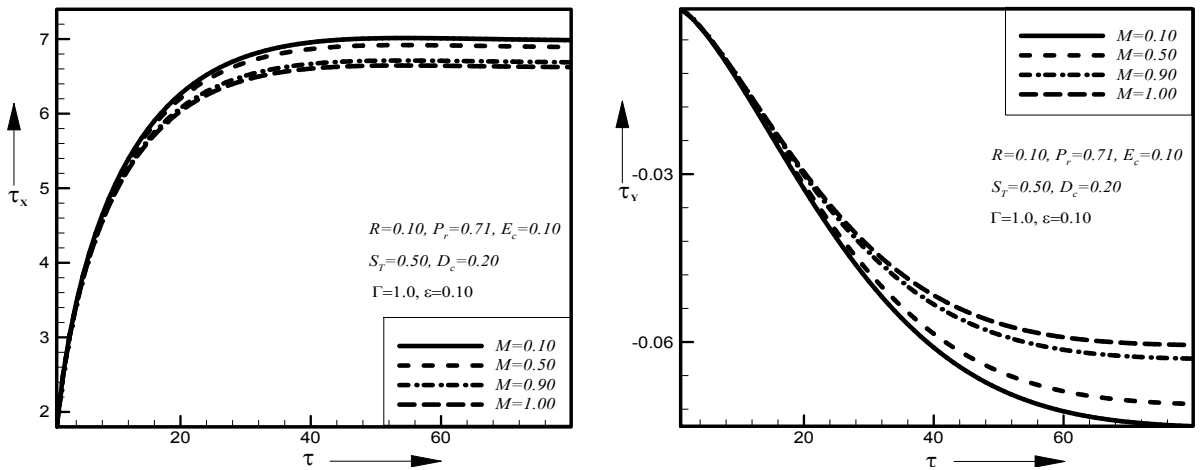Fig 7.Ilustration of (a) Local primary shear stress (b) Local secondary shear stress for different values of M

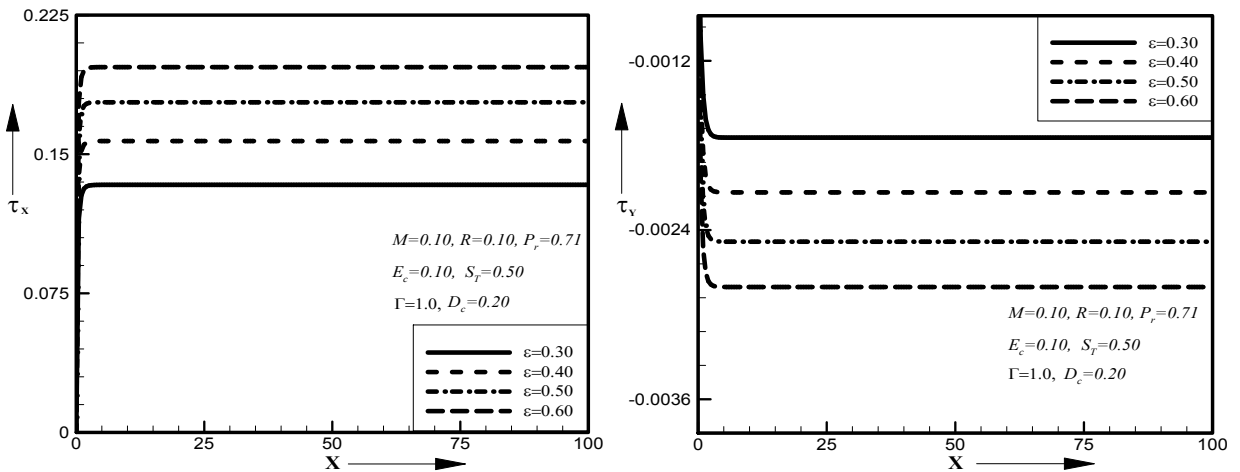Fig 8.Ilustration of (a) Average primary shear stress (b) Average secondary shear stress for different values of M

Fig 9.Ilustration of (a) Local primary shear stress (b) Local secondary shear stress for different values of ε
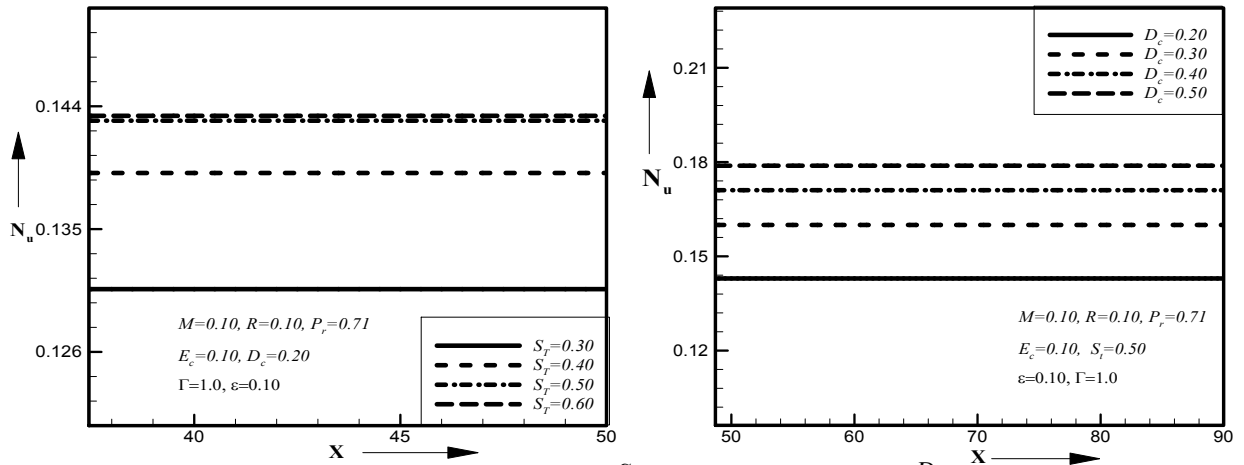
Fig 10.Ilustration of (a) local Nusselt number for different values of S_T (b) and for different values of D_c

6. Conclusions

In the present study, the local primary and average shear stress decreases with the increases of thermal stratification parameter while the local secondary and average shear stress increases with the increase of thermal stratification parameter. The local primary and average shear stress increases while the local secondary and average shear stress has decreases with the increases of Darcy number. The local primary shear stress increases for the porosity parameter while reverse effect shows for local secondary shear stress with the increases of porosity parameter. Local Nusselt number increases with the increase of thermal stratification parameter and for Darcy number.

References

[1] B. Gebhart, Y. Jaluria, R.L. Mahajan, B. Sammakia, Buoyancy-Induced Transport, Hemisphere, Washington, DC, (1988).

[2] A. Bejan, K.R. Khair, Heat and mass transfer by natural convection in a porous medium, Internat. J. Heat Mass Transfer 29 (1985) 909–918.

[3] C.K. Chen, C.I. Hung, H.C. Horng, Transient natural convection on a vertical flat plate embedded in a high porosity medium, ASME J. Energy Res. Tech. 109 (1987) 112–118.

[4] A.J. Chamkha, Hydromagnetic natural convection from an isothermal inclined surface adjacent to a thermally stratified porous medium, Int. J. Engng. Sci. 35 (1997) 975–986.

[5] F.G. Blottner, Finite-difference method of solution of a buoyancy layer equations, AIAA J. 8 (1970) 193–205.

[6] Takhar, H. S., Chamka, A .J. and Nath, G., Effects of non-uniform wall temperature or mass transfer in finite sections of an inclined plate on the MHD natural convection flow in a temperature stratified high-porosity medium, Int. J. Thermal Sciences 42, (2003) 829–836.

6th BSME International Conference on Thermal Engineering (ICTE 2014)

CFD Analysis of a Real Plant Fluidized Bed Combustor based on Co-firing

Hemant Kumar*, S.K. Mohapatra[a], Ravi Inder Singh[b]

Department of Mechanical Engineering, Punjabi University, Patiala -147002, India
[a]Department of Mechanical Engineering, Thapar University, Patiala-147004, India
[b]Department of Mechanical Engineering, Birla Institute of Technology and Science, Pilani-333031, India

Abstract

In this paper computational analysis of a real plant Bubbling Fluidized Bed (BFB) incinerator has been done, using FLUENT 6.3, CFD code. Keeping in mind the biomass potential in agricultural state like Punjab, India, various corporate sectors initiated the use of these renewable energy sources such as rice husk, paddy rejects and sugarcane baggase etc. in sharing with conventional fuels such as coal. The study has been done at Captive Power Plant (CPP) of Ambuja Cement Limited, Ropar, Punjab, India. The boiler, with 45TPH capacity, based on Fluidized Bed Combustion (FBC) system which is a prevalent biomass conversion technology uses coal and biomass (70% coal and 30% biomass) as fuels.

During field study the required data for combustion analysis has been collected with thorough understanding of the FBC system based on co-firing. In this combustor f-grade coal is being used with a 30% share of biomass in mixed form which is supplied from four overfeed ports. Standard k–ϵ two-phase turbulence model has been used to describe the gas–solids flow in the BFB. The analysis of combustion is done by Non-Pre Mixed (NPM) approach in species model. In this paper temperature contours inside the furnace and mass fractions of O_2 and CO_2 have been obtained by CFD tool. The temperatures along the biomass ports show a higher range due to instantaneous burning of biomass in suspension in the form of flame. Temperature in the vicinity of bed was found up to 1200K and at the exit of the furnace was found around 1140K. The O_2 concentration was found higher over the bed due to the presence of primary air used for fluidization, however the CO_2 concentration was found more near biomass flame due to instantaneous combustion.

Keywords: CFD; biomass; Fluidized bed; combustion; co-firing

*Corresponding author. Tel.: +91- 959-246-6014; fax: +91-175-239-3005.
*E-mail address:*hkumar@pbi.ac.in

Nomenclature

P_g, P_s	gas, solid phase pressure, N/m^2	k	Thermal conductivity, W/mK
v_g, v_s	gas, solid phase velocity vector, m/s	σ	solid-phase shear stress, N/m^2
$\varepsilon_g, \varepsilon_{s,}$	gas, solid phase volume fraction	*abbreviations*	
ρ_g, ρ_s	gas, solid phase density, kg/m^3	BFB	Bubbling Fluidized Bed
μ_g, μ_s	gas, solid phase shear viscosity, Pa s	CPP	Captive Power Plant
τ_g, τ_s	gas, solid phase shear stress, N/m^2	FBC	Fluidised Bed Combustion
h_g, h_s	gas, solid phase enthalpy, j/kg	NPM	Non-Pre Mixed
q	heat flux, W	PSH	Primary superheater
α	volumetric interphase heat-transfer coefficient, W/m^3K	TFM	Two fluid model
c_p	Specific heat, j/kg K	PDF	Probability density function

---

1. Introduction

Coal is one of the greatest sources of energy used for power generation, cross over the world, which is almost 40% of the total energy produced [1]. But due to limited reserves of coal the use of techniques such as co-firing coal with renewable energy resources have become increasingly popular [2]. Among the energy sources that can substitute fossil fuels, biomass fuels appear as the option with a higher worldwide potential. Power generation based on biomass holds a considerable promise in Punjab, which has huge biomass resources from crop production system and agro industries. The total biomass production in Punjab was estimated at about 54.54 million tonnes [3]. Out of the total 54.54 million tonnes, 30.26 million tonnes of biomass remain available for power generation. In Punjab there is a total potential of 2000MW of power that can be generated from the surplus biomass.

A comprehensive work on carbon capture technologies has been done in recent years in coal based plants [4]. Different CO_2-capture technologies such as pre-combustion capture, post-combustion capture and oxy-fuel combustion capture have been developed in the recent years. First two technologies can almost achieve zero-emissions from the combustion processes whereas oxy-fuel combustion technology has been widely considered as an efficient and viable option to control and reduce several types of emissions from the power plants [5]. However, Captive Power Plant, Ambuja Cement Limited is not using any carbon capture technology presently. For clear understanding of the computational analysis, chemical reactions and physical process, a number of research works have been studied. Al-Abbas et al. [6] has done CFD study of Victorian brown coal combustion in a 550 MW utility boiler under air-fired and three oxy-fuel-fired scenarios. The multi-step chemical reaction mechanisms were carried out on the pulverized lignite particles. The simplified approach of the chemical kinetics has been used to calculate the fuel and the thermal NO formation. It was found that Oxy-fuel combustion mode can significantly provide zero emissions from the existing and new build power plants. Al-Abbas et al. [7] conducted 3-D numerical simulations of pulverized dry lignite in a 100 KW test facility to simulate four different Oxy-fuel combustion environments and to investigate the temperature distribution levels, species concentrations, velocity, and particles consumption in the furnace. The commercial computational fluid dynamics (CFD), AVL Fire ver.2008.2 was used for the analysis. The simulation results of all combustion cases showed a good agreement against the experimental results in terms of temperature distribution levels and species concentrations at the most important locations of the furnace. Al-Abbas et al. [8] also undertook a computational fluid dynamics (CFD) model of the pyrolysis of a Loy Yang low-rank coal in a pressurised drop tube furnace (pdtf) for evaluating Arrhenius reaction rate constants. It was found that by modelling pyrolysis in a pdtf reactor, it was possible to determine the most suitable rate constants for a Loy Yang coal. Badzioch and Hawksley and Ubhayakar et al. were found to be most suitable constants. Werther et al. [9] explained that co-firing can be carried out in any furnace system, with some modifications in order to accommodate the nature of combustion of the agricultural residues. An important factor of consideration is the residue feeding system. Due to low bulk densities of biomass fuels, there are problems of blockage and discontinuous feeding if screw feeders are used. In such cases, pneumatic feeding systems may be considered. For all types of fluidized beds the modifications which may be required include, choosing a distributor plate which leads to better solids mixing, injection of combustion air in several stages (e.g. in the bed and in the freeboard), using swirl techniques for the injection of secondary air into the freeboard and using inclined walls in the freeboard to encourage gas recirculation

and turbulence.

In this paper, CFD analysis of a real plant fluidized bed incinerator has been done, where the coal feeding is done from the bottom and biomass is given over-feed supply. Standard k–ϵ two-phase approach has been used to model turbulence and the analysis of combustion is done by Non-Pre Mixed (NPM) approach in species model. Gas temperature distribution and species concentrations of O_2 and CO_2 were obtained during the study.

2. CFD governing equations

The governing equations used during the modelling study in FLUENT consisted of mathematical models of the gas phase and reactive chemistry. The CFD approach used in this work is based on two fluids model (TFM) in which both the solids phase and gas phase are treated as continuous. Prediction of the isothermal flow field in the computational grid is done through the solution of the equations for the conservation of mass and momentum and interphase heat exchange through energy balance equations as follows:

Mass Balance Equations:

Gas Phase:

$$\frac{\partial}{\partial t}(\varepsilon_g \rho_g) + \nabla \cdot (\varepsilon_g \rho_g v_g) = 0 \tag{1}$$

Solid Phase:

$$\frac{\partial}{\partial t}(\varepsilon_s \rho_s) + \nabla \cdot (\varepsilon_s \rho_s v_s) = 0 \tag{2}$$

Momentum Balance Equations

Gas Phase:

$$\frac{\partial}{\partial t}(\varepsilon_g \rho_g v_g) \, \nabla \cdot (\varepsilon_g \rho_g v_g) = \nabla \cdot \tau_g - \varepsilon_g \nabla p + \varepsilon_g p_g g - \beta(v_g - v_s) \tag{3}$$

Solid Phase

$$\frac{\partial}{\partial t}(\varepsilon_s \rho_s v_s) + \nabla \cdot (\varepsilon_s \rho_s v_s v_s) = \nabla \cdot \tau_s - \nabla P_s^* - \varepsilon_s \rho_s g - \beta(v_s - v_g) \tag{4}$$

Energy Balance Equations

Gas Phase:

$$\frac{\partial}{\partial t}(\varepsilon_g \rho_g h_g) + \nabla \cdot (\varepsilon_g \rho_g h_g v_g) = -\nabla \cdot \varepsilon_g \cdot q_g + \alpha(T_g - T_s) + \tau g \cdot \nabla \cdot v_g + \varepsilon_g \left[\frac{\partial}{\partial t} p + v_g \nabla p \right] \tag{5}$$

Solid Phase

$$\frac{\partial}{\partial t}(\varepsilon_s \rho_s h_s) + \nabla \cdot (\varepsilon_s \rho_s h_s v_s) = -\nabla \cdot \varepsilon_s \cdot q_s + \alpha(T_g - T_s)\tau_s \cdot \nabla \cdot v_s + \varepsilon_s \left[\frac{\partial}{\partial t} p + v_s \nabla p \right] \tag{6}$$

$$hi = \int_{Tref}^{T} c_{p.i} dT_i \quad and \quad qi = -k_i \nabla T_i \tag{7}$$

Turbulence Model: The standard *k-ε* model has become an important workforce for practical engineering flow calculations since it was proposed by Du et al. [10]. Its robustness, cost and reasonable accuracy for a wide range of turbulent flows and heat transfer simulations explain its popularity in industrial applications. The standard *k-ε* model is a semi empirical model based on model transport equations for the turbulence kinetic energy (*k*) and its dissipation rate (*ε*). The model transport equation for *k* is derived from the exact equation, while the model transport equation for *ε* was obtained using physical reasoning and bears little resemblance to its mathematically exact

counterpart.

Non – Premixed combustion model: The PDF modelling approach is considered computationally efficient method because a large number of species transport equations need not required to be unnecessarily solved. The basis of the mixture fraction approach is that, the thermo-chemical state of the fluid is related to a conserved scalar quantity known as the mixture fraction, *f*. Being a conserved scalar quantity, the value of *f* at each point in the flow domain is computed in FLUENT through the solution of the conservation equation for mean value of *f* in the turbulent flow field using following relation:

$$\frac{\partial}{\partial x_i}(\rho u_i \bar{f}) = \frac{\partial}{\partial x_i}\left(\frac{\mu_t}{\sigma_t}\frac{\partial \bar{f}}{\partial x_i}\right) + S_m \tag{8}$$

Where u_i is fluid velocity at any point in turbulent field, $\bar{f}$ is mean value of mixture fraction, μ_t is turbulent viscosity and σ_t is a constant. S_m represents the transfer of mass from reacting particles into the gas phase.

In addition to above equation, a conservation equation for the mixture fraction variance, $\overline{f'2}$ is also solved:

$$\frac{\partial}{\partial x_i}(\rho u_i \overline{f'2}) = \frac{\partial}{\partial x_i}\left(\frac{\mu_t}{\sigma_t}\frac{\partial \overline{f'2}}{\partial x_i}\right) + C_g \mu_t \left(\frac{\partial \bar{f}}{\partial x_i}\right)^2 - C_d \rho \frac{\varepsilon}{k}\overline{f'2} \tag{9}$$

Where the constants σ_t, C_g and C_d are given the default values by solver, which is FLUENT itself. The mixture fraction variance is used to describe the turbulence-chemistry interaction.

The main reactions of coal combustion can be expressed in the form of three homogeneous and three heterogeneous chemical reactions [11] as follows:

$$CH_4 + O_2 \rightarrow CO + H_2 + H_2O + heat \tag{10}$$
$$CO + H_2O \leftrightarrow CO_2 + H_2 \tag{11}$$
$$O_2 + 2H_2 \leftrightarrow 2H_2O \tag{12}$$
$$C_{char} + \tfrac{1}{2}O_2 \rightarrow CO + heat \tag{13}$$
$$C_{char} + CO_2 \rightarrow 2CO \tag{14}$$
$$C_{char} + H_2O \rightarrow CO + H_2 \tag{15}$$

3. Physical dimensions and operating conditions

Geometry generation and grid formation of CPP boiler is done in Gambit which is pre – processor of Fluent 6.3 commercial code. The furnace is of 12m height with 4m and 6.5m base dimensions. The coal feeding is done from the bottom with total sixteen ports in the bed which are equally and uniformly distributed in the four zones of the bed for convenience. Biomass is fed from four ports from a height of 1.8m from the bed. The geometry of boiler with dimensions and inside components is shown in Fig. 1. There are four biomass feed ports with (380x680) mm of dimensions are available for fuel supply. There are twelve upper secondary air ports and seven lower secondary air ports of, 55 mm diameter, for supplying excess air for complete combustion. There are three Super heaters (SH) installed inside the combustor. One is in-bed superheater having seven numbers of coils. Others are primary and secondary superheaters installed at the top of the combustor. Primary superheater (PSH) coils are having 45 mm diameter and 5 mm thickness. In-bed superheaters are having 51 mm outer diameter and 6.5 mm thickness. Different operating conditions and monitoring conditions of plant furnace are given in Table 1.

Table 1. Operating conditions and monitoring data of plant

Capacity (MW)	30	Distribution plate	Nozzle type
Type of bed	AFBC	Bed material	Crushed refractory
Bed Temperature (^{0}C)	900 – 950	Fuel used	70% coal with 30% Biomass
Bed cross-sectional area (m^2)	41	Fly-ash collector	ESP

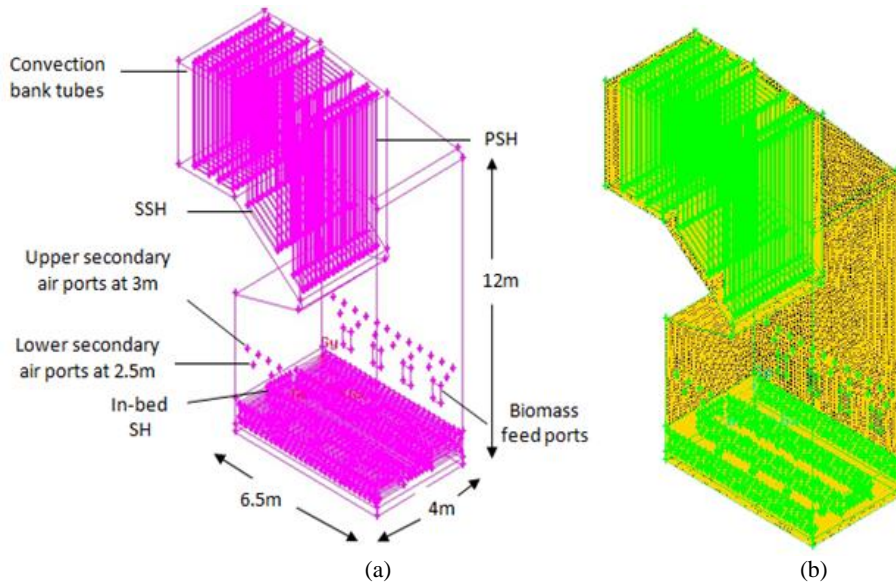| Flue gas temperature at the furnace exit temperature (^{0}C) | 850 | Fuel feed rate (T/hr) | 11 |
| Feed Water Temperature (^{0}C) | 172 | Fuel size (mm) | 5 |
| O_2 concentration at furnace outlet(molar fraction) | 0.090 | CO_2 concentration at furnace outlet(molar fraction) | 0.098 |

Fig 1: (a) Boiler geometry in GAMBIT (b) Boiler grid

4. CFD Analysis

The analysis has been done using Eulerian-multiphase model approach. In this work standard k-ε model has been used for modelling turbulence where the volumetric reaction rates have been controlled using eddy dissipation mechanism [12]. Eddy dissipation mechanism states that the reaction rate is defined by turbulence and concentrations of both reactants and products. Non premixed combustion model (NPM) has been applied to simulate combustion in which Mixture fraction/Probability density function (PDF) approach is used. This approach involves the solution of transport equations for one or two conserved scalars (the mixture fractions). Through this approach, instead of solving the transport equations for individual species, the component concentrations of species of interest are derived from the predicted mixture fraction. Therefore, the usually unknown reaction mechanism is not explicitly solved but it is treated using certain system chemistry calculations (e.g. equilibrium assumption and non-equilibrium chemistry) [13]. Physical properties of chemical species and equilibrium data are retrieved from the chemical database while the interaction of turbulence and chemistry is obtained with a probability density function or PDF. The proximate analysis and ultimate analysis values of different fuels used in are given in Table 2 and Table 3. In NPM the input is given in terms of chemical composition of fuel. NPM considers ash less and moisture less combustion [15], that is why the fractions of carbon, hydrogen, oxygen and nitrogen are calculated accordingly primarily for coal because in biomass they are having considerably very less fraction. Discrete phase modelling (DPM) approach, which is used to track particles in Lagrangian frame of reference, is the future scope of this work.

Table 2. Proximate analysis (air dried basis)

| Fuel	Moisture content	Ash content	Volatile matter	Fixed carbon
Coal	4.39	47.86	17.97	29.78

(f-grade)				
Wheat straw	6.40	12.59	71.34	9.67
Mustard straw	6.86	14.98	70.78	7.38
Rice husk	4.65	9.29	68.89	17.17

Table 3. Ultimate analysis (air dried basis)

Fuel	Elemental composition					
	C	N	H	S	O	NCV (Kcal/kg)
Coal (f-grade)	36.22	1.09	2.64	0.55	7.25	3500
Wheat straw	43.50	3.43	5.93	0.00	34.55	3400
Mustard straw	41.98	0.00	5.71	0.48	36.85	3300
Rice husk	43.10	0.00	5.33	0.00	42.27	3462

5. Results and Discussions

Simulation results of mass fraction and temperature contours of CPP boiler are shown in Fig. 2 to Fig. 4. The coal is having underfeed supply from sixteen ports which are uniformly distributed over the bed. Coal is supplied at a mass flow rate of 3.5kg/s with a mean mixture fraction of 0.373. The radial component of flow direction was taken as 0.866 and axial component of flow direction was taken as 0.5. The biomass is given overfeed supply from four feed ports at a height of 2m as shown in Fig. 1(a). The supply is given from a biomass handling plant of capacity 25TPH having vibrating screen of 25TPH. The biomass is supplied at a rate of 4.86 kg/s at a secondary mean fraction of 0.2 with the help of belt weighers to monitor the flow of biomass fuel. The axial component of flow was given the value of (−ve) 0.5 to direct the biomass in downward direction and radial component was taken as 0.866 to give a thrust to biomass fuel to drop it at the centre of the furnace for complete combustion.
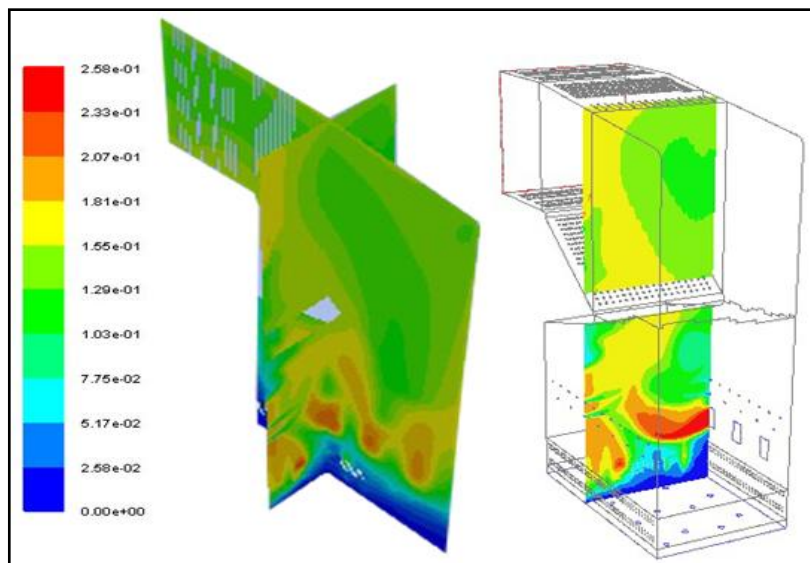
Fig 2: Mass fraction of CO_2

The flow component values have been adopted taking care of the actual process. Rest of the boundary conditions and input values are shown in Table 4.

Table 4. Boundary conditions and input values.

Mean mixture fraction of coal	0.373	Mass flow rate secondary air (kg/s)	1	Bulk density (Kg/m$^{3)}$	1100
Secondary Mean mixture fraction of biomass	0.2	Hydraulic diameter (m)	0.05	Gas density (Kg/m^3)	1.29
Velocity magnitude of primary air (m/s)	0.5	Heat transfer coefficient at in-bed SH(W/m^2-k)	20	Gas viscosity (kg/m-s)	1.72x10^{-5}
Turbulence intensity of primary air (%)	15	Internal emissivity	0.9	Convergence criteria	0.001

Mass fractions of CO_2 are shown in Fig. 2. Maximum value of CO_2 fraction was obtained at the regions where flame generation takes place due to instantaneous combustion of biomass fuel in suspension at highest range of temperature as shown in Fig. 4. CO_2 concentration was found minimum over the bed due to presence of primary air. During field study CO_2 concentration at the exit of the furnace was obtained to be 0.098 (Table1). From simulation results it was found to be 0.103. The % age change in results was found to be 4.8. O_2 mass fractions are shown in Fig. 3. O_2 concentration was found maximum at the vicinity of the bed due to supply of primary air from sixteen feed ports at 0.5 m/s. The O_2 concentration at the furnace exit was 0.090 and from model results it was obtained as 0.0932. The % age change in the actual value and model results was found to be 3.4. Temperature contours of CPP boiler are shown in Fig. 4. The way in which combustion evolves certainly affects the temperature profiles inside the furnace domain. As discussed earlier the hottest area of the furnace can be found where the greatest part of the char is converted to CO_2 [14]. Consequently, maximum temperatures were found, at the regions, where CO_2 generation was maximum. It is also to note that the O_2 concentration decreases rapidly where greater amount of fuel is burnt (Fig 3). In the vicinity of the bed the temperature contours were obtained up to 1200K (987^{0}C) as shown in Fig. 4. The actual bed temperatures vary up to 950^{0}C. The % age change in both the results was found 3.7. Flue gas temperature at the furnace exit was 850^{0}C. The temperature obtained from model results is 1140K (867^{0}C). The change in the experimental value and model results was found to be 1.9%.
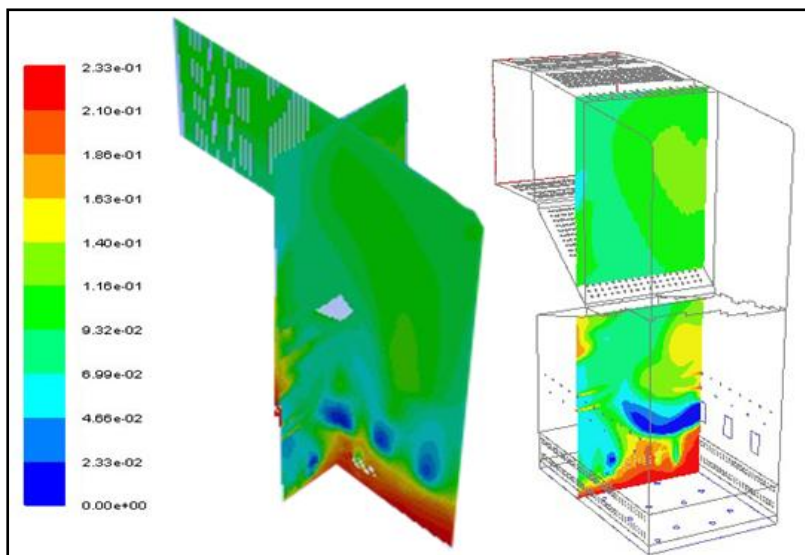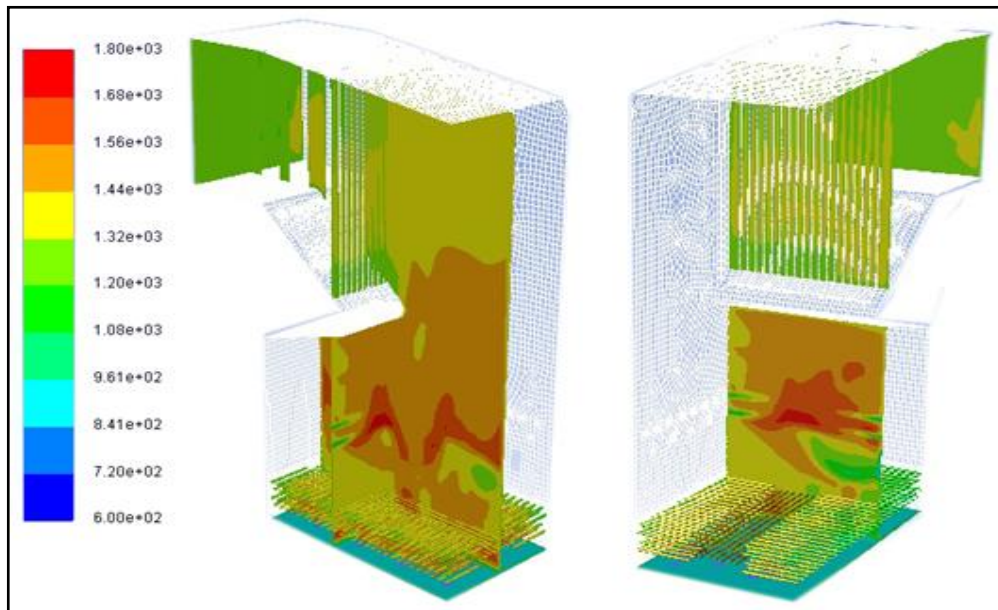

Fig 3: Mass fraction of O_2

Fig 4: Temperature contours

6. Conclusions

In the present study a real plant fluidized bed incinerator was opted for thorough understanding of fluidized bed combustion process. Three dimensional CFD modelling of plant furnace, based on actual operating conditions and input data, was done to study temperature field and species concentration of O_2 and CO_2 over the entire domain of furnace. Modelling results provided useful information about these parameters over the entire domain, especially in the regions where measurements are impossible to obtain. Simulation results were compared with monitoring data and the differences between both the values were found in the range of 1.9% to 4.8%, from which it is concluded that the simulation results are in agreement with real process behaviour and reported literature.

Acknowledgements

References

[1]   IEA, Power generation from coal – ongoing developments and outlooks, (2011) France.
[2]   S. Van Loo, J. Koppejan (Eds.), The handbook of biomass combustion and co-firing, Earthscan (2008) London.
[3]   G.Kaur, J.Singh, A.Sood, Power generation potential from crop biomass in Punjab, Agricultural Engineering Today 30 (2006) 5-6.
[4]   N. Nikolopoulos, A. Nikolopoulos, E. Karampinis, P. Grammelis, E. Kakaras, Numerical investigation of the oxy-fuel combustion in large scale boilers adopting the ECO-Scrub technology, Fuel 90 (2011)198–214.
[5]   A.H. Al-Abbas, J. Naser, Numerical study of one air-fired and two oxy-fuel combustion cases of propane in a 100 kW furnace, Energy & Fuels 26 (2012) 952-967.
[6]   A.H. Al-Abbas, J. Naser, D. Dodds, CFD modelling of air-fired and oxy-fuel combustion in a large-scale furnace at Loy Yang A brown coal power station, Fuel 102 (2012) 646-665.
[7]   A.H. Al-Abbas, J. Naser, D.Dodds, CFD modelling of air-fired and oxy-fuel combustion of lignite in a 100KW furnace, Fuel 90 (2011) 1778-1795.
[8]   A.H. Al-Abbas, J. Hart, J. Naser, Numerical investigation of pyrolysis of a Loy Yang coal in a lab-scale furnace at elevated pressures, Heat Mass Transfer 49 (2013) 1725-1732.
[9]   J.Werther, M.Saenger, E.U Hartge , T. Ogada, Z.Siagi, Combustion of agricultural residues, Prog Energy Combust Sci 26

(2000) 1–27.

[10] W.Du, B. Xiaojun, X.Jian, W.Weisheng, Computational fluid dynamics (CFD) modeling of spouted bed: Influence of frictional stress, maximum packing limit and coefficient of restitution of particles, Chem. Eng. Sci. 61(2006) 4558-4570.

[11] A.H. Al-Abbas, J. Naser, Effect of chemical reaction mechanisms and NO x modeling on air-fired and oxy-fuel combustion of lignite in a 100-kW furnace, Energy & Fuels 26 (2012) 3329-3348.

[12] R.I. Singh, A. Brink, M. Hupa, CFD modeling to study fluidized bed combustion and gasification, App. Thermal Engg. 52 (2013) 585-614.

[13] M.Rozainee, S.P.Ngo, A.A. Salema, K.G. Tan KG, Computational fluid dynamics modeling of rice husk combustion in a fluidized bed combustor, Powder Technol 203(2010) 331-347.

[14] FLUENT user's guide (2006). Vols. 1–2. Lebanon.

[15] S. Ravelli, A. Perdichizzi, G. Barigozzi, Description, applications and numerical modeling of bubbling fluidized bed combustion in waste-to-energy plants, Prog Energy Combust Sci 34 (2008) 224-253.

6th BSME International Conference on Thermal Engineering (ICTE 2014)

Similarity Solution of Heat and Mass Transfer Flow over an Inclined Stretching Sheet with Viscous Dissipation and Constant Heat Flux in Presence of Magnetic Field

Mohammad Ali[a,*], Md. Abdul Alim[b], Mohammad Shah Alam[c]

[a,c]Chittagong University of Engineering & Technology, Department of Mathematics, Chittagong -4349, Bangladesh
[b]Bangladesh University of Engineering & Technology, Department of Mathematics, Dhaka -1000, Bangladesh

Abstract

The present analysis of this paper is to examine the similarity solution of magnetohydrodynamics (MHD) free convection heat and mass transfer flow of an incompressible, electrically conducting and viscous fluid over an inclined stretching sheet with viscous dissipation and constant heat flux. So the present work is focused of the impact of the flow parameters on the velocity, temperature, and concentration are computed, discussed and have been graphically represented in figures and also the shearing stress, and rate of concentration shown in table 1 for various values of different parameters. The results presented graphically illustrate that velocity field decrease due to increasing of magnetic parameter, Prandtl number, Grashof number, and Eckert number whereas negligible increasing effects for Soret number, Schmidt number and noticeable increasing effect for angle of inclination but there is no effect for modified Grashof number. The temperature field decreases up to certain interval then increases in the presence of Magnetic parameter and reverse trend arise for Prandtl number but the temperature field increases for the remaining entering parameters. It is interesting to note that in a certain interval of η, the concentration profile is decreased and then increased but reverse trend arises in the case of Prandtl number and angle of inclination. By considering the hot plate the numerical results for the skin friction and the local Sherwood number are compared with the results reported by the other author when the magnetic field and modified Grashof number are absent. The present results in this paper are in good agreement with the work of the previous author.

Keywords: MHD; heat and mass transfer; stretching sheet: angle of inclination; viscosity;

* Corresponding author. Mob: +8801713109929.
E-mail address: ali.mehidi93@gmail.com

1. Introduction

The steady MHD boundary layer flow over an inclined stretching sheet with suction and heat generation has much interested in last few decades. The effects of magnetic field on free convective flows are of importance in liquid metals, electrolytes, and ionized gases. Due to presence of a strong magnetic field the conduction mechanism in ionized gases is different from that in a metallic substance. An electric current in ionized gases is generally carried out by electrons which undergo successive collisions with other charged or neutral particles. However, in the presence of a strong electric field, the electrical conductivity is affected by a magnetic field. Also MHD laminar boundary layer flow over a stretching sheet has noticeable applications in glass blowing, continuous casting, paper production, hot rolling, wire drawing, drawing of plastic films, metal and polymer extrusion, metal spinning and spinning of fibbers. During its manufacturing process a stretched sheet interacts with the ambient fluid thermally and mechanically. Both the kinematics of stretching and the simultaneous heating or cooling during such processes has a decisive influence on the quality of the final products. In the extrusion of a polymer sheet from a die, the sheet is some time stretched. By drawing such a sheet in a viscous fluid, the rate of cooling can be controlled and the final product of the desired characteristics can be achieved. Raptiset et al. [1] have studied the viscous flow over a non-linearly stretching sheet in the presence of a chemical reaction and magnetic field. Tan et al. [2] studied various aspects of this problem, such as the heat, mass and momentum transfer in viscous flows with or without suction or blowing. Abel and Mahesh [3] presented an analytical and numerical solution for heat transfer in a steady laminar flow of an incompressible viscoelastic fluid over a stretching sheet with power-law surface temperature, including the effects of variable thermal conductivity and non-uniform heat source and radiation. Samad and Mohebujjaman [4] investigated the case along a vertical stretching sheet in presence of magnetic field and heat generation. Saleh Alharbi et.al [5] studied heat and mass transfer in MHD visco-elastic fluid flow through a porous medium over a stretching sheet with chemical reaction, Seddeek and Abdel Meguid [6] analyzed the effects of radiation and thermal diffusivity on heat transfer over a stretching surface with variable heat flux , Ali et al. [7] studied the Radiation and thermal diffusion effects on a steady MHD free convection heat and mass transfer flow past an inclined stretching sheet with Hall current and heat generation, Ibrahim and Shanker [8] investigated the unsteady MHD boundary layer flow and heat transfer due to stretching sheet in the presence of heat source or sink by Quasi-linearization technique. Ishak et al. [9] investigated the solution to unsteady mixed convection boundary layer flow and heat transfer due to a stretching vertical surface. Ebashbeshy and Aldawody [10] analyzed heat transfer over an unsteady stretching surface with variable heat flux in presence of heat source or sink, Fadzilah et al.[11] studied the steady MHD boundary layer flow and heat transfer of a viscous and electrically conducting fluid over a stretching sheet with an induced magnetic field, Rashidi et al. [12] find the solution of MHD flow in a laminar liquid film from a horizontal stretching surface by using differential transform method and Padé Approximant, later Rashidi et al. [13] showed a new analytical study of MHD stagnation–point flow in porous media with heat transfer also Rashidi et al. [14] studied the simultaneous effects of partial slip and thermal-diffusion and diffusion-thermo on steady MHD convective flow due to a rotating disk and Mohebujjaman et al. [15] studied MHD heat transfer mixed convection flow along a vertical stretching sheet with heat generation using shooting technique. All of the above researchers in their studies were not consider the inclination of angle of the sheet, viscous dissipation and constant heat flux. So the present work focused on similarity solution of heat and mass transfer flow over an inclined stretching sheet with viscous dissipation and constant heat flux in presence of magnetic field.

2. Mathematical formulation of the problem and similarity analysis

Let us consider a steady two dimensional laminar MHD viscous incompressible electrically conducting fluid along an inclined stretching sheet with an acute angle (γ), X- direction is taken along the leading edge of the inclined stretching sheet and Y is normal to it and extends parallel to X-axis. A magnetic field of strength B_0 is introduced to the normal to the direction to the flow. The uniform plate temperature T_w ($>T_\infty$), where T_∞ is the temperature of the fluid far away from the plate. Let u and v be the velocity components along the X and Y axis respectively in the boundary layer region. Under the above assumptions and usual boundary layer approximation, the dimensional governing equations of continuity, momentum, concentration and energy under the influence of externally imposed magnetic field are:

Equation of continuity:

$$\frac{\partial u}{\partial x} + \frac{\partial v}{\partial y} = 0 \tag{1}$$

Momentum equation:

$$u\frac{\partial u}{\partial x} + v\frac{\partial u}{\partial y} = v\frac{\partial^2 u}{\partial y^2} + g\beta(T - T_\infty)\cos\gamma + g\beta^*(C - C_\infty)\cos\gamma - \frac{\sigma B_0^2 u}{\rho} \tag{2}$$

Energy Equation:

$$u\frac{\partial T}{\partial x} + v\frac{\partial T}{\partial y} = \alpha\frac{\partial^2 T}{\partial y^2} + \frac{v}{c_p}\left(\frac{\partial u}{\partial y}\right)^2, \alpha = \frac{k}{\rho c_p} \tag{3}$$

Concentration Equation:

$$u\frac{\partial C}{\partial x} + v\frac{\partial C}{\partial y} = D_m\frac{\partial^2 C}{\partial y^2} + \frac{D_m K_T}{T_m}\frac{\partial^2 T}{\partial y^2} \tag{4}$$

where u and v are the velocity components along x and y directions, T, T_w and T_∞ are the fluid temperature, the stretching sheet temperature and the free stream temperature respectively while C, C_w and C_∞ are the corresponding concentrations, k is the thermal conductivity of the fluid, C_p specific heat with constant pressure, α is thermal diffusivity, γ is the angle of inclination, μ is the coefficient of viscosity, v is the kinematic viscosity, σ is the electrical conductivity, ρ is the fluid density, β is the thermal expansion coefficient, $\beta*$ is the concentration expansion coefficient, B_0 is the magnetic field intensity, U_0 is the stretching sheet parameter, g is the acceleration due to gravity, q is the constant heat flux per unit area, D_m is the coefficient of mass diffusivity, K_T is the thermal diffusion ratio, T_m is the mean fluid temperature, respectively. The above equations are subject to the following boundary conditions:

$$u = U_0 x, \ v = 0, \ \frac{\partial T}{\partial y} = -\frac{q}{k}, C = C_w \ \ at \ \ y = 0 \ and \ \ u = 0, T = T_\infty, C = C_\infty \ as \ \ y \to \infty \tag{5}$$

Introducing the stream function $\psi(x,y)$ as defined by $u = \frac{\partial \psi}{\partial y}$ and $v = -\frac{\partial \psi}{\partial x}$

To convert the governing equations into a set of similarity equations, we introduce the following similarity transformation:

$$\psi = x\sqrt{2v\,U_0}\,f(\eta), \eta = y\sqrt{\frac{U_0}{2v}}, \ \theta(\eta) = \frac{k(T - T_\infty)}{q}\sqrt{\frac{U_0}{2v}}, \varphi(\eta) = \frac{C - C_\infty}{C_w - C_\infty}$$

From the above transformations, the non-dimensional, nonlinear and coupled ordinary differential equations are obtained as follows:

$$f''' + 4ff'' - 2f'^2 - Mf' + Gr\theta\cos\gamma + Gm\varphi\cos\gamma = 0 \tag{6}$$

$$\theta'' + 4\Pr f\theta' + \Pr Ecf''^2 = 0 \tag{7}$$

$$\varphi'' + 4Scf\varphi' + ScS_0\theta'' = 0 \tag{8}$$

The transform boundary conditions:

$$f = 0 \ f' = 1, \theta' = -1, \varphi = 1 \ at \ \eta = 0, \ and \ f' = 0, \theta = \varphi = 0 \ as \ \eta \to \infty \tag{9}$$

Where f', θ and φ are the dimensionless velocity, temperature and concentration respectively, η is the similarity variable, η_∞ is the value of η at which boundary conditions is achieved, the prime denotes differentiation with respect to η. Also

$$M = \frac{2\sigma B_0^2}{\rho U_0}, Gr = \frac{2g\beta q}{U_0^2}\sqrt{\frac{2v}{xU_0}}, Gm = \frac{2g\beta^*(C_w - C_\infty)}{xU_0^2}, \Pr = \frac{\mu c_p}{k}, Ec = \frac{kU_0^2 x^2}{qc_p}\sqrt{\frac{U_0}{2v}}, Sc = \frac{v}{D_m}$$

$$and \ S_0 = \frac{D_m K_T q}{kT_m(C_w - C_\infty)}\sqrt{\frac{2}{vU_0}}$$

are the magnetic parameter, Grashof number, modified Grashof number, Prandtl number, Eckert number, Schmidt number, and Soret number respectively. The important physical quantities of this problem are skin friction coefficient C_f and the local Sherwood number Sh which are proportional to rate of velocity and rate of concentration respectively.

3. Methodology

There are two asymptotic boundary conditions and hence two unknown conditions $f'(0), \theta'(0)$ are to be assumed to solve the boundary layer equations by using shooting method technique. Within the context of initial value method and Nachtsheim-Swigert iterations technique the outer boundary conditions may be functionally represented as:

$$f(\eta_{max}) = f \ [f'(0), \theta'(0)] = \delta_1 \tag{10}$$

$$\theta(\eta_{max}) = \theta \ [f'(0), \theta'(0)] = \delta_2 \tag{11}$$

with the asymptotic convergence criteria given by:

$$f'(\eta_{max}) = f' \ [f'(0), \theta'(0)] = \delta_3 \tag{12}$$

$$\theta'(\eta_{\max}) = \theta' \, [f'(0), \theta'(0)] = \delta_4 \tag{13}$$

Let us choose $f'(0) = \Delta x, \ \theta'(0) = \Delta y$

Retaining only the first order terms from the Taylor's Series expansion from equations (10) – (13) yields:

$$f(\eta_{\max}) = f_c(\eta_{\max}) + f_x \Delta x + fy \, \Delta y = \delta_1 \tag{14}$$

$$\theta(\eta_{\max}) = \theta_c(\eta_{\max}) + \theta_x \Delta x + \theta y \, \Delta y = \delta_2 \tag{15}$$

$$f'(\eta_{\max}) = f'_c(\eta_{\max}) + f'_x \Delta x + f'y \, \Delta y = \delta_3 \tag{16}$$

$$\theta'(\eta_{\max}) = \theta'_c(\eta_{\max}) + \theta'_x \Delta x + \theta'y \, \Delta y = \delta_4 \tag{17}$$

where $x = f'(0), \ y = \theta'(0)$ and x, y are subscripts.

Indicate partial differentiation, e. g.:

$$f'_x = \frac{\partial f'(\eta_{\max})}{\partial f'(0)}, \ f'_y = \frac{\partial f'(\eta_{\max})}{\partial \theta'(0)}$$

The subscript 'c' indicates the value of the function at $\eta_{\max}$ determined from the trial integration. Solutions of these equations in a least square sense requires determining the minimum value of

$$E = \delta_1^2 + \delta_2^2 + \delta_3^2 + \delta_4^2 \tag{18}$$

Differentiation E with respect to x and y we get

$$\delta_1 \frac{\partial \delta_1}{\partial x} + \delta_2 \frac{\partial \delta_2}{\partial x} \delta_3 \frac{\partial \delta_3}{\partial x} \delta_4 \frac{\partial \delta_4}{\partial x} = 0 \tag{19}$$

$$\delta_1 \frac{\partial \delta_1}{\partial y} + \delta_2 \frac{\partial \delta_2}{\partial y} \delta_3 \frac{\partial \delta_3}{\partial y} \delta_4 \frac{\partial \delta_4}{\partial y} = 0 \tag{20}$$

using equations (14) –(17) in equation (19), we get

$$(f_x^2 + \theta_x^2 + f_x'^2 + \theta_x'^2) \, \Delta x + (f_x f_y + \theta_x \theta_y + f_x' f_y' + \theta_x' \theta_y') \, \Delta y = -(f_c f_x + \theta_c \theta_x + f_c' f_x' + \theta_c' \theta_x') \tag{21}$$

Similarly using equations (14) – (17) in equation (20), we get

$$(f_y^2 + \theta_y^2 + f_y'^2 + \theta_y'^2) \, \Delta y + (f_x f_y + \theta_x \theta_y + f_x' f_y' + \theta_x' \theta_y') \, \Delta x = -(f_c f_y + \theta_c \theta_y + \theta_c' \theta_y' + f_c' f_y') \tag{22}$$

we can write equation (21) and (22) in system of linear equations in the following form as:

$$a_{11}\Delta x + a_{12}\Delta y = d_1 \tag{23}$$

$$a_{21}\Delta x + a_{22}\Delta y = d_2 \tag{24}$$

where, $a_{11} = f_x^2 + \theta_x^2 + f_x'^2 + \theta_x'^2$

$$a_{12} = f_x f_y + \theta_x \theta_y + f_x' f_y' + \theta_x' \theta_y'$$

$$a_{21} = f_y^2 + \theta_y^2 + f_y'^2 + \theta_y'^2$$

$$a_{22} = f_x f_y + \theta_x \theta_y + f_x' f_y' + \theta_x' \theta_y'$$

$$d_1 = -(f_c f_x + \theta_c \theta_x + f_c' f_x' + \theta_c' \theta_y')$$

$$d_2 = -(f_c f_y + \theta_c \theta_y + \theta_c' \theta_y' + f_c' f_y')$$

The matrix from of (23) and (24) is

$$\begin{pmatrix} a_{11} & a_{12} \\ a_{21} & a_{22} \end{pmatrix} \begin{pmatrix} \Delta x \\ \Delta y \end{pmatrix} = \begin{pmatrix} d_1 \\ d_2 \end{pmatrix} \tag{25}$$

We will solve the system of linear equations (25) by Cramers rule and thus we have

$$\Delta x = \frac{\det A_1}{\det A}, \quad \Delta y = \frac{\det A_2}{\det A}$$

where, $\det A = \begin{vmatrix} a_{11} & a_{12} \\ a_{21} & a_{22} \end{vmatrix} = a_{11}a_{22} - a_{12}a_{21}$

$$\det A_1 = \begin{vmatrix} d_1 & a_{12} \\ d_2 & a_{22} \end{vmatrix} = d_1 a_{22} - d_2 a_{12}$$

$$\det A_2 = \begin{vmatrix} a_{11} & d_1 \\ a_{21} & d_2 \end{vmatrix} = d_2 a_{11} - d_1 a_{21}$$

Then we obtain the unspecified missing values x and y as $x \equiv x + \Delta x$ and $y \equiv y + \Delta y$

Thus adopting this type of numerical technique described above, a computer program will be setup for the solution of the basic nonlinear differential equations of our problem where the integration technique will be adopted as the fourth order Runge-Kutta method along with shooting iterations technique. First of all, higher order non–linear differential equations are converted into simultaneous linear differential equations of first order and they are further

transformed into initial value problem applying the shooting technique. Once the problem is reduced to initial value problem, then it is solved using Runge -Kutta fourth order technique. The effects of the flow parameters on the velocity, temperature and species concentration are computed, discussed and have been graphically represented in figures and also the shearing stress and rate of concentration shown in table 1 for various value of different parameters. In this regard, defining new variables by the equations

$$y_1 = f, y_2 = f', y_3 = f'', y_4 = \theta, y_5 = \theta', y_6 = \varphi, y_7 = \varphi'$$

The higher order differential equations (6), (7), (8) and boundary conditions (9) may be transformed to seven equivalent first order differential equations and boundary conditions respectively are given below:

$$dy_1 = y_2, dy_2 = y_3, dy_3 = -4y_1y_3 + 2y_2^2 + My_2 - Gr\cos\gamma \, y_4 - Gm\cos\gamma \, y_6, dy_4 = y_5,$$

$$dy_5 = -4\Pr y_1 y_5 - \Pr Ec y_3^2, dy_6 = y_7, dy_7 = -4Sc y_1 y_7 + 4Sc S_0 \Pr y_1 y_5 + Sc S_0 \Pr Ec y_3^2$$

And the boundary conditions are

$$y_1 = 0, y_2 = 1, y_5 = \text{-}1, y_6 = 0 \ \ at \ \eta = 0, \ and \ y_2 = 0, y_4 = 0, y_6 = 0 \ \ as \ \ \eta \to \infty$$

4. Results and Discussion

Numerical calculation for the distribution of velocity, temperature and concentration profiles across the boundary layer for different values of the parameters are carried out. For the purpose of our simulation we have chosen *M = 0.5, S0= 0.2, Pr = 1.0, Gr = 2.0, Gm=2.0, Ec = 1.0, Sc= 0.22, and γ= 81ᵒ* while the parameters are varied over range as shown in the figures. Fig.1 clearly demonstrates that the velocity profile starts from maximum value at the surface and then decreasing until it reaches to the minimum value at the end of the boundary layer for all the values *M*. It is interesting to note that the effect of magnetic field is more prominent at the point of peak value, because the presence of *M* in an electrically conducting fluid introduces a force like Lorentz force which acts against the flow if the magnetic field is applied in the normal direction as in the present problem. As a result velocity profile is decreased. Similar effect is also observed in Fig. 2 and Fig. 5 with increasing values of *Gr* and *Ec*. Fig. 4, Fig. 6 and Fig.7 show the velocity profile for various values of *S₀, Sc* and *γ*, it is observed that an increasing in Soret number and Schmidt number lead to a negligible increasing effect on velocity profile whereas noticeable increasing effect for angle of inclination because of multiplication *cosγ* the effect of the buoyancy force increases for the increasing values of *γ* and therefore the velocity profile increases. But there is no effect of modified Grashof number on velocity profile which are shown in Fig. 3. Again, Fig. 8 − Fig. 14 show the temperature profile obtained by the numerical simulation for various values of entering parameters. From these figures it is clearly demonstrates that the thermal boundary layer thickness increases for the increasing values of *S0, Pr, Gr, Gm, Ec, Sc*. From Fig. 8 it is observed that in the certain interval of *η*, the temperature profile is increased and then decreased for increasing values of *M* which implies that the applied magnetic field normal to the flow of the fluid tends to heat the fluid and thus reduces the heat transfer rate from the sheet therefore temperature is increased but reverse trend arises for the increasing values of *Pr* which shown in Fig.14. That is, the thermal boundary layer thickness decreases as the *Pr* increases implying higher heat transfer. It is due to the fact that smaller values of *Pr* means increasing thermal conductivity and therefore it is able to diffuse away from the plate more quickly than higher values of *Pr*, hence the rate of heat transfer is reduced as a result the heat of the fluid in the boundary layer increases. The effect of *Gr* on temperature profile is shown in Fig. 9. From this figure it is observed that, the temperature profile increases for increasing values of *Gr*; because the increase of Grashof number results in the increase of temperature gradients, which leads to the enhancement of the velocity due to the enhanced convection and thus temperature profiles are increased. From Fig.12 it is seen that the temperature profile is increased for the increasing values of *Ec* due to the fact that heat energy is stored in the liquid due to the frictional heating. It is obvious that the increasing effect of *Ec* enhanced the temperature at any point of flow region for the case of salt water. From this figure it is concluded that greater viscous dissipative heat be the cause of increasing temperature profile. Again Fig.15-Fig. 22 shows the

concentration profiles obtained by the numerical simulation for various values of entering non-dimensional parameters. Again, from Fig.15- Fig.18 and Fig. 22 it is observed that in a certain interval of η, the concentration profile is decreased and then increased it is due to the fact that the concentration buoyancy effects to decrease compliant a reduction in the fluid velocity. Thus the simultaneous reduction effects of velocity and concentration reduced the velocity and concentration boundary layer thickness but reverse trend arises in the case of *Pr* and *γ* are shown in Fig. 20 and Fig. 21. From Fig.19 it is seen that the concentration profile is increased for the effect of *Ec* due to the fact that heat energy is stored in the liquid due to the frictional heating. It is obvious that the increasing effect of *Ec* enhanced the concentration at any point of flow region for the case of salt water. From this figure it is concluded that greater viscous dissipative heat be the cause of increasing concentration profile. Further the numerical solutions for the skin friction and the local Sherwood number have been compared with those of D. Makinde [16].These results are given in Table.1 and it is observed that the present results and those of D. Makinde [16] are in good agreement.

5. Conclusions

Following are the conclusions made from above analysis:

- The magnitude of velocity decreases with increasing magnetic parameter causing of Lorentz force.
- It is interesting to note that, in the certain interval of η, the temperature profile is increased and then decreased for increasing values of *M* but reverse trend arises for the increasing values of Pr.
- The noticeable increasing effects of Prandtl number, Schmidt number, Eckert number and angle of inclination on concentration profile but reverse trend arises for the case of Grashof number, modified Grashof number and Soret number.
- To compare the skin friction and Sherwood number with previous results and get good agreement.

Table 1.Comparison of skin friction [$f''(0)$] and local Sherwood number [$-\varphi'(0)$] for different values of *M*, when *Pr = 1.0, Gr = -0.2, Gm = -0.2, S_0 = 0.2, Ec = 1.0, Sc = 0.22, γ = 81°*

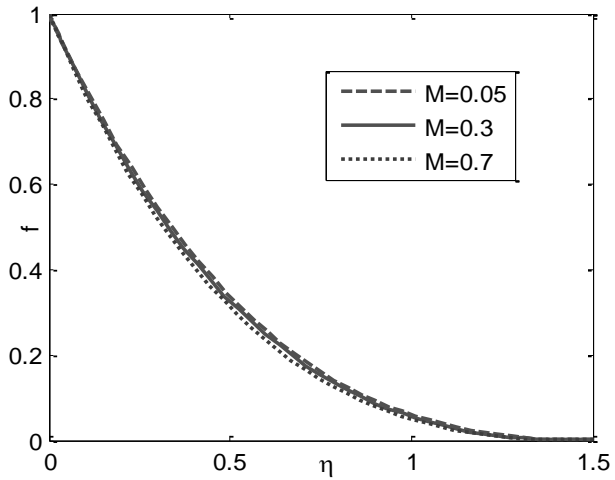| M	D. Makinde [16]		Present results	
	$-f''(0)$	$-\varphi'(0)$	$-f''(0)$	$-\varphi'(0)$
1.00	1.629178	0.561835	**1.619956**	**0.560545**
2.00	1.912620	0.554247	**1.912023**	**0.554767**
5.00	2.581130	0.541547	**2.57678**	**0.543557**
10.00	3.415289	0.531405	**3.422358**	**0.532425**

Fig.1. Velocity profile for various values of M
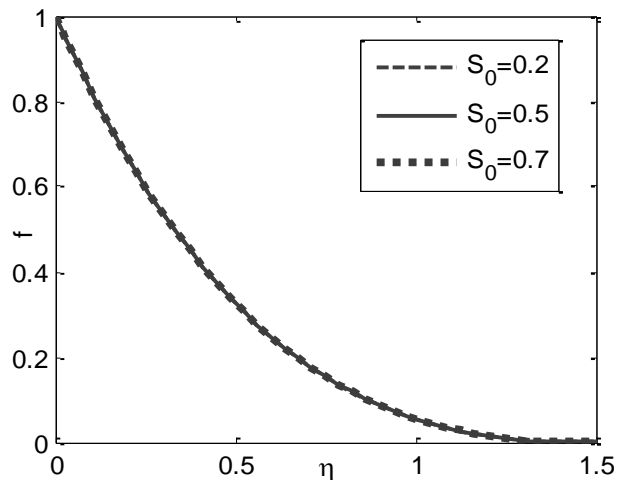
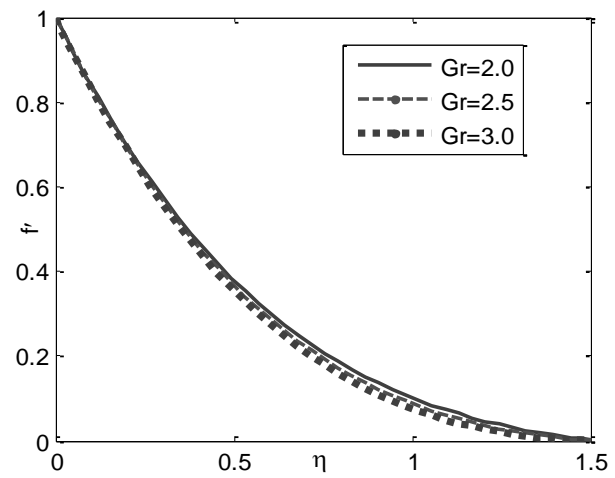Fig.4. Velocity profile for various values of S_0

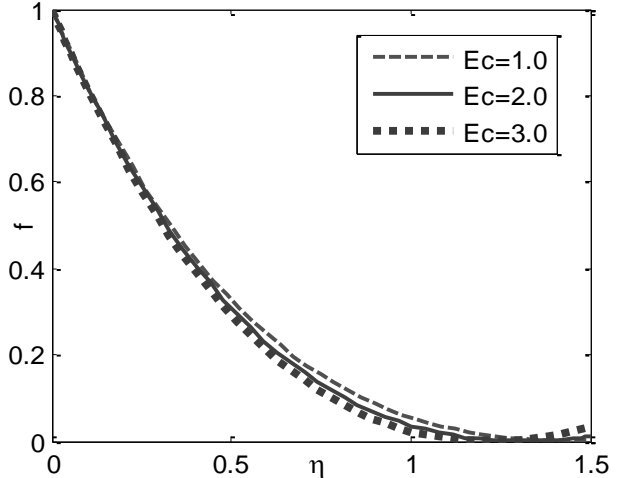Fig.2. Velocity profile for various values of Gr

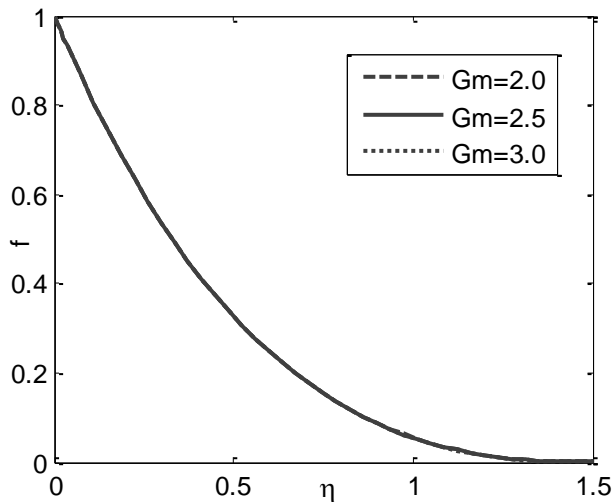Fig.5. Velocity profile for various values of Ec

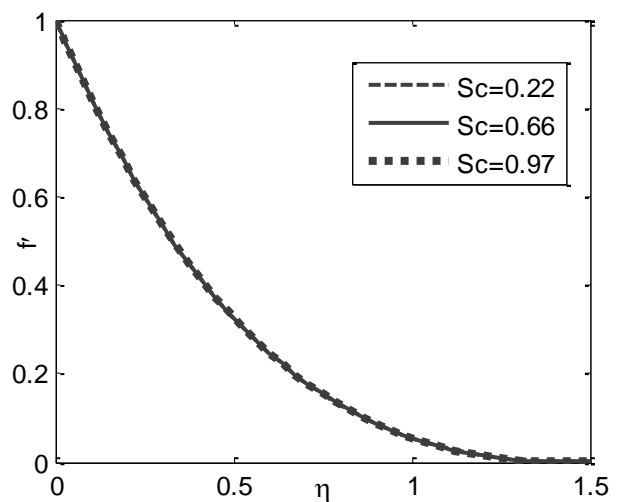Fig.3. Velocity profile for various values of Gm
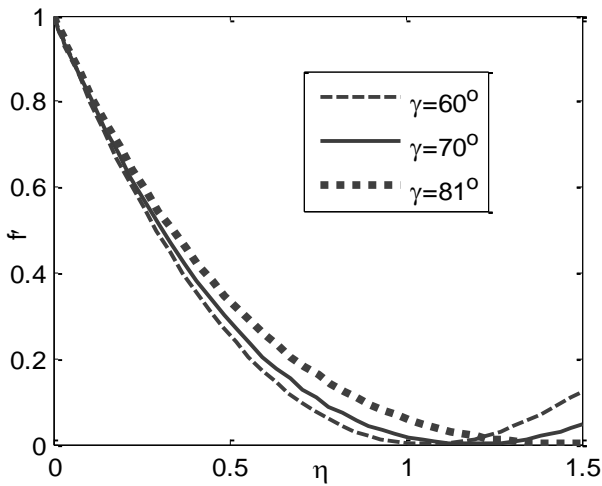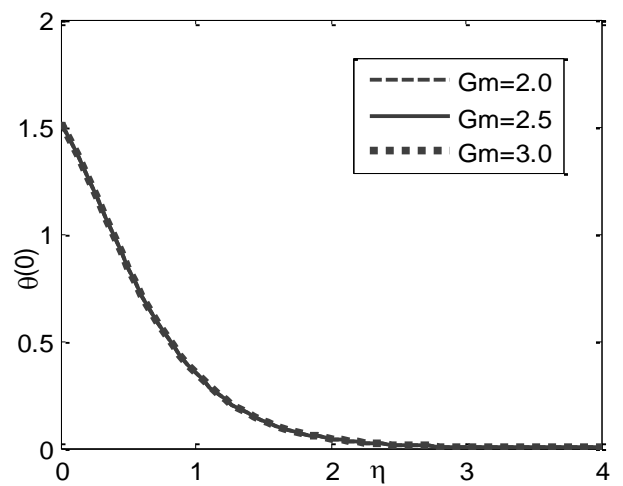
Fig.6. Velocity profile for various values of Sc

Fig.7. Velocity profile for various values of   γ
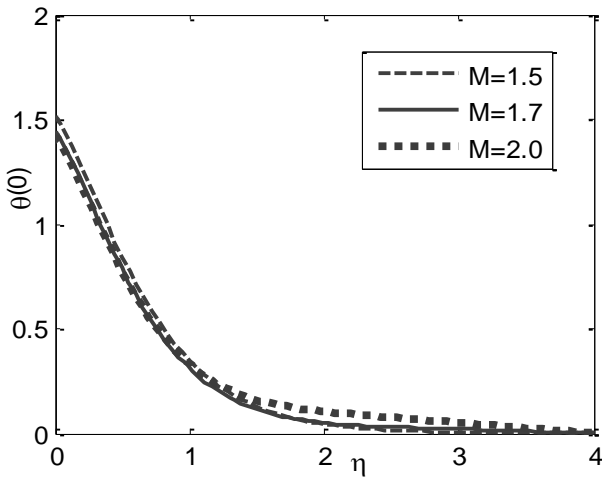

Fig.10. Temperature profile for various values of   Gm

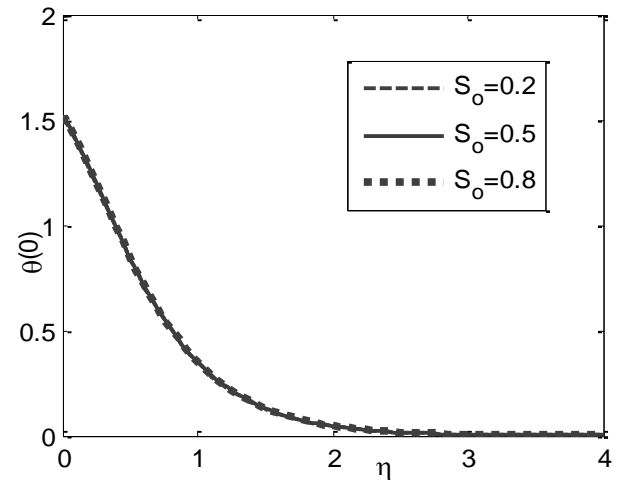Fig.8. Temperature profile for various values of   M

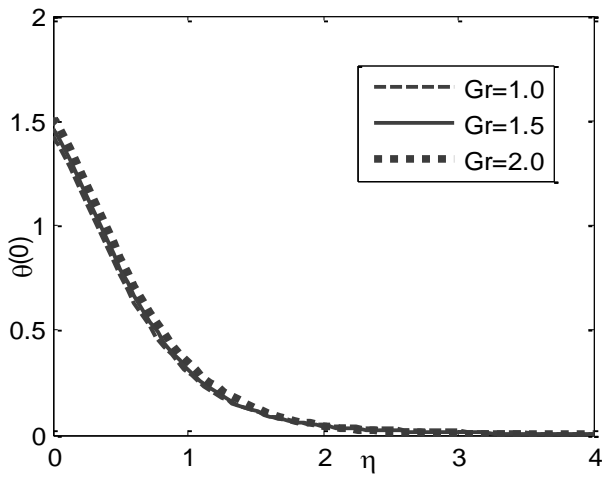Fig.11. Temperature profile for various values of   S0

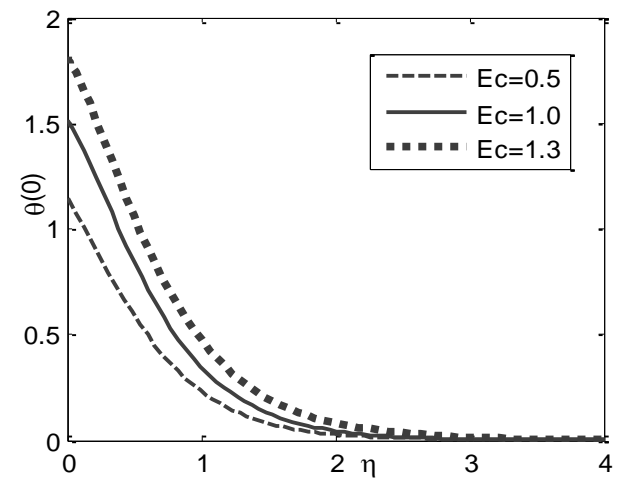Fig.9. Temperature profile for various values of   Gr

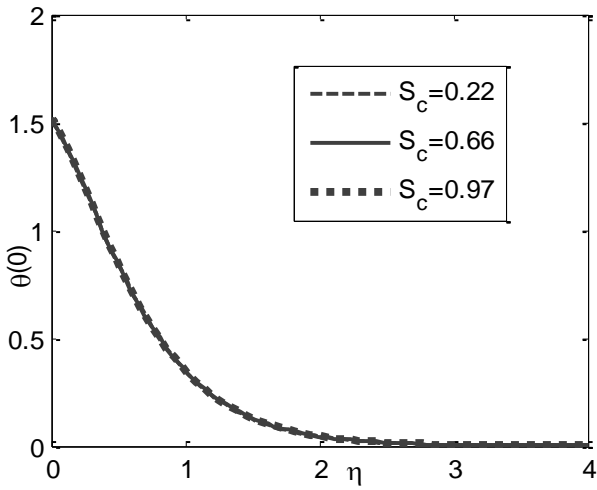Fig.12. Temperature profile for various values of   Ec

Fig.13. temperature profile for various values of   Sc
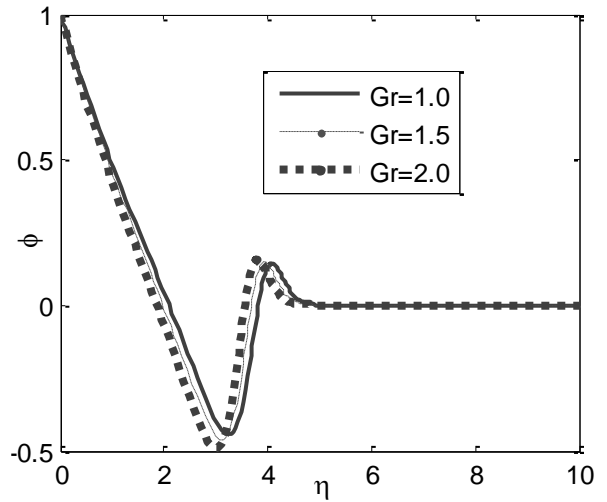

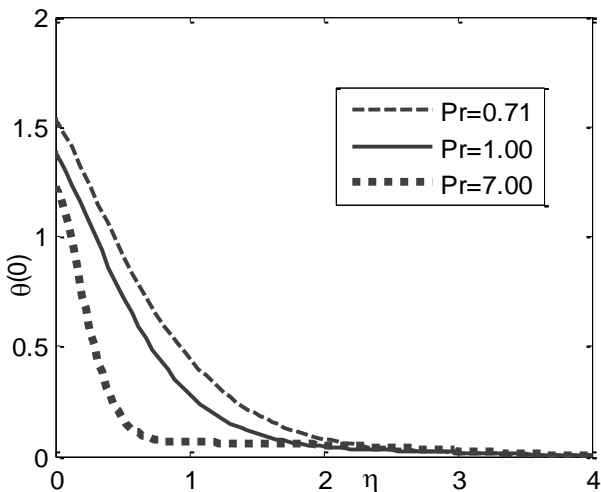Fig.16. Concentration profile for various values of   Gr
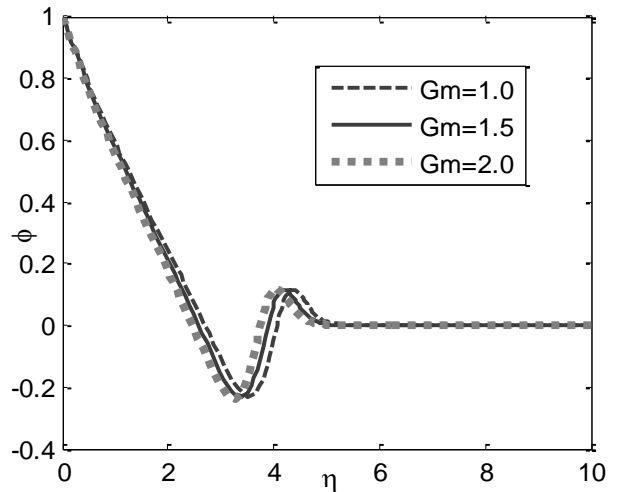

Fig.14. Temperature profile for various values of   Pr

Fig.17. Concentration profile for various values of   Gm
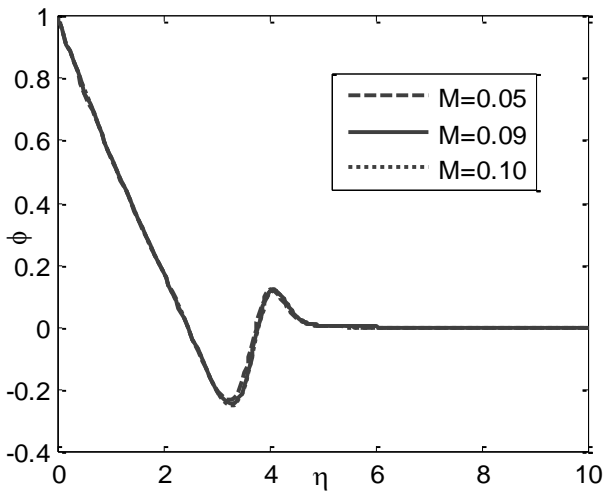

Fig.15. Concentration profile for various values of   M
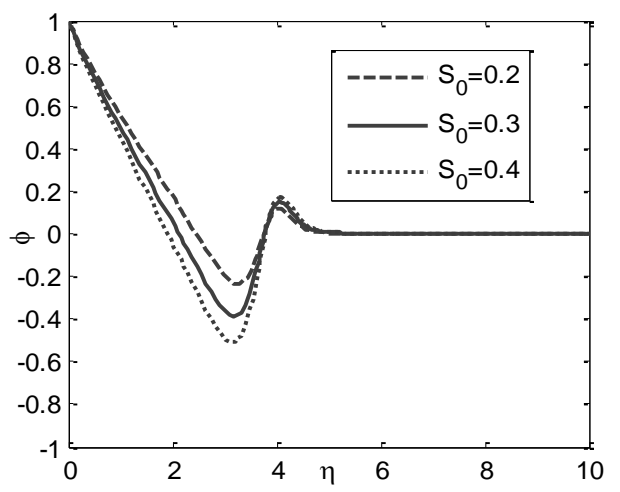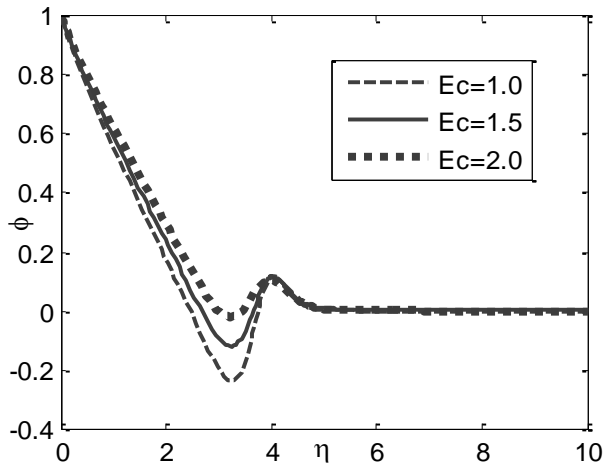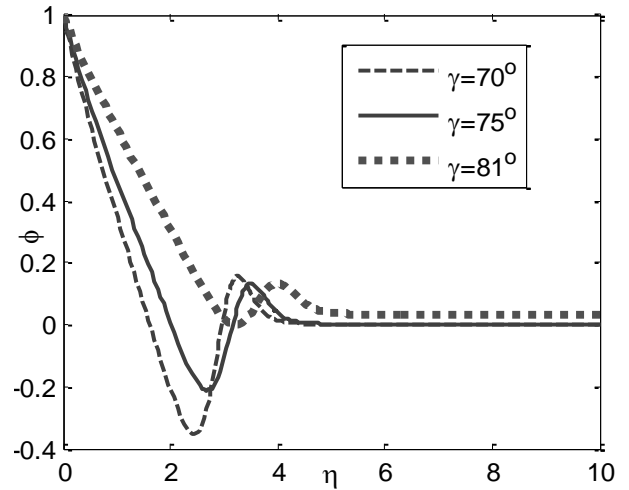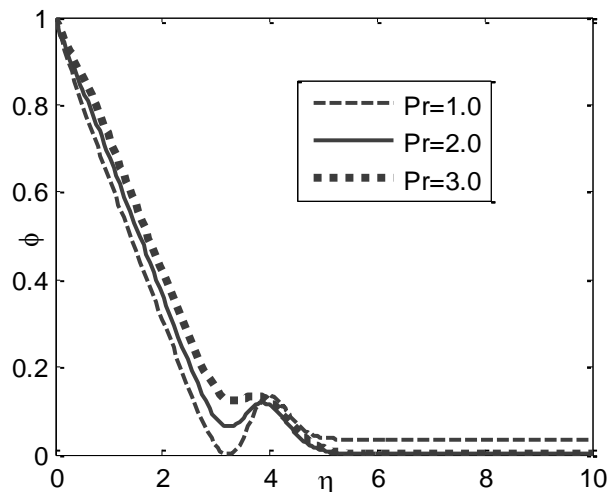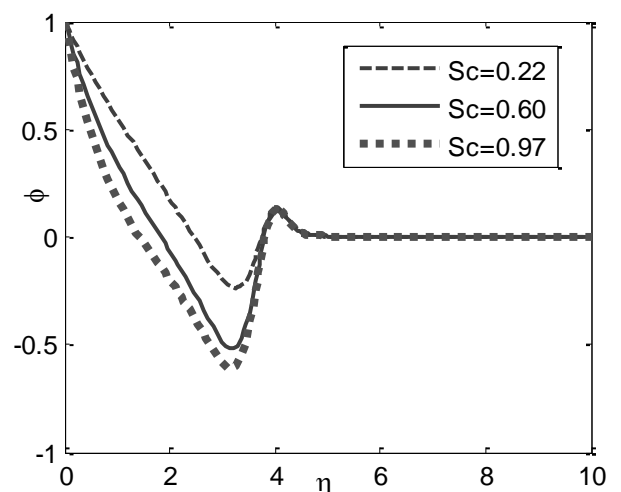

Fig.18. Concentration profile for various values of   S0

Fig.19. Concentration profile for various values of   Ec

Fig.21. Concentration profile for various values of γ

Fig.20. Concentration profile for various values of   Pr

Fig.22. Concentration profile for various values of   Sc

References

[1] Raptis, A. and C. Perdikis, Viscous flow over a non-linearly stretching sheet in the presence of a chemical reaction and magnetic field, Int. J. Nonlinear Mechanics, 41 (2006), pp. 527-529.

[2] Tan Y, You XC, Xu Hang and Liao SJ, A new branch of the temperature distribution of boundary layer flows over an impermeable stretching plate, Heat Mass Transf. 44 (2008), pp. 501-504.

[3] Abel, M. S., Mahesha, N. Heat transfer in MHD viscoelastic fluid flow over a stretching sheet with variable thermal conductivity, non-uniform heat source and radiation, App. Math. Mod, 32 (2008), pp. 1965-1983.

[4] Samad, M. A., and Mohebujjamanr, M. MHD heat and mass transfer free convection flow along a vertical stretching sheet in presence of magnetic field with heat generation, Res. J. Appl. Sci. Eng. Tech. 1 (2009), pp. 98-106.

[5] Saleh M. Alharbi1, Mohamed A. A. Bazid, Mahmoud S. El Gendy, Heat and mass transfer in MHD visco-elastic fluid flow through a porous medium over a stretching sheet with chemical reaction, App. Mathematics, 1(2010) , pp. 446-455.

[6] M. A. Seddeek and M. S. Abdelmeguid, Effects of radiation and thermal diffusivity on heat transfer over a stretching surface with variable heat flux, Physics Letters A, 348(2006), pp. 172-179.

[7] M. Ali, M. S. Alam, M. M. Alam and M. A. Alim, Radiation and thermal diffusion effects on a steady MHD free convection heat and mass transfer flow past an inclined stretching sheet with Hall current and heat generation, IOSR J. of Mathematics, 9(2014), pp. 33-45.

[8] W. Ibrahim and B. Shanker, Unsteady MHD boundary layer flow and heat transfer due to stretching sheet in the presence of heat source or sink by Quasi-linearization technique, Int. J. of Appl. Math. And Mech. 8(2012), pp. 18-30.

[9] Ishak A, Nazar R and Pop I, Boundary layer flow and heat transfer over an unsteady stretching vertical surface, Mechanica, 44 (2009), pp. 369-375.

[10] Ebashbeshy and Aldawody, Heat transfer over an unsteady stretching surface with variable heat flux in presence of heat source or sink, Computers and Mathematics with applications, 60(2010), pp. 2806-2811.

[11] Fadzilah M, Nazar R, Norihan M and Pop I, MHD boundary layer flow and heat transfer of a viscous and electrically conducting fluid over a stretching sheet with an induced magnetic field, J. of heat mass transfer,47 (2011), pp. 155-162.

[12] M.M. Rashidi, M. Keimanesh, Using differential transform method and Padé Approximant for solving MHD flow in a laminar liquid film from a horizontal stretching surface, Mathematical Problems in Engineering, 2010 (2010), 14 pages.

[13] M.M. Rashidi, E. Erfani, A New analytical study of MHD stagnation–point flow in porous media with heat transfer, Computers & Fluids, 40 (2011), pp. 172–178.

[14] M.M. Rashidi, T. Hayat, E. Erfani, S.A. Mohimanian Pour, Awatif A-Hendi, Simultaneous effects of partial slip and thermal-diffusion and diffusion-thermo on steady MHD convective flow due to a rotating disk, Communications in Nonlinear Science and Numerical Simulations 16 (2011), pp. 4303–4317.

[15] Mohebujjaman M, Khalequ S and Samad M, MHD heat transfer mixed convection flow along a vertical stretching sheet in presence of magnetic field with heat generation , Int. J. of basic and Applied Science ,10 (2010).

[16] Y. I. Seini1 and O. D. Makinde, MHD Boundary Layer Flow due to Exponential Stretching Surface with Radiation and Chemical Reaction, Hindawi Publishing Corporation Mathematical Problems in Engineering , (2013), 7 pages.

6th BSME International Conference on Thermal Engineering (ICTE 2014)

Finite Difference Solution of the Diffusion Equation and Calculation of the Interdiffusion Coefficient using the Sauer-Freise and Hall Methods in Binary Systems

Tanvir Ahmed*, Irina V. Belova and Graeme E. Murch

Centre for Mass and Thermal Transport in Engineering Materials, School of Engineering, Faculty of Engineering and Built Environment, University of Newcastle, Callaghan, University Drive, Callaghan NSW 2308, Australia

Abstract

The study of concentration dependent diffusion is important in the field of alloys and semiconductors. It is a key issue to calculate accurate interdiffusion coefficients using experimentally obtained concentration profiles. The Boltzmann-Matano (BM) method is often used for determining diffusion coefficients. But this technique has some shortcomings in calculating an accurate interdiffusion coefficient. Because of this, the Sauer and Freise (SF) method (which is a clever modification of the BM method) is more useful for calculating the interdiffusion coefficient. The Hall Method (HM) was specifically designed for determining the interdiffusion coefficient at the low and high concentration limits. In the present study, concentration profiles have been numerically generated as a solution to the interdiffusion problem in a binary system when the interdiffusion coefficient is dependent on concentration. This has been done using an explicit finite difference method. A comparative study of the HM, BM and SF methods has been performed using the generated concentration profiles. This allows for a direct comparison between the SF, BM and HM techniques. Present results clearly indicate that the HM technique can only be applicable when the interdiffusion coefficient is constant (independent of concentration) or almost constant at the low concentration regions. In all other cases the SF method gives the best agreement with the input interdiffusion function.

Keywords: Diffusion Equation; Hall method; Sauer-Freise Method; Finite Difference Method

---

* Corresponding author. Mobile.: +61469826107; fax: +61-2-4921-6946.
   E-mail address: Tanvir.Ahmed@uon.edu.au

1. Introduction

The study of concentration dependent mass diffusion is important in the field of metals and semiconductors. There is considerable demand for information on accurate diffusion coefficients, including interdiffusion coefficients. When the diffusion coefficient is dependent on concentration, it is difficult to find a closed form solution. Kass and O'Keeffe [1] studied the numerical solution of the Diffusion Equation with concentration dependent diffusion coefficients. Mittemeijer and Rozendaal [2] applied a step method for numerical solution of the Diffusion Equation and developed an iterative procedure when the diffusion coefficient is concentration dependent. They proposed that their iterative method takes less calculation time than other procedures. Garcia *et al.* [3] studied a finite difference scheme to solve the one-dimensional in space Diffusion Equation with special investigation of the stability and convergence of the scheme.

An analytical method for calculating the diffusion coefficients was originally investigated by Boltzmann [4]. This method was first used by Matano [5] to analyze experimental interdiffusion concentration profiles. Nowadays, this method is known as the Boltzmann-Matano (BM) method. However, the solutions obtained by the BM method are valid only under some preconditions. This analysis was carried out for mathematical and educational purposes. The BM method, at first, was introduced as a graphical method to find the interdiffusion coefficient. But the graphical method has some disadvantages for calculating an accurate interdiffusion coefficient. For this reason, Sauer and Freise [6] proposed a new equation for calculating the interdiffusion coefficient which is a further modification of the BM method. Using this method, it is possible to find an accurate interdiffusion coefficient as a function of concentration, avoiding the calculation of the Matano-interface location. Den Broeder [7] proposed a general simplification and improvement of the BM method for calculating interdiffusion coefficients in binary systems. Wagner [8] suggested a simplified derivation of the Sauer and Freise (SF) equation for calculation of the interdiffusion coefficient as a function of concentration. Kailasam *et al.* [9] studied the BM, SF, Wagner and den Broeder methods for calculating the concentration dependent interdiffusion coefficient in binary systems. In addition, a finite difference method was investigated by Wei *et al.* [10] for determining the interdiffusion coefficient of an aluminide coating formed on a superalloy.

Appel [11] investigated a further development of the BM method analytically for a multiphase system. Hall [12] developed an analytical method which is called a further modification of the BM method and also suggested that the resulting method, now called the Hall Method (HM), gives an accurate determination of the diffusion coefficients near the high and low concentration limits. It was slightly modified by Crank [13] using the Boltzmann variable divided by two. Finally, the HM was extended by Sarafianos [14]. Okino *et al.* [15] studied an analytical solution of the Boltzmann transformation equation with no preconditions.

Stenlund [16] studied three methods (two methods for three-dimensional and a third one for the one-dimensional case) to calculate the interdiffusion coefficient from a concentration profile without any limitations by boundary conditions. But these methods are suitable for numerical calculation only when the concentration data and the time series are available. Zhang and Zhao [17] developed a MATLAB based program to calculate the interdiffusion coefficients for binary diffusion couples using traditional methods i.e. BM method, SF method, the HM, and the Wagner method and a forward-simulation method. Recently, Belova *et al.* [18] derived a novel way of measuring interdiffusion and tracer diffusion coefficients in one experiment with an analysis based on the application of linear response theory. They showed that the Sauer and Freise method can be modified for the analysis of the combined tracer and interdiffusion experiment.

The primary aim of current study is to generate the numerical solution of the Diffusion Equation by using a finite difference method. We then investigate the analysis of the thus generated concentration profiles by means of the methods of BM, SF and Hall to find the interdiffusion coefficient.

2. Mathematical Formulation

The governing equation of the interdiffusion process in a binary alloy is described by one-dimensional in space Diffusion Equation:

$$\frac{\partial C}{\partial t} = \frac{\partial}{\partial x}\left(D\frac{\partial C}{\partial x}\right) \tag{1}$$

with the boundary conditions: $C = 1$, $x = -\infty$, $t > 0$ and $C = 0$, $x = +\infty$, $t > 0$. Here C is the concentration as a function of distance, x and time, t, D is the diffusion coefficient. D could be a constant but in general it depends on concentration. Once the concentration profile $C(x,t)$ is determined the BM method can be applied to determine the concentration dependent diffusion coefficient $D(C)$ at time, t, as:

$$D(C^*) = -\frac{1}{2t}\frac{\displaystyle\int_0^{C^*}(x - x_M)dC}{\left(\dfrac{dC}{dx}\right)_{C^*}} \tag{2}$$

where x_M is the position of the Matano plane. The location of the Matano plane is determined from the conservation condition $\displaystyle\int_{-\infty}^{x_M}(1 - C(x))dx = \int_{x_M}^{+\infty}C(x)dx$. A further development of BM method has been proposed by Eversole *et al.* [19] for dilute solutions. They evaluated the integration term by parts. Then from Eq. (2) the following expression is found:

$$D(C^*) = -\frac{1}{2t}\frac{(x^* - x_M)C^* + \displaystyle\int_{x^*}^{+\infty}Cdx}{\left(\dfrac{dC}{dx}\right)_{C^*}} \tag{3}.$$

According to the SF method the concentration dependent diffusion coefficient $D(C)$ at time, t, is given as:

$$D(C^*) = -\frac{1}{2t}\left(\frac{dx}{dC}\right)_{C^*}\left[C^*\int_{-\infty}^{x^*}(1 - C)dx + (1 - C^*)\int_{x^*}^{+\infty}Cdx\right] \tag{4}$$

In HM, the following transform is used:

$$C = erfc(u) \tag{5}$$

where (as defined at the time by Hall) $erfc(u) \equiv \frac{1}{2}(1 + erf(u))$, $u = h\lambda + k$ and $\lambda = \dfrac{x - x_M}{\sqrt{t}}$. Hall evaluated the integration term of Eq. (2) by using Eq. (5).
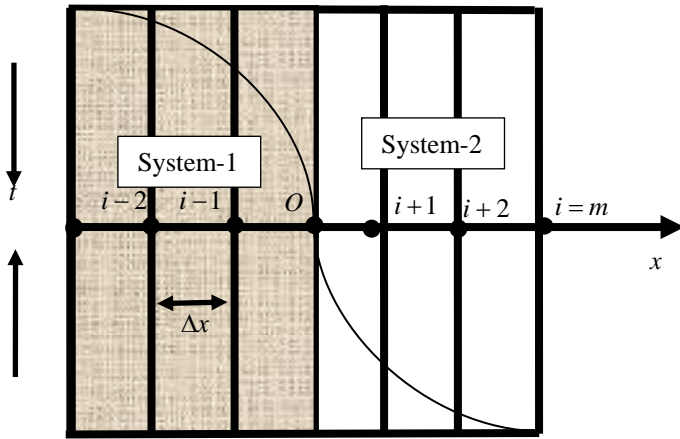
Fig. 1. Finite difference system grid for binary system.

3. Finite Difference Solution

To solve Eq. (1) we used the explicit finite difference method. In this case, the region along the space coordinate x is divided into equally spaced mesh points. It is assumed that the maximum length is $x_{\max} = (16)$ where $x_{-\infty} = -8$ and $x_{+\infty} = 8$ as corresponds to $x \to -\infty$ and $x \to -\infty$, i.e. x varies from -8 to 8 and the number of grid spacings in the x direction is $m = 200$, hence the constant mesh size along x axis becomes $\Delta x = 0.08, (-8 \le x \le 8)$ with a smaller time-step $\Delta t = 0.0001$ chosen in such a way that the stability condition is satisfied. Let C^n denote the value of C at the end of nth time-step.

Using the explicit finite difference approximation, the following finite difference equation is obtained:

$$\frac{C_i^{n+1} - C_i^n}{\Delta t} = D_i^n \frac{C_{i+1}^n - 2C_i^n + C_{i-1}^n}{(\Delta x)^2} + \left.\frac{\partial D}{\partial C}\right|_i^n \left(\frac{C_{i+1}^n - C_{i-1}^n}{2\Delta x}\right)^2 \tag{6}$$

with the boundary conditions, $C_{-\infty}^n = 1$ and $C_{+\infty}^n = 0$.

In Eq. (6) the subscript i denotes the grid points along the x coordinate and the superscript n denotes a step in time, $t = n\Delta t$ where $n = 0, 1, 2, \dots$. The concentration C at all interior mesh points is computed by successive applications of the above finite difference equations. The stability condition and convergence criterion for the finite difference solution is given by (e.g. [3,4]) $\frac{\max(D_i^n)\Delta t}{(\Delta x)^2} \le \frac{1}{2}$. In this research, we studied the following test cases:

Case-1 (constant): $D = 1$.
Case-2 (linear concentration dependence): $D = 0.5 + 0.5C$.

Case-3 (quadratic concentration dependence): $D = 1 - 2C(1 - C)$.

Case-4 (quadratic concentration dependence): $D = 2C(1 - C) + 0.5$.

In the application of the BM and SF methods, the numerical values of integration terms are calculated by the Trapezoidal Rule. But for implementation of the HM we have used Eq. (5) to get numerical values of integration terms at each space/concentration point as:
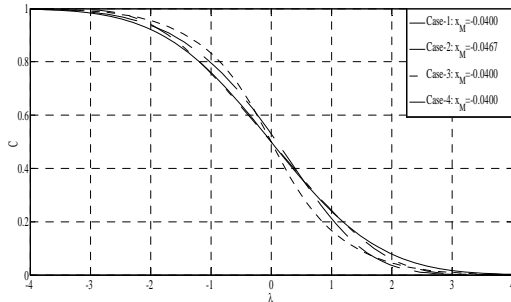
Fig. 2. Concentration profiles for different cases at time, $t = 0.40$.

$$D(i) = -\frac{1}{2}\frac{\sqrt{\pi}}{h_i'}e^{\{u'(i)\}^2}I(i+1) \quad \text{where} \quad I(1) = -\frac{1}{2h'(1)\sqrt{\pi}}e^{\{-u'(1)\}^2}$$

$$-\frac{k'(1)C'(1)}{h'(1)}, \qquad II(1) = 0, \qquad III(1) = 0, \qquad II(i) = -\frac{1}{2h'(i-1)\sqrt{\pi}}$$

$$\left[e^{\{-u(i)\}^2} - e^{\{-u'(i-1)\}^2}\right] - \frac{k'(i-1)}{h'(i-1)}(C(i) - C'(i-1)), \qquad III(i) = -\frac{1}{2h'(i)\sqrt{\pi}}\left[e^{\{-u'(i)\}^2} - e^{\{-u(i)\}^2}\right] - \frac{k'(i)}{h'(i)}(C'(i) - C(i)), \qquad I(i) = I(i-1) + II(i-1) + III(i-1),$$

$$C'(i) = 0.5(C(i)+C(i+1)), \quad u'(i) = 0.5(u(i)+u(i+1)), \quad \lambda'(i) = 0.5(\lambda(i)+\lambda(i+1)), \quad h'(i) = \frac{u(i+1)-u(i)}{\lambda(i+1)-\lambda(i)} \text{ and } k'(i) = \frac{\lambda(i+1)u(i)-\lambda(i)u(i+1)}{\lambda(i+1)-\lambda(i)}.$$

4. Results and Discussion

To obtain the finite difference solutions, the computations have been carried out for $t = 0.40$ time units. Then we calculated the interdiffusion coefficient making use of BM, SF and HM for all of the above test cases. The graphical representations of the resulting interdiffusion coefficients are given in Figs. 3-4.

In Fig. 3(a) it can be seen that both the BM method and SF method give the same results for Case-1. But the HM gives better results than the other two methods. This is particularly clear at and near the zero concentration limit, as expected. In Fig. 3(b) it can be seen that the SF method gives better results than the HM and BM method for the Case-2. At low concentrations the BM method and SF method both give the same results. But at high concentrations only the SF method gives good results. In Fig. 4(a) it can be seen that for Case-3 the BM and SF methods both give the same results. And HM gives comparable results to the other two methods. In Fig. 4(b) the same behavior of the SF and BM results for the Case-4 as for the Case-3 can be observed. But HM gives a much poorer result for this test. This trend is most obvious at and near to the low and high concentration limits.

a   b
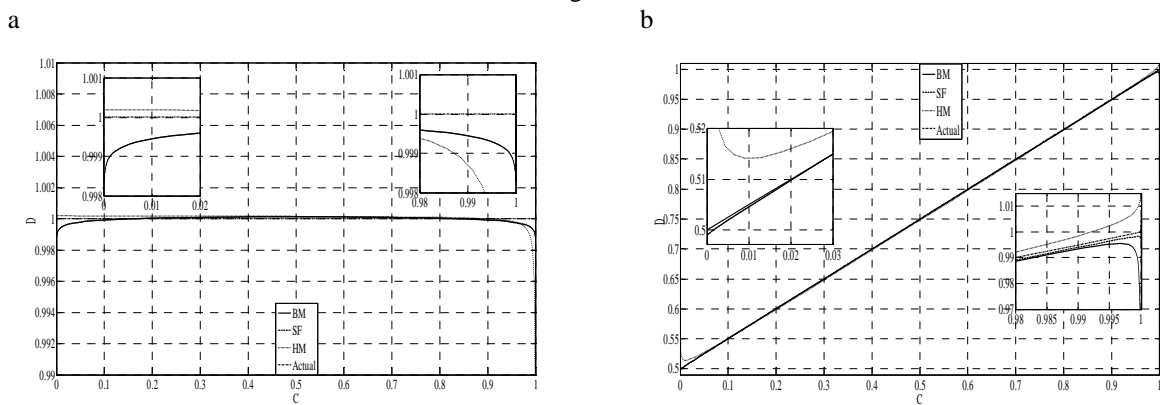
Fig. 3. Interdiffusion coefficient vs Concentration for (a) Case-1 and (b) Case-2.

a   b
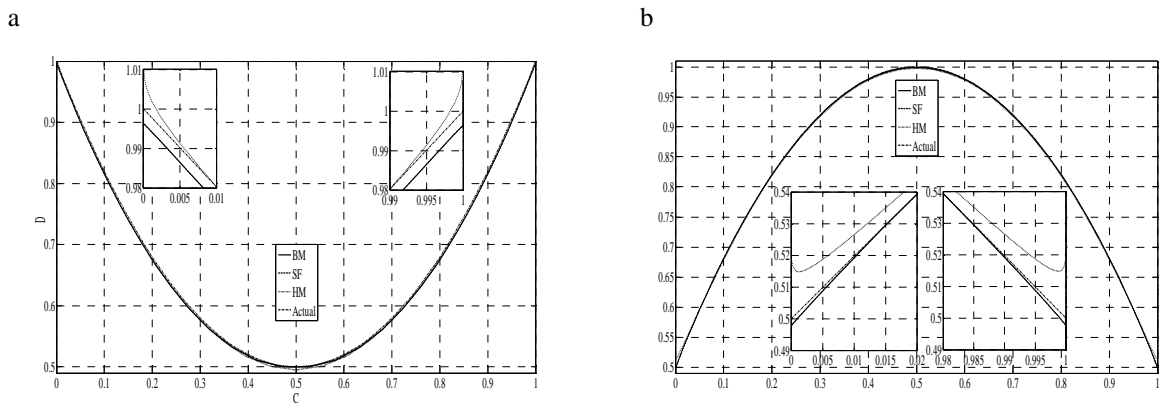
Fig. 4. Interdiffusion coefficient vs Concentration for (a) Case-3 and (b) Case-4.

5. Conclusions

In this study, the explicit finite difference solution of the Diffusion Equation for binary alloy systems with concentration dependent interdiffusion coefficients has been used to generate interdiffusion concentration profiles for several test cases. Three methods to obtain the interdiffusion coefficient as a function of concentration were investigated for those test cases. They were the Boltzmann-Matano, Sauer and Freise and Hall methods. It was

observed that the results of the SF method were generally the best compared with the results of the BM and Hall methods. Only for a constant interdiffusion coefficient did the Hall method give the best agreement with the required interdiffusion coefficient. Therefore it was concluded that for the determination of the interdiffusion coefficient at or near to the low and high concentration levels the Hall method should be applied with care.

Acknowledgements

References

[1] W. Kass, and M. O'Keeffe, Numerical Solution of Fick's Equation with Concentration-Dependent Diffusion Coefficients, Journal of Applied Physics. 37(1966) 2377-2379.
[2] E. J. Mittemeijer, and H. C. F. Rozendaal, A rapid method for numerical solution of Fick's second law where the diffusion coefficient is concentration dependent, Scripta Metallurgica. 10 (1976) 941-943.
[3] V. Garcia, P. Mors, and C. Scherer, Kinetics of phase formation in binary thin films: the Ni/Al case, Acta Materialia. 48(2000) 1201-1206.
[4] L. Boltzmann, Zur Integration der Diffusionsgleichung bei variabeln Diffusionscoefficienten," Annalen der Physik. 53(1894) 959-964.
[5] C. Matano, On the Relation between the Diffusion-Coeffcients and Concentrations of Solid Metals (The Nickel-Copper System), Japanese Journal of Physics. 8(1933) 109-113.
[6] F. Sauer, and V. Freise, Diffusion in binären Gemischen mit Volumenänderung, Z. Elektrochem. 66(1962) 353-362, 1962.
[7] F. J. A. den Broeder, A general simplification and improvement of the matano-boltzmann method in the determination of the interdiffusion coefficients in binary systems, Scripta Metallurgica. 3(1969) 321-325.
[8] C. Wagner, The evaluation of data obtained with diffusion couples of binary single-phase and multiphase systems, Acta Metallurgica. 17(1969) 99-107.
[9] S. Kailasam, J. Lacombe, and M. Glicksman, Evaluation of the methods for calculating the concentration-dependent diffusivity in binary systems, Metallurgical and Materials Transactions A. 30(1999) 2605-2610.
[10] X. S. Hua Wei, Qi Zheng, Guichen Hou, Hengrong Guan, Zhuangqi Hu, A Finite Difference Method for Determining Interdiffusivity of Aluminide Coating Formed on Superalloy, J. Mater. Sci. Technol. 20(2004) 595-598.
[11] M. Appel, Solution for Fick's 2nd law with variable diffusivity in a multi-phase system, Scripta Metallurgica. 2(1968) 217-221.
[12] L. D. Hall, An Analytical Method of Calculating Variable Diffusion Coefficients, Journal of Chemical Physics. 21(1953) 87-89.
[13] J. Crank, The Mathematics of Diffusion, Oxford University Press, London, 1979.
[14] N. Sarafianos, An analytical method of calculating variable diffusion coefficients, Journal of Materials Science. 21(1986) 2283-2288.
[15] T. Okino, T. Shimozaki, R. Fukuda, and H. Cho, Analytical Solutions of the Boltzmann Transformation Equation, Defect and Diffusion Forum. 322 (2012) 11-31.
[17] H. Stenlund, "Three Methods for Solution of Concentration Dependent Diffusion Coefficient, Tech. rep., Visilab Signal Technologies Oy; 2011.
[16] Q. Zhang, and J.C. Zhao, Extracting interdiffusion coefficients from binary diffusion couples using traditional methods and a forward-simulation method, Intermetallics. 34(2013) 132-141.
[18] I. V. Belova, N. S. Kulkarni, Y. H. Sohn, and G. E. Murch, Simultaneous measurement of tracer and interdiffusion coefficients: an isotopic phenomenological diffusion formalism for the binary alloy, Philosophical Magazine. 93(2013) 3515-3526.
[19] W. Eversole, J. D. Peterson, and H. Kindsvater, Diffusion Coefficients in Solution. An Improved Method for Calculating D as a Function of Concentration, The Journal of Physical Chemistry. 45 (1941) 1398-1403.

6th BSME International Conference on Thermal Engineering (ICTE 2014)

Numerical analysis of primary conversion efficiency of oscillating water columns with multiple chambers

Pallav Koirala*, Shuichi Nagata, Yasutaka Imai, Tengen Murakami, Toshiaki Setoguchi

Institute of Ocean Energy, Saga University, Saga Shi, 840-8502, Japan

Abstract

The authors investigate the primary conversion efficiency of Oscillating Water Columns (OWCs) with multiple water chambers and air chambers. Two-dimensional frequency-domain numerical models to estimate the primary conversion efficiency of a two-chamber OWC with two air chambers and a two chamber OWC with one air chamber are developed. The numerical results are compared with that of a conventional one chamber OWC with equivalent total chamber width and front opening. The wave induced force is calculated using the boundary element method based on the velocity potential theory. Assuming air to be an ideal gas, the air flow is calculated using an equation of state and the equations of conservation of mass and energy. Boundary integral equations are formulated to calculate the air pressure in the air chambers, the reflection coefficient and the primary conversion efficiency of each of the chambers as well as the combined efficiency. In addition, the behaviour of these physical quantities with the variation of the nozzle ratio, the relative water depth, the depth of the curtain wall and the width of the front-chamber are investigated using the calculated results.

Keywords: Boundary element; velocity potential; primary conversion efficiency; reflection coefficient.

Nomenclature

b_c width of front chamber
C_p specific heat at constant pressure

---

* Corresponding author. Tel.: +81-0952-28-8624; fax: +81-0952-28-8595
  E-mail address: koirala@ioes.saga-u.ac.jp

C_v	specific heat at constant volume
C_d	coefficient of contraction
C_s	coefficient of velocity
d_c	height of curtain wall
EFF	primary conversion efficiency
E_air	absorbed power by OWC
E_w	Incident wave power
g	acceleration due to gravity
h	water depth
H	wave height
i	imaginary unit
j	field point (centre of the element)
k	wave number
K_R	reflection coefficient
l	distance from the origin where the imaginary boundary of Region-1 is located
L	total length of OWC in the direction of wave propagation
m	number of source point
N	total number of elements
p_0	atmospheric air pressure
p_1	air pressure in chamber 1
p_2	air pressure in chamber 2
R_{mj}	distance between the source point and the field point
Q	inflow or outflow rate of air through the nozzle
SF_0	water surface in region-1
SF_1	water surface in chamber-1
SF_2	water surface in chamber-2
T	wave period
T_a	temperature of air in the air chamber
T_0	absolute temperature of atmospheric air
V_a	volume of air in air chamber
X	coordinate axis in the direction of wave propagation
W	width of chamber
w_0	specific weight of water
Γ	nondimensionalised angular frequency of the wave
ΔS_j	length of jth element
ε	nozzle area ratio
ζ	water surface elevation
λ	wave length of incident wave
μ	Rayleigh's damping coefficient
v	unit normal to a surface
ξ	component of local coordinate of the centre of the element
η	component of local coordinate of the centre of the element
ρ	mass density of water
σ	wave angular frequency
φ	velocity potential
Φ_0	incident velocity potential

1. Introduction

Oscillating water column (OWC) type wave energy converters (WECs) are popular because of their simple design and ease of installation and operation compared to other WECs [1-3]. In addition, OWCs that utilize air turbines have very few moving parts and there are no moving parts in the water. Regarding the viability of OWCs as power plants, the reliability of shore-based operations has been well demonstrated [2].

Conventional Oscillating Water Columns generally have one water chamber and one air chamber as shown in Fig.1. However, two-chamber OWCs have also been studied with the objective of increasing the output power by means of effective phase control utilizing valves [3]. More recently, Min-Fu Hsieh et al. proposed a new design with two adjacent chambers, each fitted with a turbine and a generator, aligned in the direction of wave propagation with the objective of increasing and smoothing the output power [4]. Motivated by a similar goal, the authors have numerically investigated the primary conversion efficiency of OWCs with multiple chambers: two-chamber OWC with two water chambers and two air chambers (Fig. 2) and two-chamber OWC with two water chambers and one air chamber (Fig. 3). These numerical results are compared with that of a single chamber OWC. This paper presents the results of a 2D numerical analysis in frequency domain for the OWCs using the numerical method proposed by Nagata et al. [5]. The major physical quantities examined are the primary conversion efficiency, the air pressure and the reflection coefficient. The authors intend to conduct wave tank tests in future to validate the numerical results on the multi-chamber OWCs. At present, the numerical model is validated by comparing with the experimental data of the one-chamber OWC by Ojima et al. [6, 7].
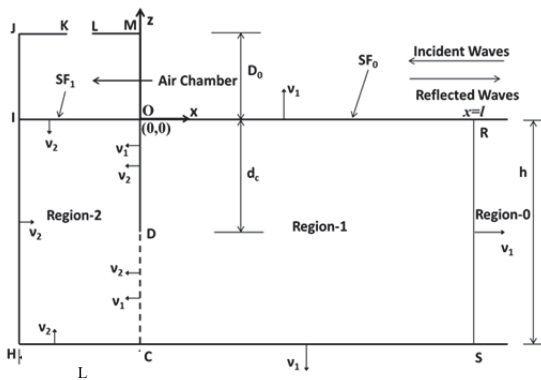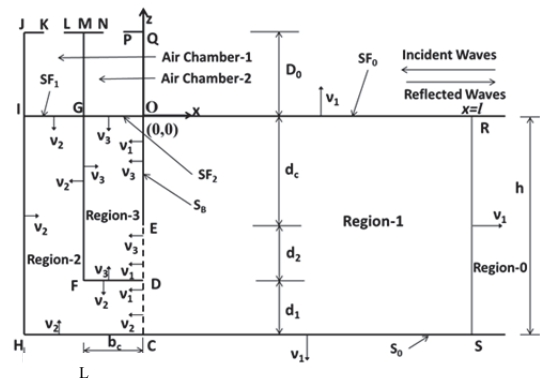

Fig.1. Sketch of one chamber OWC

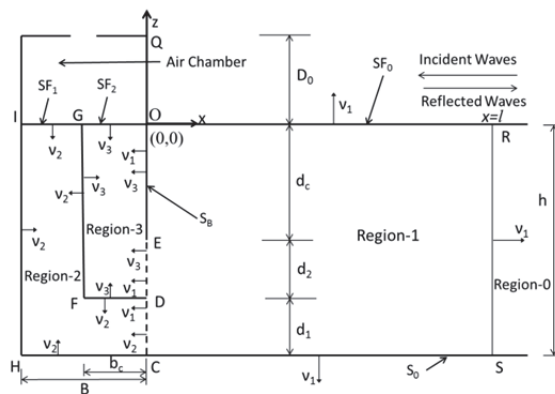Fig.2. Sketch of two chamber OWC with two air chambers

Fig.3. Sketch of two chamber OWC with one air chamber

2. Numerical model

The numerical model for the two-chamber OWC with two air chambers (Fig.2) is presented. This can be modified without much difficulty to apply to the two-chamber OWC with one air chamber (Fig.3) or one-chamber OWC (Fig.1).

2.1. Equations related to wave motion

Assuming the fluid motion to be inviscid, incompressible and of small amplitude, the potential theory gives the linearized governing equations for the velocity potential $\Phi(x, z; t)$ as follows:

$$\nabla^2 \Phi = 0 \qquad\qquad \text{in the fluid} \tag{1}$$

$$\frac{\partial \zeta}{\partial t} = \frac{\partial \Phi}{\partial z} \qquad\qquad \text{on } S_{F0}, S_{F1}, S_{F2} \tag{2}$$

$$\frac{\partial \Phi}{\partial t} + \mu\Phi + g\zeta = -\frac{1}{\rho}(p_0 + p_1) \quad \text{on } S_{F1} \tag{3}$$

$$\frac{\partial \Phi}{\partial t} + \mu\Phi + g\zeta = -\frac{1}{\rho}(p_0 + p_2) \quad \text{on } S_{F2} \tag{4}$$

$$\frac{\partial \Phi}{\partial t} + g\zeta = -\frac{p_0}{\rho} \qquad\qquad \text{on } S_{F0} \tag{5}$$

$$\frac{\partial \Phi}{\partial \nu} = 0 \qquad\qquad \text{on } S_0, S_B \tag{6}$$

Combining Eqs.(2), (3) and (5) and Eqs.(2), (4) and (5), following equations are obtained

$$\frac{\partial^2 \Phi}{\partial t^2} + g\frac{\partial \Phi}{\partial z} = 0 \qquad\qquad \text{on } S_{F0} \tag{7}$$

$$\frac{\partial^2 \Phi}{\partial t^2} + \mu\frac{\partial \Phi}{\partial z} + g\frac{\partial \Phi}{\partial z} = -\frac{1}{\rho}\frac{\partial p_1}{\partial t} \quad \text{on } S_{F1} \tag{8}$$

$$\frac{\partial^2 \Phi}{\partial t^2} + \mu\frac{\partial \Phi}{\partial z} + g\frac{\partial \Phi}{\partial z} = -\frac{1}{\rho}\frac{\partial p_2}{\partial t} \quad \text{on } S_{F2} \tag{9}$$

The fluid region is divided into four: region-0, region-1, region-2 and region-3 as shown in Fig. 2. Region-0 is the outer region of the OWC where the water depth is *h*. Regions 2 and 3 correspond to the fluid region in chambers 1 and 2 of the OWC respectively. The velocity potential $\Phi(x, z; t)$ in region-0 is obtained as the solution of Laplace's equation which satisfies the free surface and the bottom boundary conditions at constant water depth as follows

$$\Phi_0(x,z;t) = \frac{g\zeta_0}{\sigma}\left[e^{ikx} + K_R e^{-ikx}\right]\frac{\cosh k(z+h)}{\cosh kh}e^{-i\sigma t} \tag{10}$$

where the first term inside the brackets on the right-hand side corresponds to the incident wave and the second term has the complex constant K_R representing the reflected wave. k is obtained by solving the following dispersion relation

$$\sigma^2 = gk\tanh kh \tag{11}$$

Φ, p_1 and p_2 and the coordinate system are non-dimensionalized as follows

$$\Phi(x,z;t) = \frac{g\zeta_0}{\sigma}\mathrm{Re}\left[\phi(x,z)e^{i\sigma t}\right] \tag{12}$$

$$p_1(t) = \rho g\zeta_0\,\mathrm{Re}\left(p_1^a e^{i\sigma t}\right) \tag{13}$$

$$p_2(t) = \rho g\zeta_0\,\mathrm{Re}\left(p_2^a e^{i\sigma t}\right) \tag{14}$$

$$\zeta(x;t) = \zeta_0\mathrm{Re}\left(\zeta^a e^{i\sigma t}\right) \tag{15}$$

$$x' = \frac{x}{h}, z' = \frac{z}{h} \tag{16}$$

These dimensionless terms are used hereafter without the primes.

2.2. The boundary value problem

The boundary value problems for the potential functions $\phi^{(1)}$ in region-1, $\phi^{(2)}$ in region-2 and $\phi^{(3)}$ in region-3 can be written as

- Region-1

$$\nabla^2\phi^{(1)} = 0 \qquad\qquad \text{in the fluid} \tag{17}$$

$$\frac{\partial\phi^{(1)}}{\partial\nu} = \Gamma\phi^{(1)} \qquad\qquad \text{on } \mathrm{S_{F0}} \tag{18}$$

$$\frac{\partial\phi^{(1)}}{\partial\nu} = 0 \qquad\qquad \text{on } \mathrm{S_0}, \mathrm{S_B} \tag{19}$$

$$\phi^{(1)}(l,z) = \left(e^{-i\lambda l} + K_R e^{i\lambda l}\right)A(\lambda z) \qquad \text{on RS} \tag{20}$$

$$\frac{\partial\phi^{(1)}}{\partial\nu}(l,z) = -i\lambda\left[e^{-i\lambda l} - K_R e^{i\lambda l}\right]A(\lambda z) \qquad \text{on RS} \tag{21}$$

where

$$
\left.\begin{array}{l}
A(\lambda z) = \dfrac{\cosh \lambda(z+1)}{\cosh \lambda} \\[2ex]
\Gamma = \dfrac{\sigma^2 h}{g} \\[2ex]
\lambda = kh
\end{array}\right\}
\tag{22}
$$

- Region-2

$$
\nabla^2 \phi^{(2)} = 0 \qquad\qquad\qquad \text{in the fluid} \tag{23}
$$

$$
\frac{\partial \phi^{(2)}}{\partial \upsilon} = \Gamma\left[i p_1^a - \left(1 - i\frac{\mu}{\sigma}\right)\phi^{(2)} \right] \qquad \text{on } S_{F1} \tag{24}
$$

$$
\frac{\partial \phi^{(2)}}{\partial \nu} = 0 \qquad\qquad\qquad \text{on } S_B \tag{25}
$$

- Region-3

$$
\nabla^2 \phi^{(3)} = 0 \qquad\qquad\qquad \text{in the fluid} \tag{26}
$$

$$
\frac{\partial \phi^{(3)}}{\partial \upsilon} = \Gamma\left[i p_2^a - \left(1 - i\frac{\mu}{\sigma}\right)\phi^{(3)} \right] \qquad \text{on } S_{F2} \tag{27}
$$

$$
\frac{\partial \phi^{(3)}}{\partial \nu} = 0 \qquad\qquad\qquad \text{on } S_B \tag{28}
$$

- Kinematical conditions on boundary DC

$$
\phi^{(1)} = \phi^{(2)} \tag{29}
$$

$$
\frac{\partial \phi^{(1)}}{\partial \nu} = \frac{\partial \phi^{(2)}}{\partial \nu} \tag{30}
$$

- Kinematical conditions on boundary ED

$$
\phi^{(1)} = \phi^{(3)} \tag{31}
$$

$$
\frac{\partial \phi^{(1)}}{\partial \nu} = \frac{\partial \phi^{(3)}}{\partial \nu} \tag{32}
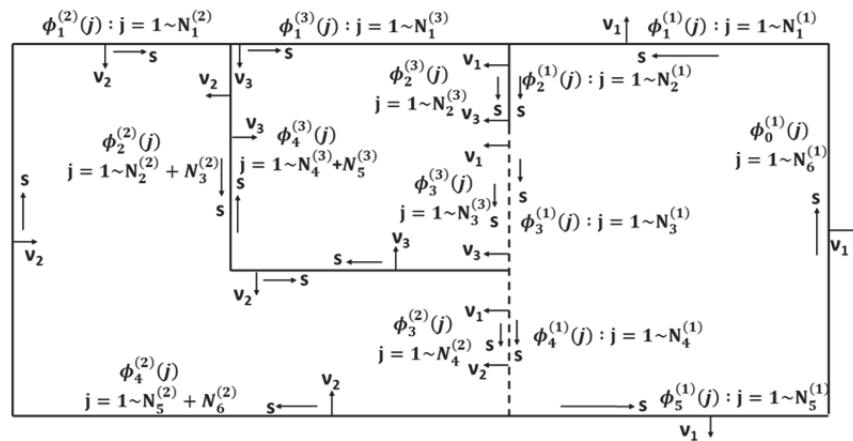$$

2.3. Boundary integral equations

Fig.4. Definition of potential function on boundaries

The boundary enclosing the fluid region is divided into N elements by N points. If we denote the center and the length of each element by $j=(\xi_j,\eta_j)$ and ΔS_j $(j=1\sim N)$ respectively, the relationships between the potentials on the boundary $\phi(j)(=\phi(\xi_j,\eta_j))$ and their normal derivatives $\bar{\phi}(j)(=\bar{\phi}(\zeta_j,\eta_j))$ are given by Green's theorem as

$$\sum_{j=1}^{N}\left[F_{mj}\phi(j)-E_{mj}\bar{\phi}(j)\right]=0 \tag{33}$$

where

$$F_{mj}=-\delta_{mj}+\overline{E}_{mj} \qquad\qquad \text{for region 1}$$

$$F_{mj}=\delta_{mj}+\overline{E}_{mj} \qquad\qquad \text{for regions 2, 3}$$

$$E_{mj}=\frac{1}{\pi}\int_{\Delta s_j}\log R_{mj}ds$$

$$\overline{E}_{mj}=\frac{1}{\pi}\int_{\Delta s_j}\frac{\partial}{\partial v}\log R_{mj}ds$$

$$R_{mj}=\left[\left(\xi_j-\xi_m\right)^2+\left(\eta_j-\eta_m\right)^2\right]^{\frac{1}{2}}$$

The potential functions on the boundary lines RO, OE, ED, DC, CS and SA of region-1(Fig.2) are denoted by $\phi_1^{(1)},\phi_2^{(1)},\phi_3^{(1)},\phi_4^{(1)},\phi_5^{(1)}$ and $\phi_0^{(1)}$ respectively. These boundary lines are divided by $N_1^{(1)},N_2^{(1)},N_3^{(1)},N_4^{(1)},N_5^{(1)}$ and $N_6^{(1)}$ points respectively. In region-2 the potential functions on IG, GD, DC and CI are $\phi_1^{(2)}$, $\phi_2^{(2)}$, $\phi_3^{(2)}$ and $\phi_4^{(2)}$ respectively. These boundary lines are divided by $N_1^{(2)}$, $N_2^{(2)}+N_3^{(2)}$, $N_4^{(2)}$ and $N_5^{(2)}+N_6^{(2)}$ points respectively. On boundary lines GO, OE, ED and DG in region-3 the potentials are denoted by $\phi_1^{(3)}$, $\phi_2^{(3)}$, $\phi_3^{(3)}$ and

$\phi_4^{(3)}$ respectively.These boundary lines are divided by $N_1^{(3)}$, $N_2^{(3)}$, $N_3^{(3)}$ and $N_4^{(3)} + N_5^{(3)}$ points respectively. Using constant elements, the following can be obtained from Greens' identity

- Region-1

$$
\sum_{j=1}^{N_1^{(1)}} \left[F_{mj}^{(1)} - \Gamma E_{mj}^{(1)} \right] \phi_1^{(1)}(j) + \sum_{j=1}^{N_2^{(1)}} \left[F_{mj}^{(1)} \phi_2^{(1)}(j) \right] + \sum_{j=1}^{N_3^{(1)}} \left[F_{mj}^{(1)} \phi_3^{(1)}(j) - E_{mj}^{(1)} \overline{\phi}_3^{(1)}(j) \right]
$$

$$
+ \sum_{j=1}^{N_4^{(1)}} \left[F_{mj}^{(1)} \phi_4^{(1)}(j) - E_{mj}^{(1)} \overline{\phi}_4^{(1)}(j) \right] + \sum_{j=1}^{N_5^{(1)}} F_{mj}^{(1)} \phi_5^{(1)}(j) + K_R \sum_{j=1}^{N_6^{(1)}} \left[F_{mj}^{(1)} + i\lambda E_{mj}^{(1)} \right] e^{i\lambda l} A(kz_j) \tag{34}
$$

$$
= -\sum_{j=1}^{N_6^{(1)}} \left[F_{mj}^{(1)} - i\lambda E_{mj}^{(1)} \right] e^{-i\lambda l} A(kz_j)
$$

The number of source point m on the boundary SR is one. Hence the total number of source points m in Eq.(34) is ($N_1^{(1)} + N_2^{(1)} + N_3^{(1)} + N_4^{(1)} + N_5^{(1)} + 1$).

- Region-2

$$
\sum_{j=1}^{N_1^{(2)}} \left[F_{mj}^{(2)} + \Gamma E_{mj}^{(2)} \left(1 - i \frac{\mu}{\sigma} \right) \right] \phi_1^{(2)}(j) + \sum_{j=1}^{N_2^{(2)}+N_3^{(2)}} \left[F_{mj}^{(2)} \phi_2^{(2)}(j) \right]
$$

$$
+ \sum_{j=1}^{N_4^{(2)}} \left[F_{mj}^{(2)} \phi_3^{(2)}(j) - E_{mj}^{(2)} \overline{\phi}_3^{(2)}(j) \right] + \sum_{j=1}^{N_5^{(2)}+N_6^{(2)}} \left[F_{mj}^{(2)} \phi_4^{(2)}(j) \right] - i\Gamma \left\{ \sum_{j=1}^{N_1^{(2)}} \left[E_{mj}^{(2)} \right] \right\} p_1^a = 0 \tag{35}
$$

The total number of source points m in Eq.(35) is ($N_1^{(2)} + N_2^{(2)} + N_3^{(2)} + N_4^{(2)} + N_5^{(2)} + N_6^{(2)}$).

- Region-3

$$
\sum_{j=1}^{N_1^{(3)}} \left[F_{mj}^{(3)} + \Gamma E_{mj}^{(3)} \left(1 - i \frac{\mu}{\sigma} \right) \right] \phi_1^{(3)}(j) + \sum_{j=1}^{N_2^{(3)}} \left[F_{mj}^{(3)} \phi_2^{(3)}(j) \right]
$$

$$
+ \sum_{j=1}^{N_3^{(3)}} \left[F_{mj}^{(3)} \phi_3^{(3)}(j) - E_{mj}^{(3)} \overline{\phi}_3^{(3)}(j) \right] + \sum_{j=1}^{N_4^{(3)}+N_5^{(3)}} \left[F_{mj}^{(3)} \phi_4^{(3)}(j) \right] - i\Gamma \left\{ \sum_{j=1}^{N_1^{(3)}} \left[E_{mj}^{(3)} \right] \right\} p_2^a = 0 \tag{36}
$$

The total number of source points m in Eq.(36) is ($N_1^{(3)} + N_2^{(3)} + N_3^{(3)} + N_4^{(3)} + N_5^{(3)}$).

2.4. Thermodynamics of the air chamber

The equations presented in this section are applicable to both chambers. Therefore, subscripts 1 and 2 denoting the respective chambers are dropped here and will be reintroduced later. Assuming air to be a perfect gas, the equation of state, the equation of the continuity and the equation of conservation of energy are given as follows [7].

$$
\frac{p_a}{\rho_a} = RT_a \tag{37}
$$

$$\frac{d}{dt}(\rho_a V_a) + \frac{dm_a}{dt} = 0 \tag{38}$$

$$p_a \frac{dV_a}{dt} + C_v \frac{d}{dt}\left(\frac{p_a V_a}{R}\right) + C_p T_e \frac{dm_a}{dt} = 0 \tag{39}$$

$$\frac{dm_a}{dt} = \pm \rho_e \varepsilon C_d C_S A_W \sqrt{2C_P|T_a - T_0|} \tag{40}$$

In this paper, Nakagawa and Ueki method [8] is followed in which the pressure and the average water surface elevation in the air chamber is given based on Eqs.(37)~(40) and by linearizing the nonlinear term in Eq. (40). We consider the case of outflow first. The following equation is obtained by using Eq.(37) in Eq. (38).

$$\frac{d}{dt}\left(\frac{p_a V_a}{RT_a}\right) + \frac{dm_a}{dt} = 0 \tag{41}$$

Eliminating dm_a/dt in Eq.(39), Eq.(41) leads to

$$\frac{1}{T_a}\left(\frac{dT_a}{dt}\right) = \frac{R}{C_p}\frac{1}{p_a}\frac{dp_a}{dt} \tag{42}$$

Eq.(43) is obtained from Eq.(37),(39) and (40).

$$\frac{C_p}{V_a}\frac{dV_a}{dt} + \frac{C_v}{p_a}\frac{dp_a}{dt} + C_p \varepsilon C_d C_S A_W \frac{1}{V_a}\sqrt{2C_p|T_a - T_0|} = 0 \tag{43}$$

We assume the magnitude of the variations in p_a, V_a and T_a are small enough so that they can be written as

$$\left.\begin{aligned}
p_a(t) &= p_0 + p_s(t) = p_0 + \text{Re}\left[\hat{p}_s^a e^{i\sigma t}\right] \\
V_a(t) &= V_0 + \text{Re}\left[\hat{v} e^{i\sigma t}\right] \\
T_a(t) &= T_0 + \text{Re}\left[\hat{T}_s e^{i\sigma t}\right]
\end{aligned}\right\} \tag{44}$$

Substituting Eq.(44) into Eq.(42) and Eq.(43) and comparing the coefficient of $e^{i\sigma t}$ we obtain

$$\left(1 - \frac{1}{\gamma}\right)\left(\frac{\hat{p}_s^a}{p_0}\right) - \frac{\hat{T}}{T_0} = 0 \tag{45}$$

$$\begin{aligned}
&\text{Re}\left[i\sigma\left(\frac{\hat{v}}{V_0}\right)e^{i\sigma t}\right] + \frac{1}{\gamma}\text{Re}\left[i\sigma\left(\frac{\hat{p}_s^a}{p_0}\right)e^{i\sigma t}\right] \\
&+ \frac{\varepsilon C_d C_S A_W \sqrt{2C_p T_0}}{V_0}\sqrt{\left|\text{Re}\left\{\left(\frac{\hat{T}}{T_0}\right)e^{i\sigma t}\right\}\right|} = 0
\end{aligned} \tag{46}$$

The nonlinear term in Eq.(46) is linearized as follows

Author name / Procedia Engineering 00 (2015) 000–000

$$\sqrt{\left|\mathrm{Re}\left\{\left(\frac{\hat{T}}{T_0}\right)e^{i\sigma t}\right\}\right|} = \alpha\,\mathrm{Re}\left\{\left(\frac{\hat{T}}{T_0}\right)e^{i\sigma t}\right\} \qquad (47)$$

where

$$\alpha = \frac{2}{\pi}\left|\frac{\hat{T}}{T_0}\right|^{-\frac{1}{2}} \int_{-\pi/2}^{\pi/2} \cos\chi\sqrt{\cos\chi}\,d\chi \qquad (48)$$

We get the following equation by substituting Eq.(47) into Eq.(46)

$$i\sigma\left(\frac{\hat{v}}{V_0}\right) + \frac{i\sigma}{\gamma}\left(\frac{\hat{p}_s^a}{p_0}\right) + \beta\left(\frac{\hat{T}}{T_0}\right) = 0 \qquad (49)$$

where

$$\left.\begin{array}{l} \beta = \dfrac{\beta_0}{\sqrt{\left(\hat{T}/T_0\right)}} \\[2ex] \beta_0 = \dfrac{\varepsilon C_d C_s A_W \sqrt{2C_p T_0}}{V_0}\alpha_0 \\[2ex] \alpha_0 = \dfrac{2}{\pi}\displaystyle\int_{-\pi/2}^{\pi/2}\cos\chi\sqrt{\cos\chi}\,d\chi \end{array}\right\} \qquad (50)$$

From Eq. (45) and Eq.(49) we obtain

$$\frac{\hat{p}_s^a}{p_0} = \frac{-i\sigma\gamma}{i\sigma + \beta(\gamma-1)}\frac{\hat{v}}{V_0} \qquad (51)$$

Eq.(51) is valid for the case of inflow as well. The volume of air in the air chamber is expressed as

$$V_a = V_0 - \iint_{S_W} \zeta\,dxdy \qquad (52)$$

Substuting Eq.(15) in Eq.(52) and comparing with the second equation of Eq.(44) we obtain

$$\hat{v} = -\iint_{S_W} \zeta_0 \zeta^a\,dxdy \qquad (53)$$

From Eq.(51), (53) and, $\hat{p}_s^a = \rho g \zeta_0 p_s^a$ we obtain

$$p_s^a = iC_E \int_{l_W} \zeta^a\,dx/l_c \qquad (54)$$

where

$$C_E = \frac{p_0}{\rho g h} \frac{1}{D_0} \frac{\sigma \gamma}{i\sigma + \beta(\gamma - 1)} \tag{55}$$

Equations (3) and (4) can be used to express the complex amplitude of the free water surface as

$$\zeta^a = -\left[i\left(1 - i\frac{\mu}{\sigma}\right)\phi + p_s^a \right] \tag{56}$$

Finally, substituting Eq.(56) in Eq.(54) and discretizing we obtain the following for chambers 1 and 2 respectively where the corresponding subscripts have been reintroduced.

$$p_{s1}^a = \frac{C_{E1}}{(1 + iC_{E1})l_{c1}} \sum_{j=1}^{N_1^{(2)}} \left(1 - i\frac{\mu}{\sigma}\right)\phi_1^{(2)}(j)\Delta x_j \tag{57}$$

$$p_{s2}^a = \frac{C_{E2}}{(1 + iC_{E2})l_{c2}} \sum_{j=1}^{N_1^{(3)}} \left(1 - i\frac{\mu}{\sigma}\right)\phi_1^{(3)}(j)\Delta x_j \tag{58}$$

2.5. Primary conversion efficiency

The primary conversion efficiency is the ratio of the absorbed power by the OWC which is the power of the air outflow or inflow through the nozzle of the air chamber to the incident wave power. The equations presented in this section are applicable to both chambers of the two-chamber OWC and therefore subscripts 1 and 2 denoting chamber 1 and chamber 2 are dropped. The total efficiency of the system is obtained by adding the individual contributions of the respective chambers. The wave power of the incident wave is expressed as

$$E_W = \frac{\rho g^2 \zeta_0^2 W}{4\sigma f(kh)} \tag{59}$$

where

$$f(kh) = \frac{2\cosh^2 kh}{2kh + \sinh 2kh} \tag{60}$$

The absorbed power by OWC can be written as

$$E_{air} = \overline{p_a(t).Q(t)} \tag{61}$$

where the overhead bar denotes time average over a period. *Q(t)* can be written as

$$Q(t) = \pm\varepsilon C_d C_s A_W \sqrt{2C_P\left|T_a - T_0\right|} = \varepsilon\alpha C_d C_s A_W \sqrt{2C_P T_0} \, \mathrm{Re}\left[\left(\frac{\hat{T}}{T_0} e^{i\sigma t}\right)\right] \tag{62}$$

Finally, E_{air} can be written as

$$E_{air} = \frac{1}{2}\rho^2 g^2 \zeta_0^2 \beta_1 \, \mathrm{Re}\left[p_s^a p_s^{a*}\right] \tag{63}$$

where

$$\beta_1 = \varepsilon \alpha C_d C_S A_W \sqrt{2 C_p T_0} \left(1 - \frac{1}{\gamma}\right) \frac{1}{p_0} \qquad (64)$$

The primary conversion efficiency can now be written as

$$EFF = \frac{E_{air}}{E_W} \qquad (65)$$

3. Validation of numerical model

As the authors are yet to conduct experiments on multi-chamber OWCs, the validation of the proposed numerical model was conducted by comparing the numerical results for one-chamber OWC with the experimental results of Ojima et al.[8]. The water depth was 0.60m, the length of OWC was 0.40m and the height of the air chamber was 0.40m. Fig.5 shows that for a given wave period, EFF increases with nozzle ratio, reaches a peak value
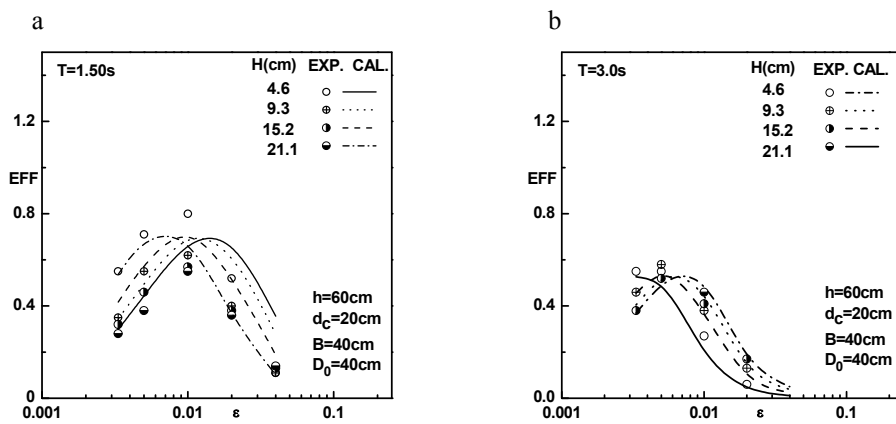

Fig. 5. Primary conversion efficiency vs nozzle ratio. (a) T=1.50s; (b) T=3.0s
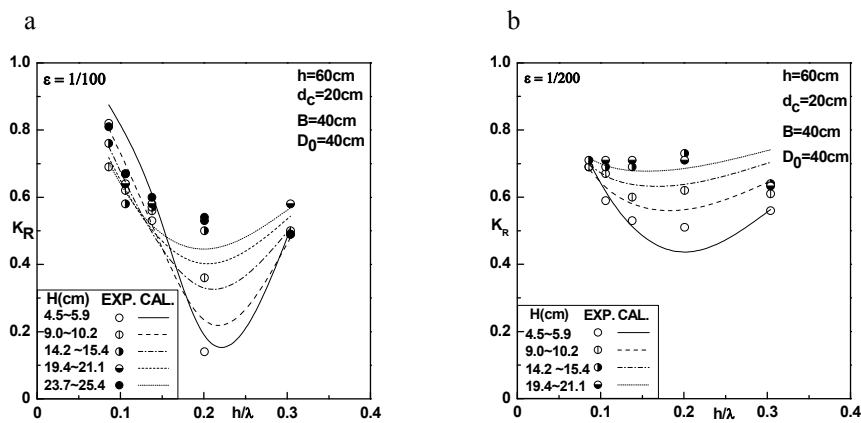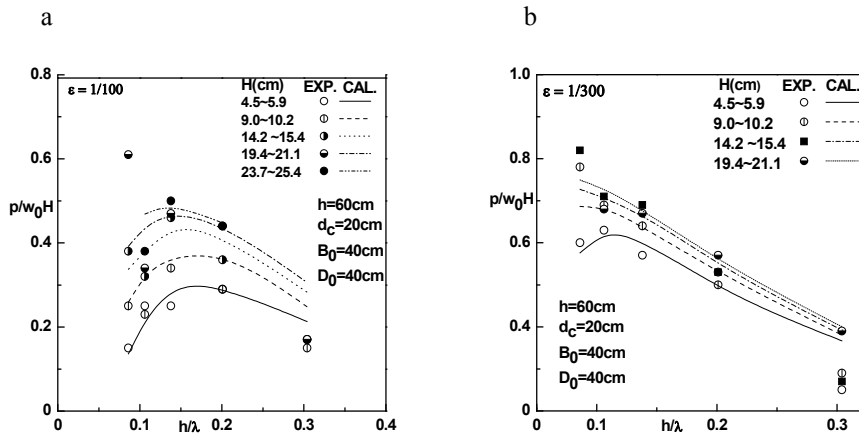

Fig. 6. K_R vs h/λ. (a) ε=1/100; (b) ε=1/200

a   b

Fig. 7. p/w$_0$H vs h/λ. (a) ε=1/100; (b) ε=1/300

and decreases again. Fig. 6 shows that for a given nozzle ratio, K$_R$ decreases with the relative depth, reaches a minimum and then increases again with a further increase of the relative depth. As for the air pressure shown in Fig. 7, it increases with the relative depth first, reaches a maximum value and decreases again with a further increase of the relative depth. It is found from Figs.5~7 that the numerical results are in good agreement with the experiment results for EFF, K$_R$ and p/w$_0$H. Hence, the numerical model can also simulate the physical phenomena for the two-chamber OWCs.

4. Numerical results

4.1. Primary conversion efficiency, air pressure and reflection coefficient of two-chamber OWC with two air chambers

Each of the chambers of the two-chamber OWC contributes to the overall efficiency of the OWC. The total efficiency is estimated as the sum total of these contributions from the individual chambers. The combined efficiency is between 60 to 90 percent and is larger for short wave periods as shown in Figs. 8(a)~(d). Also, the contribution of chamber 2 is much greater than that of chamber 1 for shorter wave periods and decreases with the increase of the period. For T=1.15s and 1.5s, EFF is highest for nozzle ratio slightly greater than 1/100. For T=2.00s it is greatest at ε=1/100 and for longer wave periods it is highest at smaller values of the nozzle ratio.
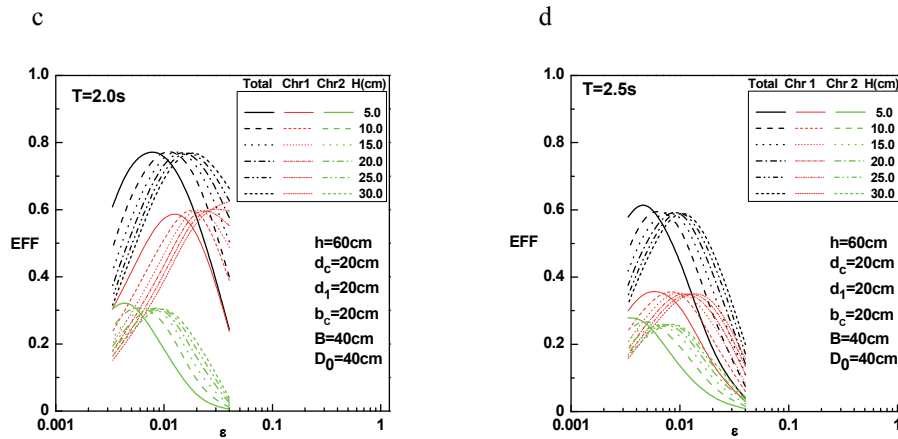
a   b

c   d
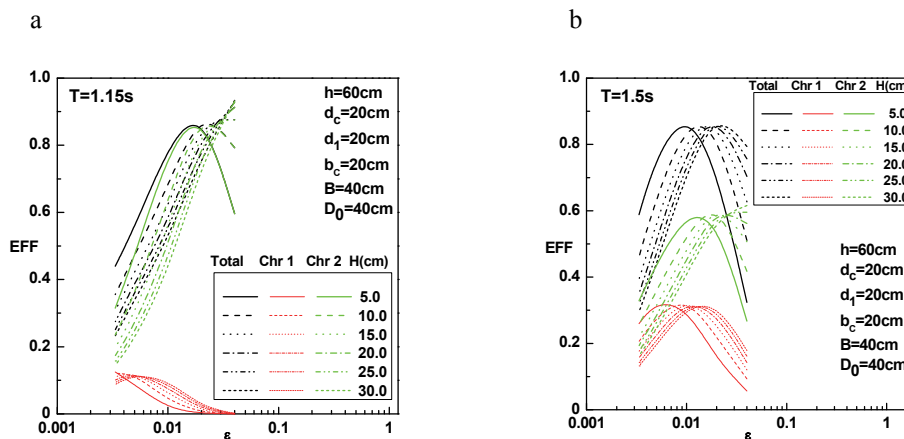
Fig. 8. Primary conversion efficiency vs nozzle ratio. (a) T=1.15s; (b) T=1.5s; (c) T=2.0s; (d) T= 2.5s

4.2. Comparison between one-chamber OWC, two-chamber OWC with two air chambers and two-chamber OWC with one air chamber
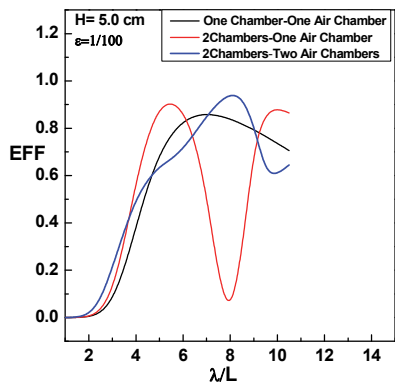

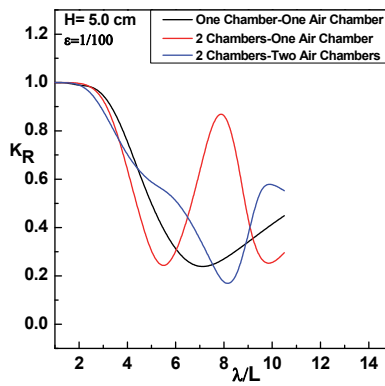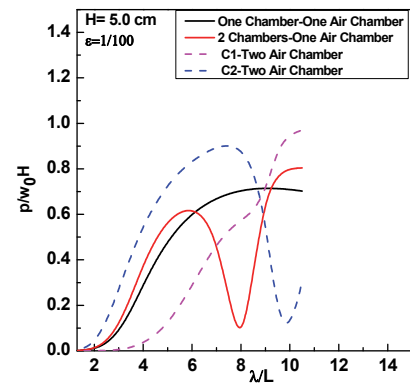Fig. 9. Primary conversion efficiency vs λ/L   Fig. 10. Reflection coefficient vs λ/L   Fig.11. Air pressure in the air chamber vs λ/L

The primary conversion efficiency increases with λ/L, reaches a maximum and decreases again for the one chamber OWC and two-chamber OWC with two air chambers as shown in Fig. 9. However, for the OWC with two chambers and one air chamber, EFF shows two peaks attaining a lowest value at λ/L=8. The reflection coefficient shows a similar trend where the two-chamber OWC with one air chamber has double troughs as shown by Fig. 10. This result is consistent with the result for EFF. The variation of air pressure in the air chamber as plotted in Fig. 11 also shows two peaks and a trough for the OWC with two chambers and a single air chamber. The peak pressure for this OWC is greater than that for the one-chamber OWC for larger values of λ/L. In Fig.11, C1 and C2 represent the back chamber and the front chamber respectively.

4.3. Effect of curtain wall depth and front chamber width in two-chamber OWC

In this section, the effects of the variation of the nondimensionalized curtain wall depth, d_c/h, and the front chamber width, b_c/h , on EFF are investigated for H=10.0cm and ε=1/100. Fig.12 shows that the primary conversion efficiency of chamber 1 is independent of d_c/h for all the wave periods. In the case of chamber 2, for T=1.15s and 1.50s, the primary conversion efficiency decreases with d_c/h. This effect is more pronounced for T=1.15s. However, for longer wave periods there is slight increase with d_c/h.
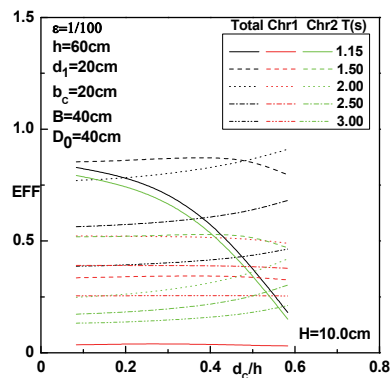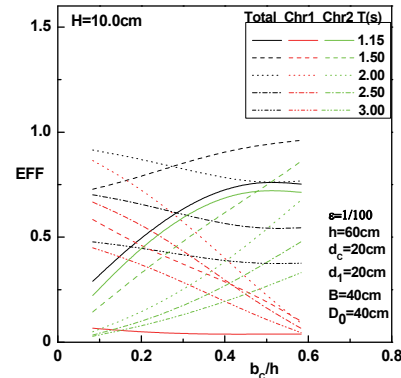
Fig. 12. Primary Conversion efficiency vs d_c/h Fig. 13. Primary Conversion efficiency vs b_c/h

Fig. 13 shows that for T=1.15 s and 1.5s, EFF increases with the increase of b_c/h. For these shorter wave periods, chamber 2 is more significant than chamber 1. For longer wave periods EFF decreases slightly with b_c/h.

5. Conclusions

The authors have investigated a two-chamber OWC with two air chambers and a two-chamber OWC with one air chamber using a two-dimensional numerical method based on velocity potential theory in frequency domain. Calculations were made on three physical quantities: primary conversion efficiency, air pressure and the reflection coefficient. Comparing with a one-chamber OWC with the same physical dimensions, it was found that EFF for the two-chamber OWC with two air chambers is slightly greater for longer wave periods. It is also observed that chamber 2 is more effective for shorter wave periods. As for the nozzle area ratio, the value of ε for which EFF is highest lies in the vicinity of 1/100 and the exact values differ different depending on the incident period. Regarding two-chamber OWC with one air chamber, EFF showed two peaks when plotted against λ/L. Though the peak values are almost equal to the double chamber OWC with two air chambers, EFF is very small around $\lambda/L=8$. Next, the effect of system parameters d_c/h and b_c/h on EFF was studied. It was found that there was no significant change in the value of EFF of chamber 1 with the increase of d_c/h. In the case of chamber 2, EFF decreased with the increase of d_c/h for $T=1.15$s and 1.5s and increased for other wave periods. The total EFF also showed a similar behaviour. For the case of b_c/h, the total EFF increased with its increasing value for $T=1.15$s and 1.5s and decreased for other periods. As expected, EFF for chamber-1 decreased rapidly with b_c/h and vice versa for chamber 2.

References

[1] J. Cruz, Ocean Wave Energy, Springer, 2008.
[2] T.V. Heath, A review of Oscillating Water Columns, Philosophical Transactions of the Royal Society A., 370, 2012, pp.235–245.
[3] J. Falnes, G. Oltedal, K. Budal, P.M. Lillebekken, Simulation Studies of a Double Oscillating Water Column, International Workshop on Water Waves and Floating Bodies, 1989, pp. 65-68.
[4] Min-Fu Hsieh, I-Hsien Lin, D.G. Dorell, Min-June Hsieh, Development of a Wave Energy Converter Using a Two Chamber Oscillating Water Column, The IEEE Transactions on Sustainable Energy, Vol. 3, Issue 3, 2012, pp. 482-497.
[5] S. Nagata, K. Toyota,Y. Imai,T. Setoguchi, M.A.H. Mamun, Numerical Analysis on Primary Conversion Efficiency of Floating OWC-type Wave Energy Converter, Proceedings of the Twenty-first International Offshore and Polar Engineering Conference, 2011, pp. 578-585.
[6] R.Ojima,Y. Goda, S. Suzumura, Analysis of Efficiency of Pneumatic-type Wave Power Extractors Utilizing Caisson Breakwaters, Report of the Port and Harbour Research Institute, Vol.22, No.3,1983, pp. 125-158. (in Japanese)
[7] S. Takahashi, R. Ojima, S. Suzumura, Air Power Pneumatic-type Wave Power Extractors due to Irregular Wave Actions, Report of the Port and Harbour Research Institute, Vol.24, No.1,1989, pp.3-41.
[8] H. Nakagawa and K. Ueki, Study on Absorbed Wave Power by Air Chambers Installed in Breakwater, Journal of the Japan Society of Naval Architects and Ocean Engineers, No. 5, 2007, pp. 155-161.

6th BSME International Conference on Thermal Engineering (ICTE 2014)

Numerical study of the wetting and mobility of liquid droplets on horizontal and inclined flat and microgrooved surfaces

Nazia Farhat, Saif Khan Alen, Md. Ashiqur Rahman*

Department of Mechanical Engineering, Bangladesh University of Engineering and Technology, Dhaka-1000, Bangladesh

Abstract

Designing hydrophobic surfaces with controllable wettability has attracted much interest in the recent times. The present study seeks to simulate the static and dynamic wetting behavior of liquid droplets on horizontal flat and microgrooved surfaces and compare the findings with experimentally obtained data. Using an open-source software, a 3D drop-shape model is developed to numerically analyze the shape of liquid droplets and anisotropic wetting for a wide range of parametric space. The effects of droplet volume, variation in the microgroove geometry and wettability gradient along the parallel and perpendicular directions of the microgrooved surfaces *etc*. on the drop shape and apparent contact angle are examined. Simulation and analysis are extended to analyze the wetting behavior of V-grooved geometry and are compared with the findings on rectangular microgrooved surfaces. For creating wettability gradient along the parallel direction of the grooves, periodic PDMS (Polydimethylsiloxane) coating is considered and increased hydrophobicity of the surface is observed with significant increase in the parallel contact angle for this case. The simulated results manifest considerable differences in the wetting pattern of the microgrooved and flat surfaces and are found out to be in good agreement with the experimental findings.

Keywords: Wettability; Microgrooved surface; Drop shape modelling; Water retention; Anisotropic wetting.

---

* Corresponding author. Tel.: +88-01712-274887.
  E-mail address: ashiqurrahman@me.buet.ac.bd

1. Introduction

Nomenclature

θ	intrinsic contact angle
θ_w	apparent contact angle at Wenzel state
θ_c	apparent contact angle at Cassie state
r	roughness factor
f	Cassie roughness factor
σ_{sf}	surface tension at solid-vapor interface
σ_{sl}	surface tension at solid-liquid interface
σ_{lf}	surface tension at liquid-vapor interface

Modification of the intrinsic wetting property of metal surfaces can play a significant role in a range of modern technological developments. Analysis of droplet motion and liquid retention property of a surface is important for a wide range of applications such as refrigeration, microfluidic operation, electrowetting-based cooling *etc.* A liquid droplet, when placed on a rough surface, can reside in any of the two different wetting states or modes. The first one is the collapsed state, in which the drop enters into the groove or bottom of the surface roughness and completely wets the substrate. In another mode, the drop forms a composite surface under it. In this composite state, the drop does not enter into the groove, which results into a periodic contact of solid-liquid and liquid-air under the drop. The former collapsed state is termed as 'Wenzel state' and the latter one is called 'Cassie state' of wetting.

Inducing superhydrophobicity in an intrinsically hydrophobic surface is a very active field of research. Many researchers suggested different ways of including roughness to increase the hydrophobic wetting behavior of the surface. In an earlier study, Oliver and Mason [1] reported the influence of surface roughness on the equilibrium spreading of liquids on aluminum and stainless steel surfaces. Bico *et al.* [2] obtained a contact angle close to 180° when they placed a small drop of water on a hydrophobic rough surface. Many researchers modified an intrinsically hydrophobic surface by introducing roughness of different geometry, such as square shaped pillars or rectangular microgrooves to the substrate [3,4].There has been considerable interest to modify intrinsically hydrophilic surface into hydrophobic surface by introducing roughness. A design and fabrication procedures of such surfaces are described by Cao *et al.* [5], who induced superhydrophobic behavior on hydrophilic surface by micro-texturing the surface. Patankar and He [6,7] in two separate studies, reported hydrophobic behavior on an intrinsically hydrophilic surface by fabricating cavities on the surface and proposed multiple equilibrium droplet shapes on rough hydrophobic surfaces.

Recently, many experimental studies have been reported for analyzing the hydrophobic behavior of intrinsically hydrophilic surface. Abdelsalam *et al.* [8] studied the hydrophobic wetting behavior of regularly structured gold surface, which is hydrophilic in nature. Sommers and Jacobi [9] developed a model for the critical droplet size on microgrooved aluminum surfaces. Rahman and Jacobi [10-14] reported a series of studies on the anisotropic wetting and frosting/defrosting behavior of brass surfaces whose wetting behavior was modified by fabricating rectangular microgrooves on them via micromachining.

Xu and Wang [15], in their study on multi-phase flow on rough hydrophobic surface, derived the Cassie and Wenzel equation from phase field model. Conditions to be satisfied for the wetting transition (Cassie or Wenzel) on rough surfaces were described by several researchers [16-19]. However, these derived conditions were for intrinsically hydrophobic surfaces.

In this present study, a numerical simulation has been conducted to analyze the anisotropic wetting characteristics of brass surfaces with parallel, rectangular microgrooves by varying the geometric properties of the roughness. After validating the numerical results with experimentally obtained data, the simulation is extended to a different groove geometry. Moreover, the effect of periodic wettability gradient, simulating a PDMS coating, along the parallel direction to the groove is analyzed. For this present work, limiting and transition conditions are derived by comparing the Gibb's free energy between the Wenzel and Cassie states. Mathematical condition is given into the simulation software to automatically detect the wetting state of the drop from the given input geometric parameters.

2. Numerical simulation

For numerical simulation, Surface Evolver, an interactive software to analyze the liquid drop shape, has been used. Several other researchers [20, 21] used this open access software for numerically simulating and analyzing drop shape and wetting state on different structured surfaces. A detailed description of the simulation procedure is given in the surface evolver manual [22]. A brief explanation of simulation methodology along with the simulation procedure is given in the next section.

2.1. Simulation Methodology

For calculating the equilibrium shape of a drop on a substrate, energy minimization needs to be carried out numerically. The total free energy of the system needs to be minimized [20] for obtaining equilibrium drop shape. The free energy G of the system is expressed as the following equation:

$$G/\sigma_{lf} = A_{lf} - \iint Cos\theta dA \qquad (1)$$

where θ is the intrinsic contact angle and σ_{lf} are the surface tension at the liquid-air interface. And the integration of the right hand side of this equation is along A_{sl} which is the area of solid-liquid interface. The intrinsic contact angle can be defined by young's equation:

$$Cos\theta = \frac{\sigma(sf) - \sigma(sl)}{\sigma(lf)} \qquad (2)$$

where θ is the young's contact angle, and σ_{sf}, σ_{sl} and σ_{lf} are the interface surface tension at the solid-air, solid-liquid and liquid-air, respectively. In this expression of free energy, the effect of gravity is neglected because in this present work this expression has been used for a small (<12 μl) droplets (sessile droplet). For a constant drop volume, the free energy needs to be minimized to obtain the equilibrium drop shape. As the free energy G is minimized with respect to the liquid-fluid interface shape, it can be observed from equation (1) that the only parameter which contributes to the equilibrium drop shape on a surface is the actual contact angle. Before obtaining the equilibrium shape using free energy minimization, the wetting state of the drop on substrate needs to be defined. Brass is intrinsically hydrophilic ($\theta<90°$) and in this simulation the wetting state is predicted using the geometry of the microgroove.

2.2. Simulation details in Surface Evolver

An open source software 'Surface Evolver' is used to obtain the equilibrium drop shapes. At first the surface is generated by defining its vertices, edges and faces and then geometric, energy and volumetric constraints have been applied to the necessary vertices and edges of the surface. When the droplet is in Wenzel state, the liquid-vapor interface is assumed to have disappeared and the droplet gets the energy corresponding to the intrinsic contact angle of the rough surface locally. When Cassie state is observed, it has been assumed that the liquid-vapor interface at the air-gap gets the liquid-vapor interfacial energy and the contact angle corresponding to this is 180°.
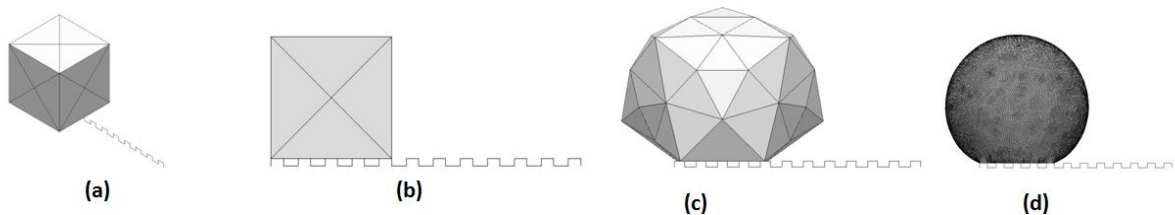

(a) (b) (c) (d)

Figure-1: Drop attaining equilibrium shape in simulation (a) Initial Cube on which the constraints are defined (b) Orthogonal view of the initial drop (c) Drop minimizing the surface energy after very small number of iteration (d) Equilibrium drop shape at the end of the simulation.

The drop volume considered in this work is varying between 4 µl to 12 µl, so the effect of gravity can be neglected as the drop radius R is less than the capillary length α and so the liquid-vapor interface at the groove can be taken as a straight line instead of a curvature. Here α is defined as

$$\alpha = \sqrt{\frac{\sigma(lf)}{\Delta\rho \, g}} \qquad (3)$$

where σ_{lf} is the surface tension in solid-air interface and $\Delta\rho$ is the difference between liquid density and the density of the surrounding air.

Among the four edges of the bottom face, left and right edges are constrained to move on two outer most pillars respectively. This boundary condition is necessary because physically the number of pillar on which the drop resides is defined by the drop formation process. While applying the constraints to the facets and edges in the simulation, only the bottom face is considered to be responsible for obtaining the shape of the droplets. For convenience, the boundary conditions are given to the edges, which contribute to generate the three phase contact line. Figure 1 illustrates the steps involved in the simulation in Surface Evolver. As we can see from Figure 1(c), after a small number of iterations, droplet tries to obtain a minimum energy (spherical) shape. After sufficient iterations and several refinement steps, the droplet finally attains the required spherical shape as shown in Figure 1(d).

3. Result analysis and discussion

3.1. Sample geometry and contact angle data

For the present work, eight microgrooved brass samples with four having a constant groove depth and width and four more samples with a constant groove width and pillar width are selected for drop shape analysis and simulation. To verify the validity of the numerical simulation, the experimentally and numerically obtained orthogonal and parallel contact angles and shape of the droplets under the same conditions are compared.

In order to ensure that the comparisons are made for the same conditions, all parameters (droplet size, number of pillars the experimental and simulated drops are resting on, dimension of the groove geometry parameters such as width, depth and spacing *etc.*) are kept constant. Topographic data of all the rectangular microgrooved brass samples used in the present study and experimentally and numerically observed wetting state on different surfaces (rectangular and V-grooved surfaces, surfaces with imposed wettability gradient) are shown in Table 1. All the microgrooved samples had a fixed groove width of 130 µm. The number of pillars the liquid drops are resting on for different surfaces, along with the contact angle data obtained experimentally and from simulation, are for a fixed drop volume of 5 µl.

Table-1: Topographic data 8 microgrooved brass samples used in this present study. The microgrooved samples are designated as $D_G{}^x W_P{}^y W_G{}^z$; where D_G, W_P, W_G stand for the groove depth, pillar width, and groove width, respectively, and the superscripts x, y and z represent the numerical values of these parameters.

Sample	Dimensions (um)			Wetting State			
	Depth of Groove (Dg)	Width of Pillar (Wp)	Width of Groove (Wg)	Experimental	Rectangular Groove	V Groove	Rectangular Groove With Wettability Gradient
$D_G{}^{67}W_P{}^{26}W_G{}^{130}$		26		Wenzel	Wenzel	Wenzel	Wenzel
$D_G{}^{67}W_P{}^{80}W_G{}^{130}$	67	80	130	Cassie	Cassie	Wenzel	Cassie
$D_G{}^{67}W_P{}^{110}W_G{}^{130}$		110		Cassie	Cassie	Wenzel	Cassie
$D_G{}^{67}W_P{}^{187}W_G{}^{130}$		187		Cassie	Cassie	Wenzel	Cassie
$D_G{}^{27}W_P{}^{112}W_G{}^{130}$	27			Wenzel	Wenzel	Wenzel	Wenzel
$D_G{}^{67}W_P{}^{112}W_G{}^{130}$	67	112	130	Cassie	Cassie	Wenzel	Cassie
$D_G{}^{98}W_P{}^{112}W_G{}^{130}$	98			Cassie	Cassie	Wenzel	Cassie
$D_G{}^{122}W_P{}^{112}W_G{}^{130}$	122			Wenzel	Wenzel	Cassie	Wenzel

Table-2: Comparison of numerically obtained apparent contact angle data with experimental results of 8 microgrooved brass samples (constant drop volume of 5µl and number of pillar is selected from the experimental observation)

Sample	Volume of Water Droplet (ul)	No. of Pillars Under the Droplet	Experimentally Measured Contact Angle (°)		Numerically Obtained Contact Angle (°) Rectangular Groove	
			Orthogonal	Parallel	Orthogonal	Parallel
$D_G^{67}W_P^{26}W_G^{130}$	5	10	141.6	53.1	131.6	60.8
$D_G^{67}W_P^{80}W_G^{130}$	5	6	144.9	124.0	153.4	123.7
$D_G^{67}W_P^{110}W_G^{130}$	5	5	145.7	85.2	150.6	90.0
$D_G^{67}W_P^{187}W_G^{130}$	5	4	142.9	115.5	148.2	90.0
$D_G^{27}W_P^{112}W_G^{130}$	5	6	134.7	63.4	134.1	61.1
$D_G^{67}W_P^{112}W_G^{130}$	5	5	145.7	85.2	150.6	90.0
$D_G^{98}W_P^{112}W_G^{130}$	5	5	142.8	100.3	150.4	92.0
$D_G^{122}W_P^{112}W_G^{130}$	5	5	132.7	27.3	138.6	51.3

3.2. Comparison and analysis of the experimental and numerical results

One of the primary objectives of this work was to examine the effect of roughness geometry on the wettability of a surface. The key parameters when analyzing the wetting behavior of a surface are the wetting state and apparent contact angle. The apparent contact angle in the orthogonal direction of the grooves is also considerably dependent on the number of pillar rather than the dimension of the roughness. So when wetting state is defined, parallel contact angle is the only parameter that plays an important role to compare wetting behavior of two surfaces. So to investigate the wetting behavior of different roughness geometry, at first the numerical results and experimental findings of rectangular microgroove surface were compared in Figures 2(a-d). The experimental values had an uncertainty of ± 4°, and the numerical results agreed with the experimental one with a maximum difference of ± 10°.

It should be noted here that the simulation conditions for obtaining the numerical results of Figure 2 were very realistic as they were for the same geometry, same drop size and rested on the same number of pillars as that of the experiments. An excellent agreement between the numerical and experimental findings can be observed from Figure 2 for a fixed drop volume of 5 µl. It means that the simulations were successful in capturing the wetting physics properly. Also the wetting state was successfully captured with the given input conditions which were derived mathematically by using energy balance between Cassie and Wenzel states. Next, the validity of this simulation procedure was examined further for random size of the droplets and similar set of simulations were performed by varying the droplet volume from 4 µl to 12 µl and choosing experimentally validated supporting pillar numbers for a particular liquid drop. The results are plotted in Figures 3(a-d), from where it can be clearly seen that the findings exhibit very similar trend and the experimental and numerical values vary within a range of 15°. But in some cases the differences were significant in the parallel direction and especially for the droplets in a Wenzel wetting state. It is because the software is not able to include the physics of capillary channeling, which causes the droplet to expand significantly along the grooves in Wenzel wetting, especially observed for machined grooves [1,10].

Now that a good agreement between the numerical results and experimental findings is obtained, our study is extended to examine the wetting behavior of this rough brass surfaces with different roughness geometry. For this, the simulation was conducted for V-grooved brass surfaces with similar dimensions (groove depth and groove width at the top) of rectangular grooves. And it can be seen clearly from Figure 4(b) that for all 8 microgrooved brass surfaces, V-grooved geometry demonstrates a parallel contact angle of 55°-60°, which were much less than that of surfaces with rectangular grooves under the same conditions. The reason behind this is that a V-grooved surface has a lower droplet suspending ability than that of a rectangular grooved surface. As a result, the wetting state was Wenzel, resulting in a significant decrease in the parallel contact angle. Therefore, replacing the rectangular grooves with V-grooves is unlikely to increase the hydrophobicity, though machining a V-grooved surface is easier than machining a rectangular grooved surface.
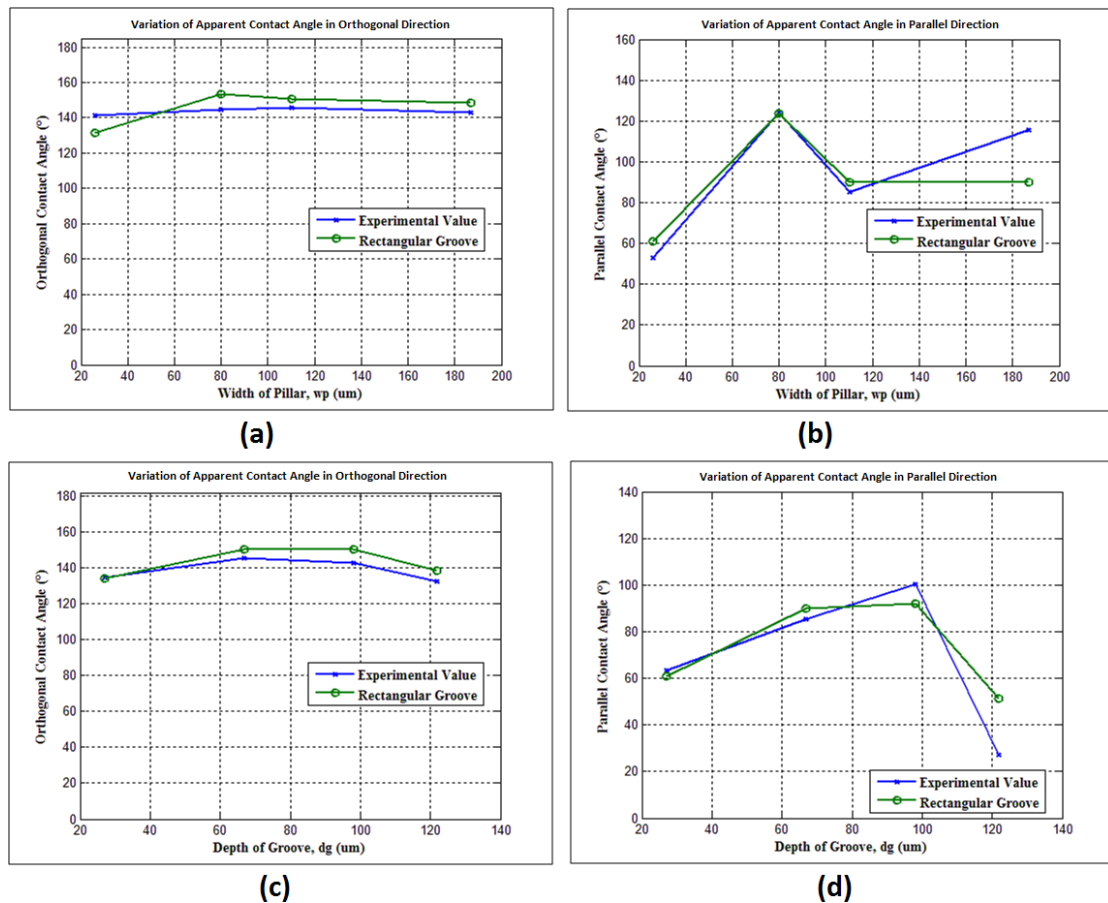
Figure-2: Comparison between experimental and numerically obtained results for surfaces with a variation of pillar width (top row) and groove depth (bottom row), keeping all other parameters constant (for drop volume= 5 μl) These variation are shown for apparent contact angles along the (a) orthogonal direction with varying W_P (D_G =67 μm, W_G=130 μm) (b) parallel direction with varying W_P (D_G =67 μm, W_G=130 μm) (c) orthogonal direction with varying D_G (W_P=112 μm, W_G=130 μm), and (d) parallel direction with varying D_G (W_P=112 μm, W_G=130 μm).

Since the consideration of V-grooved geometry did not provide a possible solution for obtaining a more hydrophobic behavior of the surface, the simulation was further extended for rectangular microgrooved surface which has periodic wettability gradient on the pillars. The concept of providing a periodic wettability gradient along the parallel direction to the groove simulated the physical condition of coating the surface periodically with strips of PDMS (Polydimethylsiloxane) 200 μm wide with a gap of 200 μm across the pillars. When this wettability gradient was applied, a significant rise in parallel contact angle can be observed from Figure 4 (b,d). A new composite surface of brass and PDMS under the drop on the pillar may be responsible for this significant rise. For sample $D_G^{67}W_P^{112}W_G^{130}$, this increase in parallel contact angle was 22°. And for every sample, applying wettability gradient increased the contact angle in the parallel direction of the grooves by almost 20°, which might promote a better water drainage behavior of the surface.

3.3. Drop shape comparison

Comparison between the numerical result and experimental drop shape enables to obtain a proper validation of the simulation methodology. In the present study, a close agreement between the experimental and the simulated drop shapes on rectangular microgroove surfaces was observed. It was observed from the simulation that the pillar number has a significant effect on the orthogonal contact angle. Therefore, the number of pillars along with the other

groove dimensions was kept constant to systematically analyze the variation in the wetting behavior among rectangular groove, V-groove, and periodically wettability gradient surfaces.

The top views of liquid droplet from both experimental and numerical results are compared in Figure 5. From Figures 5(a,b),we can see that for sample $D_G^{122}W_P^{112}W_G^{130}$ that the shape of the water droplets obtained experimentally and from our simulation exhibited excellent agreement. The drop shape was elliptical due to the fact that the wetting state for this sample was Wenzel. So the parallel contact angle was much less than the orthogonal contact angle, resulting in an elliptical drop shape. From this top view comparison, the small deviation from the experimental shape may be seen which was probably due to the fact that the experimental drop shape was for a drop size of 25 µl while the simulation result is for a 10 µl drop. From Figures 5(c, d) it can be seen that the three-phase contact angle for the sample of $D_G^{67}W_P^{110}W_G^{130}$ (5µl) was not a regular ellipse. Some portion of this three-phase contact line was irregular along the orthogonal direction to the groove. The main reason behind this was that sample $D_G^{67}W_P^{110}W_G^{130}$ formed a Cassie (composite) state over the substrate. As a result a composite state of solid-liquid and solid-air contact line was formed. Similar findings were reported by Patankar *et al.* [20].
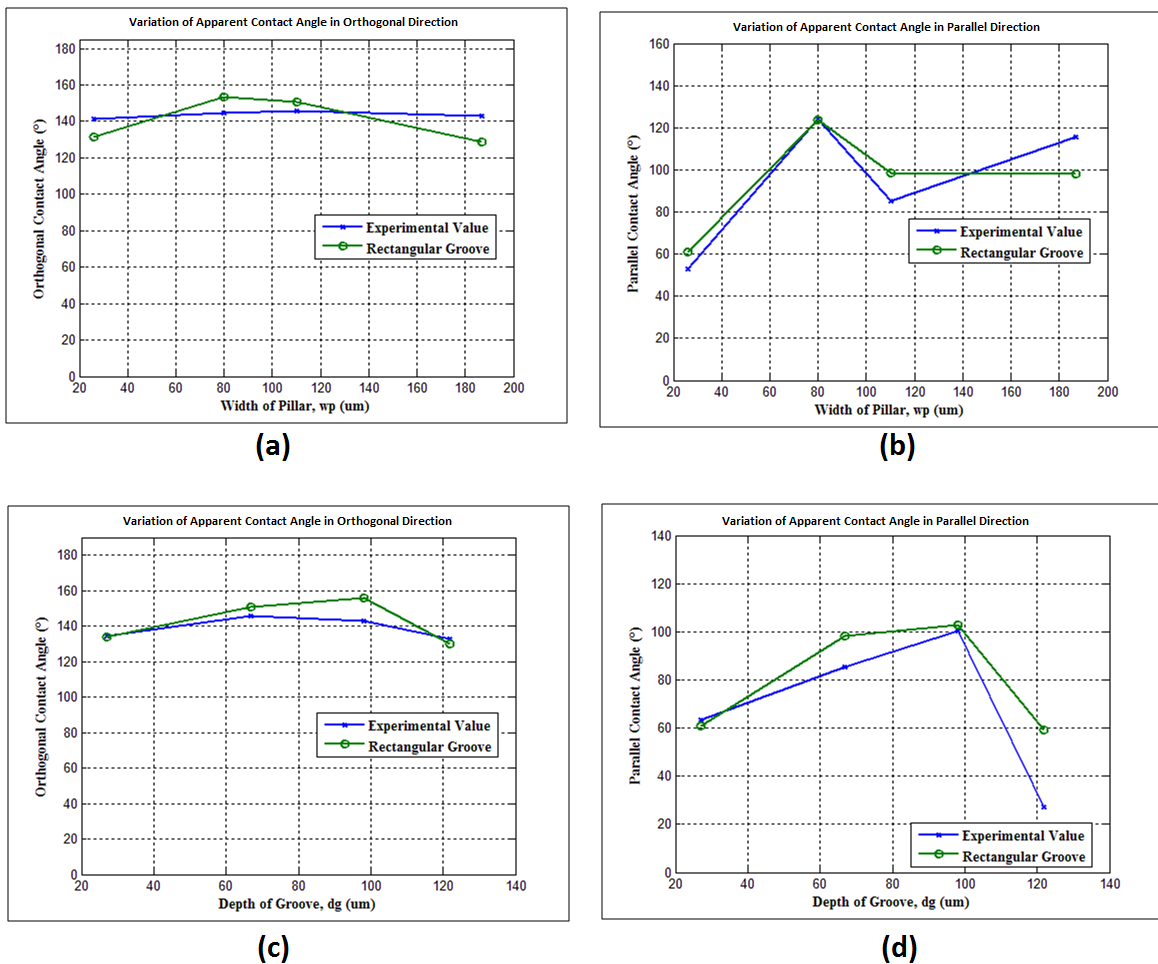

(a)

(b)

(c)

(d)

Figure-3: Comparison between experimental and numerically obtained results for surfaces with a variation of pillar width (top row) and groove depth (bottom row),, for different combinations of drop volume (4 µl -12 µl) and experimentally validated number of pillars supporting the droplets. These variations are shown for apparent contact angles along the (a) orthogonal direction with varying W_P (D_G =67 µm, W_G=130 µm) (b) parallel direction with varying W_P (D_G=67 µm, W_G=130 µm) (c) orthogonal direction with varying D_G (W_P=112 µm, W_G=130 µm), and (d) parallel direction with varying D_G (W_P=112 µm, W_G=130 µm).
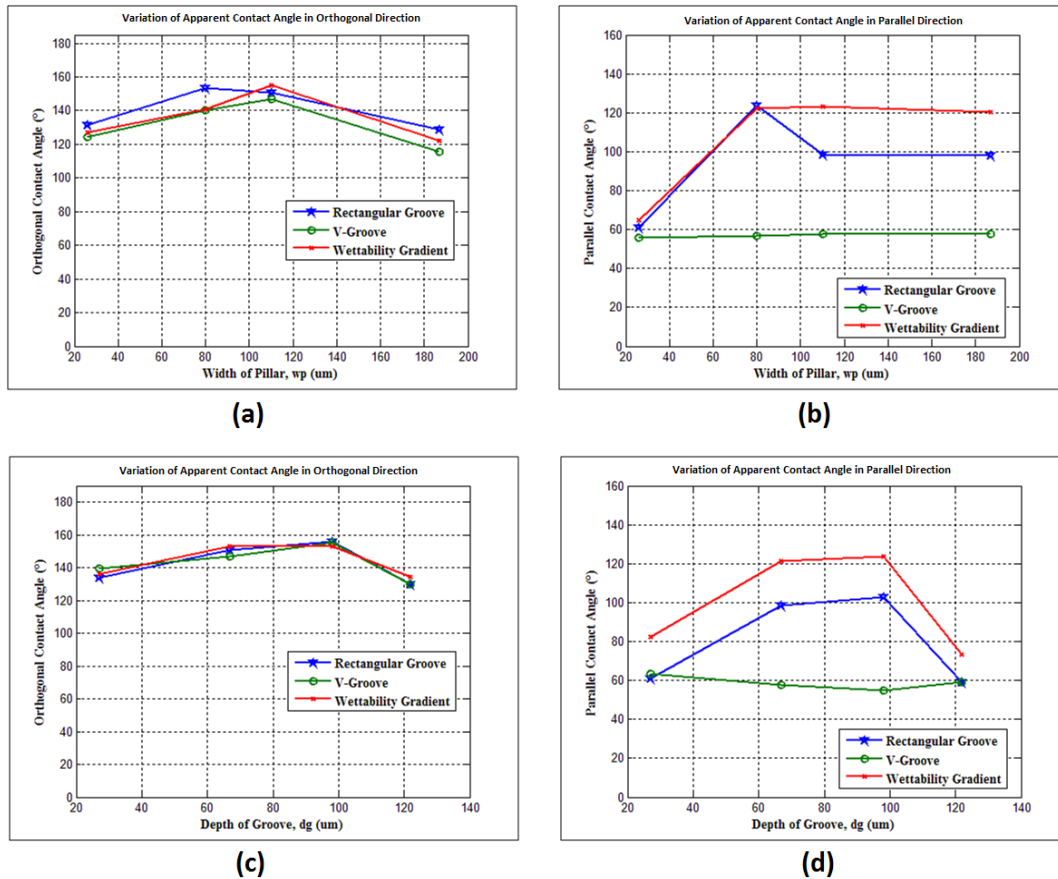
Figure-4: Comparison among numerically obtained contact angles for surfaces with rectangular grooves, V-grooves and rectangular grooves with an imposed wettability gradient. Plot is obtained by changing the width of pillar and depth of groove successively, for different combination of drop volume (4 -12 µl) and experimentally validated number of pillars. The results are shown for apparent contact angles along the (a) orthogonal direction with varying W_P (D_G =67 µm, W_G=130 µm) (b) parallel direction with varying W_P (D_G =67 µm, W_G=130 µm) (c) orthogonal direction with varying D_G (W_P=112 µm, W_G=130 µm), and (d) parallel direction with varying D_G (W_P=112 µm, W_G=130 µm).

To compare the drop shape along the orthogonal and parallel direction to the groove, samples $D_G^{67}W_P^{26}W_G^{130}$ and $D_G^{67}W_P^{187}W_G^{130}$ were selected, which exhibited a Wenzel and Cassie wetting state, respectively. From Figures 6-7, it can be seen clearly that the simulation software could accurately sense the wetting state of the drop and at the same time accurately captured the wetting dynamics. The shape of the droplet from both the orthogonal and parallel directions of the grooves obtained experimentally and numerically matched very closely as we can see from Figures 6(a,b) and Figures 6(e,f), respectively. From Figures 6(f,g), it can be seen that in case of a V-grooved surface, the parallel contact angle remained nearly same as the wetting state in this case was Wenzel for both the rectangular and V-grooved surfaces. In addition, Figures 6(f,h) clearly indicates that an imposed wettability gradient (a 200 µm strip simulating PDMS coating which has a contact angle of 114⁰ and applied periodically with a spacing of 200 µm) increased the contact angle, especially in the parallel direction of the groove. There was a maximum of 20° increase in parallel contact angle for this wettability gradient condition. The modified wettability obtained by incorporating a wettability gradient may be used further for obtaining better water drainage behavior from microgrooved surfaces.

From Figure 7, a similar analysis may be performed while comparing the drop shapes for different groove geometry which exhibited a Cassie wetting state experimentally. Here, from Figure 7(g), it can be seen that the contact angle decreased considerably on the V-grooved surface. It was because of the difference in wetting states (Cassie and Wenzel) between rectangular and V-grooved surfaces having the same groove dimensions. From the excellent agreement between the experimental and rectangular microgrooved drop shapes, it is obvious that the developed software for this numerical simulation is capturing the wetting physics accurately.
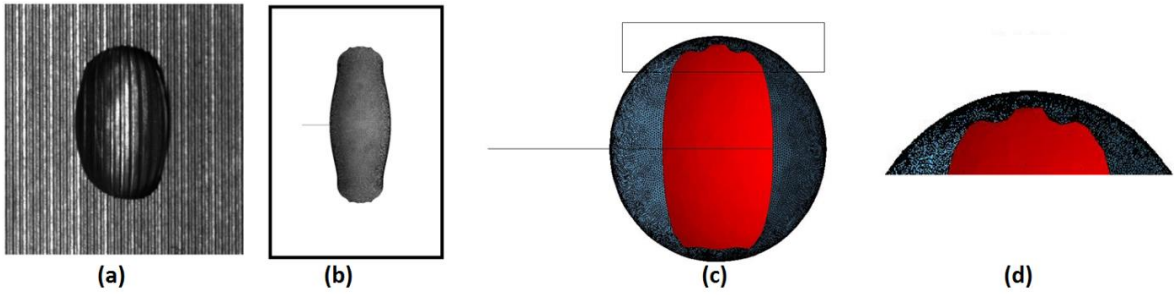
Figure-5: Top view of a water droplet on rectangular microgrooved sample $D_G^{122}W_P^{112}W_G^{130}$ (a) Experimental result (b) From Simulation. And bottom view of the drop sample $D_G^{67}W_P^{110}W_G^{130}$ from numerical simulation on rectangular microgrooved surface to analysis of three phase contact line (c) Original view (d) Magnified view of the selected portion.
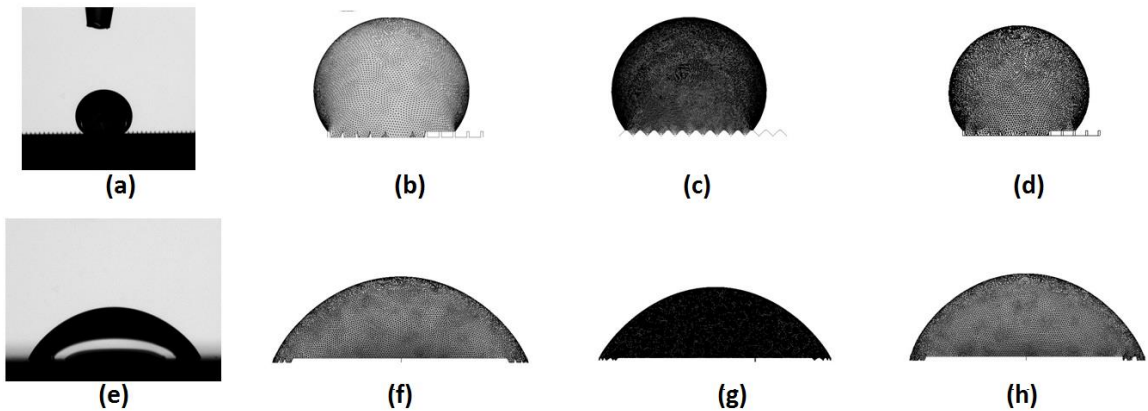

Figure-6: Drop Shape for sample $D_G^{67}W_P^{26}W_G^{130}$(5 µl drop volume residing on 10 pillars) viewed from both orthogonal and parallel direction of the grooves. In the top row, drop shape from the orthogonal direction obtained from (a) Experiments (b) Simulation (rectangular groove) (c) Simulation (V-groove) and (d) Simulation (rectangular groove with wettability gradient). In the bottom row (e-h), drop shape from the parallel direction of the grooves on these surfaces in the same order.

Figure-7: Drop Shape for sample $D_G^{67}W_P^{187}W_G^{130}$ (5 µl drop volume residing on 4 pillars) viewed from both orthogonal and parallel direction of the grooves. In the top row, drop shape from the orthogonal direction obtained from (a) Experiments (b) Simulation (rectangular groove) (c) Simulation (V-groove) and (d) Simulation (rectangular groove with wettability gradient). In the bottom row (e-h), drop shape from the parallel direction of the grooves on these surfaces in the same order.
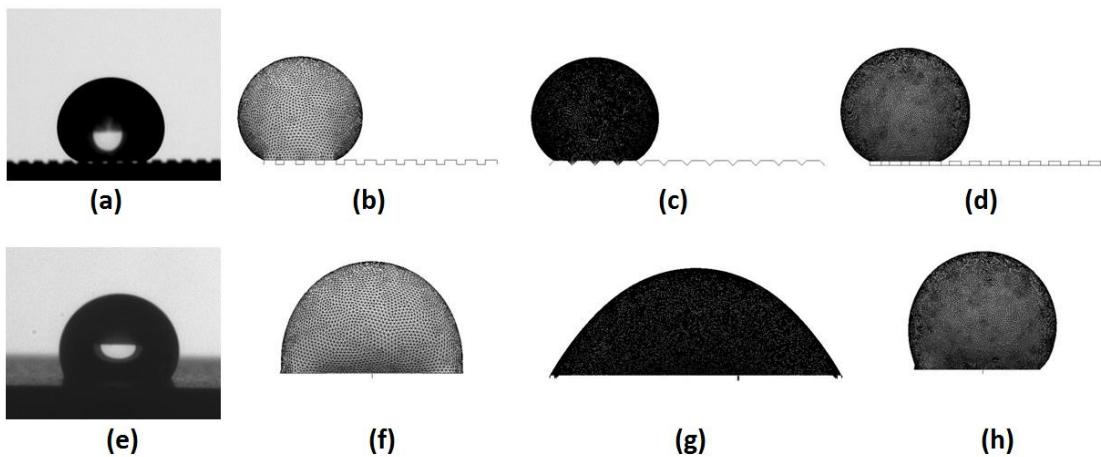
4. Conclusion

A detailed numerical simulation was been performed to analyze the wetting behavior of microgrooved brass surfaces having a variation of groove depth and spacing. The main objective of this work was to capture the wetting state and wetting dynamics accurately on these surfaces, along with the same on other designed micro structured surfaces. Drop shape analysis was performed and compared for the experimental and numerical results for a total of 8 microgrooved surfaces. Experimental findings and numerical results showed a very good agreement, with a maximum variation of less than ±10°. The simulation was then extended further for V-grooved surfaces with similar groove dimension as that of rectangular microgrooves. However, no significant improvement in the wetting behavior of the brass surfaces were observed, rather the contact angles in the parallel direction of the grooves were found to decrease on V-grooved surfaces due to the wetting state being Wenzel for the same groove depth and width. On the contrary, applying a periodic wettability gradient simulating 200 μm PDMS strips on the pillars along the parallel direction to the groove significantly altered the wetting behavior of the surface. The increase in contact angle in the parallel direction of the microgrooves due to the imposed wettability gradient was as high as 20°. The authors are working now to develop a mathematical model that can predict the wetting state of the liquid droplet from the roughness geometry of a rough hydrophobic surface having an intrinsically hydrophilic behavior.

Reference

[1]　J. F. Olivier, S. G. Mason, Liquid spreading on rough metal surfaces, Journal of Material Science 15 (1980), pp. 431-437.

[2]　 J. Bico, C. Marzolin, D. Quere, Pearl drops, Europhysics Letters 47 (2) (1999), pp. 220-226.

[3]　N. A. Patankar, On the Modeling of Hydrophobic Contact Angles on Rough Surfaces, Langmuir 2003, 19, pp. 1249-1253.

[4]　L. Barbieri, Wetting properties of flat-top periodically structured superhydrophobic surfaces, The University of Genoa, Italy.

[5]　L. Cao, H. H. Hu, D. Gao, Design and Fabrication of Micro-textures for Inducing a Superhydrophobic Behavior on Hydrophilic Materials, Langmuir, 2007.

[6]　B. He, N. A. Patankar, J. Lee, Multiple Equilibrium Droplet Shapes and Design Criterion for Rough Hydrophobic Surfaces, Langmuir, 2003.

[7]　N. A. Patankar, Hydrophobicity of Surfaces with Cavities: Making Hydrophobic Substrates from Hydrophilic Materials?, Journal of Adhesion Science and Technology, April, 2012.

[8]　M. E. Abdelsalam, P. N. Bartlett, T. Kelf, Jeremy Baumberg, Wetting of Regularly Structured Gold Surfaces, Langmuir, 2005, 21, pp. 1753-1757.

[9]　A. D. Sommers, A. M. jacobi, Wetting phenomenon on micro-grooved aluminum surfaces and modeling of the critical droplet size, Journal of Colloid and Interface Science, 2008.

[10] M. A. Rahman, A. M. Jacobi, Wetting Behavior and Drainage of Water Droplets on Microgrooved Brass Surfaces, Langmuir, 2012.

[11] M. A. Rahman, A. M. Jacobi, Study of frost properties and frost melt water drainage on microgrooved brass surfaces in multiple frost/defrost/refrost cycles, Applied Thermal Engineering, 2014.

[12] M. A. Rahman, A. M. Jacobi, Effect of microgroove geometry on the early stages of frost formation and frost properties, Applied Thermal Engineering 56 (2013), pp. 91-100.

[13] M. A. Rahman, A. M. Jacobi, Experimental study on condensation, frost formation and condensate retention on microgrooved and plain brass surfaces under natural convection condition, 8th International Conference on Heat Transfer, Fluid Mechanics and Thermodynamics, 26th June - 1st July 2011, Pointe Aux Piments, Mauritius.

[14] M. A. Rahman, A. M. Jacobi, Drainage of frost melt water from vertical brass surfaces with parallel microgrooves, International Journal of Heat and Mass Transfer 55 (2012), pp. 1596-1605.

[15] X. Xu, X. Wang, Derivation of the Wenzel and Cassie equations from phase field model for two phase flow on rough surface, SIAM J. Appl. Math., Vol. 70, No. 8, pp. 2929-2941.

[16] E. Bormashenko, Progress in understanding wetting transitions on rough surfaces, Advances in Colloid and Interface Science- 2014.

[17] C. X. Ling, L. Tian, The apparent state of droplets on a rough surface, Science in China Series G: Physics, Mechanics & Astronomy- 2009.

[18] E. Bormashenko, Wetting transitions on biomimetic surfaces, Phil. Trans. R. Soc. A- 2010.

[19] X. Cui, W. Li, On the possibility of superhydrophobic behavior for hydrophilic materials, Journal of Colloid and Interface Science- 2010.

[20] Y. Chen, B. He, J. Lee, N. A. Patankar, Anisotropy in the wetting of rough surfaces, Journal of Colloid and Interface Science 281 (2005),pp. 458–464.

[21] N.Janardan, M. V. Panchagnula, Effect of the initial conditions on the onset of motion in sessile drops on tilted plates, Colloids and Surfaces A: Physicochemical and Engineering Aspects, 2014.

[22] K.A. Brakke, http://www.susqu.edu/facstaff/b/brakke/evolver.